ABSTRACT

Seismo-Lineament Analysis of The Malibu Beach Quadrangle, Southern California

Lauren E. Seidman, M. S.

Chairperson: Vincent S. Cronin, Ph.D.

The Santa Monica Mountains are a young, structurally active mountain range within southern California. The purpose of this study was to map seismogenic faults within the Malibu Beach quadrangle. Using available earthquake data, I projected fault-plane solutions onto a digital elevation model (DEM). The intersection of each fault-plane solution with the DEM yielded a seismo-lineament whose width reflected the reported confidence interval associated with the earthquake location. Geomorphic lineaments were identified and mapped by illuminating the DEM at a 45 degree elevation from various azimuths. The lineament maps were used to generate hypotheses about the possible location of structures, which were field evaluated. Field work verified the existence of previously unmapped faults along some lineaments. Some faults are approximately coplanar with earthquake fault-plane solutions, and are tentatively considered seismogenic. Focal mechanism solutions and field observations suggest that strain is partitioned between several active faults, including some with pure strike-slip displacements.

Seismo-Lineament Analysis of The Malibu Beach Quadrangle, Southern California

by

Lauren E. Seidman, B.A.

A Thesis

Approved by the Department of Geology

_____
Steven G. Driese, Ph.D., Chairperson

Submitted to the Graduate Faculty of
Baylor University in Partial Fulfillment of the
Requirements for the Degree
of
Master of Science

Approved by the Thesis Committee:

_____
Vincent S. Cronin, Ph.D., Chairperson

_____
John A. Dunbar, Ph.D.

_____
Gregory A. Benesh, Ph.D.

Accepted by the Graduate School
May 2007

_____
J. Larry Lyon, Ph.D., Dean

Page bearing signatures is kept on file in the Graduate School.

TABLE OF CONTENTS

LIST OF FIGURES

LIST OF TABLES

ACKNOWLEDGMENTS

With great pleasure I wish to thank the following individuals for their exceptional contributions to the completion of my project. First and foremost, I extend heartfelt gratitude and appreciation to my thesis advisor, Dr. Vincent S. Cronin, for taking me on as a graduate student, and for his creativity and innovation without which this research project would not have taken place. His knowledge and passion in the field of geology, unwavering guidance, and wonderful sense of humor were invaluable to me throughout the duration of this thesis. I am also thankful to my committee members, Dr. John Dunbar and Dr. Greg Benesh, for their challenging academic support and to Baylor University, the Geological Society of America, the Roy J. Shlemon Scholarship, Sigma Xi (The Scientific Research Society), and the SIPES Foundation for their generous monetary support. Furthermore, I felt a special sense of accomplishment due to the steadfast support of my two field assistants, Eric Robinson and Mary Seidman. And finally, to my family, parents Richard and Mary, my sister Lily, and a special aunt, Jeanne Lukaska, who because of their generosity, moral support, and love, I owe everything.

To my grandparents, Ken and Dorothy, who gave me the keys to the kingdom.

“Far and away the best prize that life offers is the

chance to work hard at work worth doing.”

Teddy Roosevelt

CHAPTER ONE

Introduction

The Malibu Beach 7.5 minute quadrangle, where the field work for this thesis was conducted, is located within the west-central Santa Monica Mountains ~65 kilometers southwest of the San Andreas fault and ~40 km west of downtown Los Angeles. The Santa Monica Mountains are a young, structurally active mountain range that is ~15 km wide from north to south and extends ~75 km east-west along the southern boundary of the Transverse Ranges Province (fig. 1).

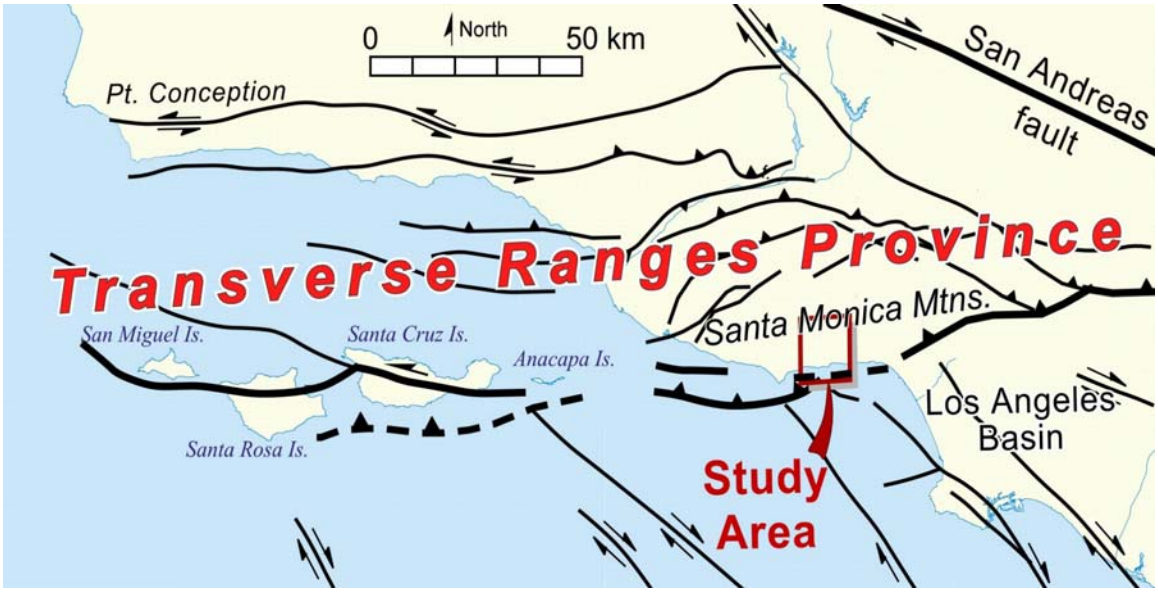

Figure 1. Location of the Malibu Beach 7.5 minute quadrangle (study area) within the structural context of southwestern California. Map extends from approximately 33.5° to 34.75° north latitude and from ~116° to 120.75° west longitude. Adapted from Cronin and Sverdrup (1998).

The Transverse Ranges are physiographically distinctive for being one of just three major mountain ranges in North America that trend east-west, along with the Brooks Range and the Uinta Mountains.

Structural activity in the Santa Monica Mountains is evident from locally high relief developed on sedimentary strata that is typically mid- to late Cenozoic in age. In some places, strata now exposed on ridges hundreds of meters above sea level were accumulating on the sea floor just ~12 million years ago. Current published models for the Santa Monica Mountains place all active faulting along a few left-oblique structures along the coastline, or just offshore (fig. 2; Treiman, 1994).

Figure 2. DEM image of the Point Dume, Malibu Beach, and Topanga 7.5 minute quadrangles. Black lines represent published fault traces of the Malibu Coast fault, from the Potrero fault (P) westward to the Zuma Beach area. Segments outlined in red are legally active and include the Solstice (S) and Winter Mesa (WM) strands (Hart and Bryant, 1999; Treiman, 1994).

The earthquake location data and focal mechanism solutions utilized in this project do not support this limited view of active faulting for the region (fig. 3).

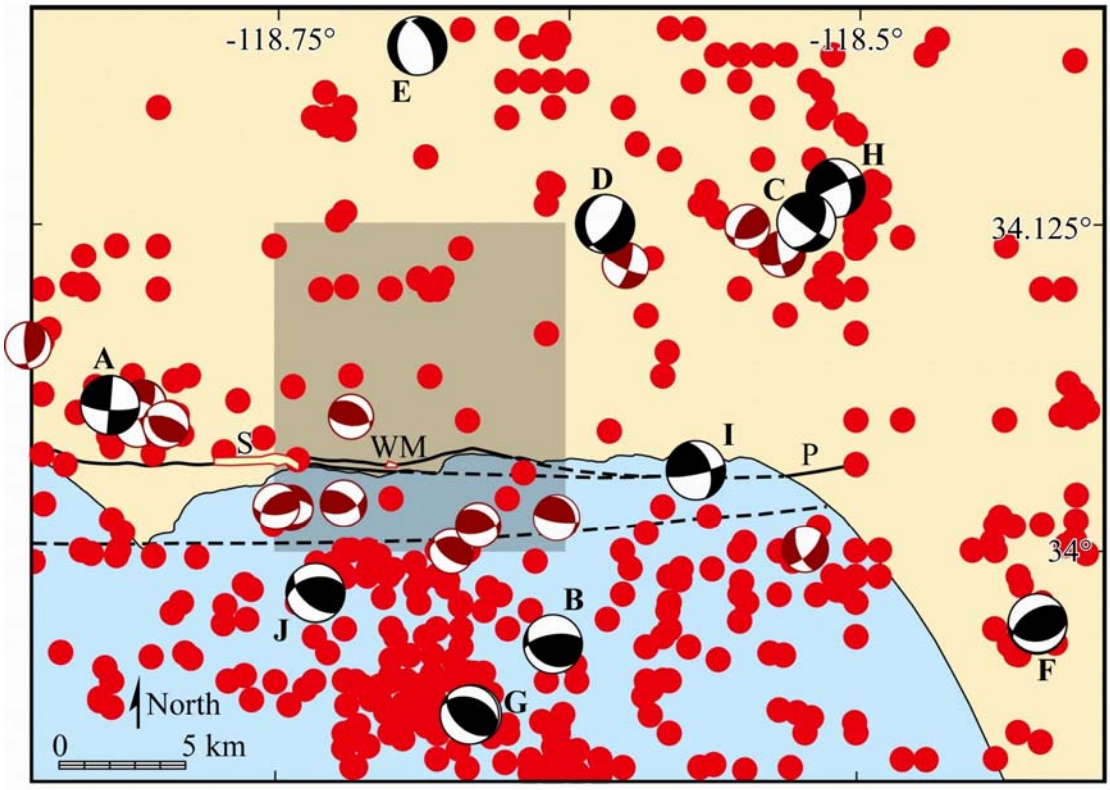

Figure 3. Earthquake data do not support the limited view of structural activity confined to the Malibu Coast fault (black dashed or solid lines; P is Potrero fault) along a narrow near-coastal strip, or to the two Alquist-Priolo fault study zones (yellow outlined in red): the Solstice strand (S) or the Winter Mesa (WM) strand. Red dots are epicenters, black focal-mechanism diagrams correspond to earthquakes used in this thesis, and focal-mechanism diagrams for other earthquakes are in red.

As the term is used in this thesis, a *fault* is a surface or zone on which there is shear displacement of rock or soil (Cronin and Sverdrup, 1998). Most, if not all, earthquakes with foci located within the brittle upper crust are thought to be generated when elastic strain energy stored in rock is suddenly released by frictional slip along a fault surface (Reid, 1910; Scholz, 2000). A fault is considered to be "seismogenic" if it is capable of producing earthquakes.

Recognition of faults that are potentially seismogenic in the Santa Monica Mountains is necessary to fully assess seismic risk in the area. Geologic mapping of the

Santa Monica Mountains since the early 1990's has demonstrated the existence of several faults in the area, most of which are considered inactive (Blake, 1991; Dibblee, 1993; Fisher and others, 2005; Wright, 1991; Yerkes and Campbell, 1980). In addition to faults shown on published geologic maps, other faults are commonly noted in private consulting reports, or are apparent in road cuts and natural outcrops. Some of these faults may be capable of producing earthquakes. Identifying faults that may be seismogenic is of considerable importance in assessing seismic hazards in the greater Los Angeles metropolitan area (Tsutsumi and others, 2001).

Geoscientists commonly integrate analysis of topographic maps and aerial images, along with field work, to successfully identify faults in challenging terrain. Dense chaparral, steep topography, and private property constraints combine to make field mapping difficult in the Santa Monica Mountains. Remote sensing of the topography of a region successfully yields fault locations, as geomorphic features including scarps, sag ponds, terraces, and valleys are indicative of faulting (*e.g.,* Lobeck, 1939; Worchester, 1948). The surface trace of a fault is commonly recognizable on aerial photographs (*e.g.,* Hobbs, 1904; Ray, 1960; Miller, 1961) and satellite imagery (Cronin and others, 1993).

In addition to remote sensing techniques, Geographic Information Systems (GIS) allow geoscientists to integrate geologic, topographic, and photographic information into a single digital format. Within a GIS format, one way geoscientists are able to analyze the geology and topography of a region without vegetative and cultural distractions is by using a digital elevation model (DEM). Analysis of a DEM at different illumination

directions assists in the identification of geomorphic lineaments, which may correspond to actual faults (Haugerud and others, 2003; Cronin and others, 2003).

These remote sensing and GIS techniques combine to generate fault-location hypotheses, which must then be tested in the field. When faults are identified in the field, it is important to determine whether they constitute a hazard and are capable of producing earthquakes.

The identification of seismogenic faults commonly involves a traditional toolkit of paleoseismology techniques: geologic mapping, interpretation of aerial photographs, and trenching (*e.g.*, McCalpin, 1996). These paleoseismic techniques may be implemented along a presumed surface trace of a fault in order to determine whether Holocene age rock material was displaced by movement in a faulting event. Even though trenching is advantageous as it tests the age of the rock displaced by physical movement of the fault, it is nevertheless an arduous, expensive, and dangerous process. It is common in highland areas such as the Santa Monica Mountains for there to be no datable Holocene material at the ground surface, other than latest Holocene slope wash (colluvium). Holocene displacement along a fault whose surface trace is located in a highland area may leave no datable record. In this case trenching will not be able to determine the offset of Holocene rock material. Therefore, another technique has been needed to evaluate faults that cut pre-Holocene age rock at the ground surface.

To account for potentially seismogenic faults that cut pre-Holocene age rock at or near the ground surface, Cronin (2004b, c) developed a method which describes projecting nodal planes from a focal mechanism solution onto a DEM surface to define a seismo-lineament. This thesis project is part of a larger research project led by Cronin,

which involves using seismo-lineament analysis in conjunction with established techniques that geologists currently use to locate potentially seismogenic faults the Santa Monica Mountains. The goal is to investigate this structurally active region by developing a toolkit of techniques that utilize the spatial information contained in a DEM to help locate the surface trace of previously unmapped seismogenic faults (Cronin and others, 2003).

Prior research conducted by Cronin and others (2003) demonstrated that structural-geomorphic analysis of DEMs and aerial photography in a GIS format combine to provide useful information for locating previously unidentified faults. Further investigation determined that the implementation of earthquake data, in addition to geomorphic analysis of DEMs, has potential in generating location hypotheses of previously unidentified faults (Gammill and others, 2004). Bayliss and Cronin (2005) successfully tested these specific analysis techniques in the Point Dume 7.5 minute quadrangle. Some previously unmapped seismogenic faults were discovered, including one system with pure strike-slip displacement.

The objective of this project is to identify seismogenic faults within the Malibu Beach 7.5 minute quadrangle. This thesis will build upon the methods tested by Bayliss (2006) to identify faults that may be seismogenic, using high quality focal-mechanism solutions from ten earthquakes reported in or within the Malibu Beach quadrangle. This research has contributed to the development of the seismo-lineament analysis technique for locating seismogenic faults.

CHAPTER TWO

Background

Complex tectonics, active seismicity and a significant local community of Earth scientists combine to make southern California one of the most geologically investigated regions in the world. The complex tectonic regime of southern California is dominated by the relative motion of the North American and the Pacific plates across a broad boundary zone that includes the San Andreas fault as its most famous feature.

Yeats (1981) suggests that the Transverse Ranges is in motion relative to both the Pacific and North American plates. Stress in the Transverse Ranges Province is commonly attributed to the the effect of transpression through the southern restraining bend in the San Andreas fault, located roughly between Palm Springs and the southwestern San Joaquin Valley (Tsutsumi and others, 2001). The trend of the restraining bend through the Transverse Ranges is about 25° anticlockwise with respect to the right-lateral motion of the Pacific and North American plates (Cronin and Sverdrup, 1998). At Point Dume, the Pacific plate moves at a rate of about 46 mm/yr to the northwest relative to the North American plate (Cronin and Sverdrup, 1998).

Yeats (1981) and Crouch and Suppe (1993) infer that the upper crust is detached from the upper-mantle lithosphere underneath the Transverse Ranges. This detachment zone intersects with Earth's surface along the trend of two major thrust systems: the Red-Mountain-San Cayetano-Santa Susanna-Sierra Madre-Cucamonga fault zone, and

the Santa Cruz Island-MCFZ-Santa Monica-Raymond-Cucamonga fault zone (Cronin and Sverdrup, 1998).

Available paleomagnetic data suggest that the Santa Monica Mountains have rotated about 78 degrees in a clockwise direction since the early Miocene around a vertical axis (Hornafius and others, 1986). The Transverse Ranges continue to rotate at a rate of about 6 degrees per million years (fig.4; Hornafius and others, 1986; Kamerling and Luyendyk, 1979; Lajoie and others, 1979; Luyendyk and others, 1985; Luyendyk, 1991; Molnar and Gibson, 1994).

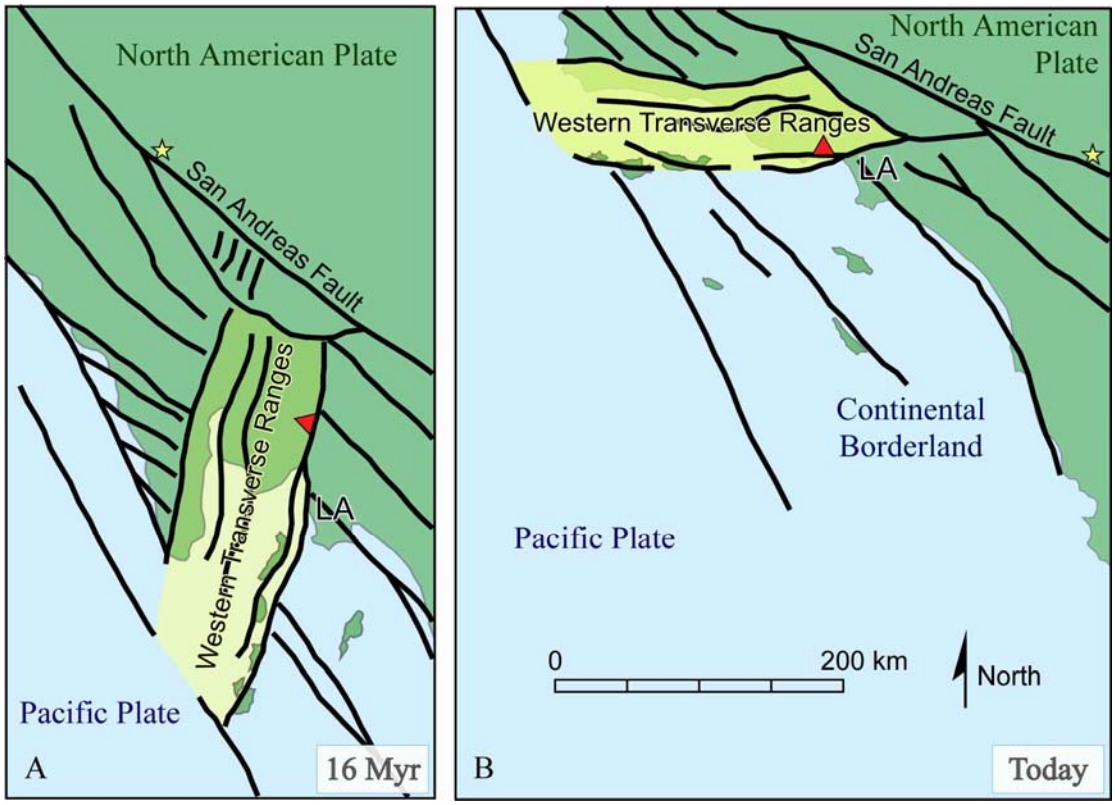

Figure 4. Neogene rotation of the central and western Transverse Ranges indicated by paleomagnetic data. Yellow star provides a reference fixed to western North America. Red triangle is approximate location of Malibu Beach quadrangle. (A) Position of the Transverse Ranges ~16 Myr. (B) Present position of the Transverse Ranges. Figure by Cronin and used with permission; modified from Hornafius and others (1996).

Several models describing the kinematics of the Transverse Ranges have been proposed. Bird and Rosenstock (1984) present a model with mantle-lithosphere downswelling to a depth of 250 km underneath the Transverse Ranges. Nicholson and others (1994) present a model for basal shear as the cause of the rotation of the western Transverse Ranges. Fuis and others (2003) infer from the results of the Los Angeles Reflection Seismic Experiment (LARSE) that the western Transverse Range block is thrust over the blocks of the Continental Borderland/Peninsular Ranges. Legg and others (2004) suggest basal shear caused by thrusting the western Transverse Ranges block over the Continental Borderland as the mechanism for rotation of the western Transverse Ranges.

The Transverse Ranges experience rates of uplift of about 4 to 10 mm/yr (Kamerling and Luyendyk, 1979; Lajoie and others, 1979; Luyendyk and others, 1985; Luyendyk, 1991). Pinter and others (1998) attribute this uplift to a combination of the reverse slip component of the Dume, Malibu Coast, and Santa Monica faults and slip on a blind (non-emergent) thrust fault.

The combination of geomorphic, seismic, and geodetic records suggest that the western Transverse Ranges are a structurally active feature and pose a seismic hazard to the regional population (Ziony and Yerkes, 1985; Hauksson and Saldivar, 1989; Hauksson, 1987; Wesnousky, 1986; Dolan and others, 1995; Larson, 1993; Molnar and Gibson, 1994). Jackson and Molnar (1990) describe earthquakes that have a combination of thrust and strike-slip motion in the western Transverse Ranges. Faults that do not extend to the ground surface pose a considerable threat to humans and property because they are not recognized as seismic hazards. For example, the Northridge earthquake (M

6.7; January 17, 1994) occurred on a previously unmapped blind thrust fault that dips underneath the San Fernando Valley.

The Malibu Coast Fault Zone (MCFZ) is part of a system of faults exhibiting late Neogene activity that trend east-west and form the southernmost boundary of the Transverse Ranges Province. Other faults in that system include the Santa Cruz Island, Santa Rosa Island, Santa Monica, Hollywood, Raymond, and Cucamonga faults (*e.g.,* fig. 1; Cronin and Sverdrup, 1998; Fisher and others, 2005). The MCFZ "includes the Potrero fault, the various strands of the Malibu Coast fault (*e.g.,* Puerco Canyon fault, Ramirez thrust, Escondido thrust, Point Dume fault, Latigo fault, Solstice fault, Paradise Cove fault), the Anacapa fault ('Dume fault' of Junger, 1976), Fault Z, and several unnamed offshore faults interpreted from marine geophysical data" (Cronin and Sverdrup, 1998). The faults at the southern edge of the western Transverse Ranges are north dipping and generally have both a thrust and left lateral strike-slip component. The reverse slip component of the MCFZ fault is apparent in the geomorphic change in slope along the coastline.

The Malibu Coast fault is one of several strands of the MCFZ. Cronin and Sverdrup (1998) define the Malibu Coast fault as "the structurally interrelated fault strands that have been active during the Quaternary and that are located within ~3 km of the Malibu coastline between longitudes 118.5° and 119° W". The Malibu Coast fault typically dips between 30 to 70 degrees to the north (Cronin and Sverdrup, 1998). The total left-lateral strike-slip displacement of the Malibu Coast-Santa Monica fault zones is estimated to be 60 to 90 km since Miocene time (Lamar, 1961; Yeats, 1968; Colburn, 1973; Sage, 1973; Campbell and Yerkes, 1976; Link and others, 1984; Hornafius and

others, 1986; Yerkes and Lee, 1987). The total vertical displacement along the Malibu Coast fault has not been described (Cronin and Sverdrup, 1998).

In the state of California, a fault is legally defined as active if a trench study reveals fault displacement of Holocene-age material – material that is less than 11,000 years old -- on or near the ground surface (Hart and Bryant, 1999). Previously conducted trench studies have yielded contradictory results, variously indicating that the main strand of the Malibu Coast fault is active (Drumm, 1992) and inactive (Leighton and Associates, 1989; Treiman, 1994). The result of this inconsistency is that the Malibu Coast fault is not legally considered active in its entirety. Even so, two short segments of the Malibu Coast fault zone are legally defined as active as designated by the Alquist-Priolo Act: the Winter Mesa and Soltice strands of the MCFZ (fig. 2; Cronin and Sverdrup, 1998; Hart and Bryant, 1999). All of the Winter Mesa strand and part of the Solstice strand are located within the Malibu Beach 7.5 minute quadrangle. Faults along the trend of the Malibu Coast and Santa Monica fault zones are capable of producing M 7.0 earthquakes (Dolan and others, 1995; Cronin and Sverdrup, 1998). Seeber and Sorlien (2000) suggest that faults in the region are capable of producing earthquakes that are beyond the magnitudes of any earthquakes in the historical record for this trend.

In addition to the Mailbu Coast fault, the Anacapa-Dume fault zone is also a part of the MCFZ. Sorlien and others (2003) suggest that the Dume fault (the offshore segment of the MCFZ) and the Malibu Coast fault merge at depth. They infer that this system produced the 1973 Point Mugu earthquake (M 5.3) and associated aftershocks (Sorlien and others, 2003).

To the south of the western Transverse Ranges Province are the northwest-trending ridges and basins of the Continental Borderland (Wright, 1991). A system of right-lateral strike-slip faults trend northwest through the Continental Borderland and Penisular Ranges. This system of right-lateral strike-slip faults comprise the onshore Newport-Inglewood, Whittier-Elsinore, and San Jacinto faults of the Peninsular Ranges, and the offshore faults of Santa Rosa-Cortes Ridge, San Clemente Island, San Pedro Basin, and Rose Canyon faults of the Continental Borderland. These faults are overthrust or terminate at the east-west trending faults of the Transverse Ranges Province. While the Transverse Ranges rotate, the Continental Borderland experiences right-slip and crustal extension (Legg and others, 1994; Crouch and Suppe, 1993; Bohannon and Parsons, 1995).

Rock exposures in the Santa Monica Mountains are composed of sedimentary rocks that are Cretaceous to Pleistocene in age, and middle Miocene volcanic rocks (Blake, 1991; Dibblee, 1993; Fisher and others, 2005; Wright, 1991; Yerkes and Campbell, 1980). Published geological mapping includes the work of Campbell and others (1996), Hoots (1931), McGill (1982); Yerkes and Campbell (1980), Yerkes and Wentworth (1965), and Yerkes and others (1971). Early to middle Miocene age rock units in the Santa Monica Mountains include the marine Vaqueros formation and Topanga Canyon formations, and the non-marine Sespe formation, Fernwood member and Piuma member (Yerkes and Cambell, 1980). The basement rock of the Santa Monica Mountains is the Catalina Schist.

CHAPTER THREE

Methods and Analytical Techniques

Data Collection

A collection of published geologic and topographic maps of the Malibu Beach 7.5 minute quadrangle and of the Santa Monica Mountains was acquired, including *Geologic map of the Point Dume quadrangle, Los Angeles County, California* (Campbell and others, 1996), *Geologic map of east-central Santa Monica Mountains, Los Angeles County, California* (Yerkes and Campbell, 1980), and the *Geologic map of the Malibu Beach Quadrangle, Los Angeles County, California* (Dibblee, 1993). A set of digital information, published by the USGS, concerning the structure and geology of the study area was also acquired and is available at http://geopubs.wr.usgs.gov/open-file/pf97-257/ and http://geonsdi.er.usgs.gov/metadata/open-file/97-257/metadata.faq.html. Digital elevation models (DEM) with 10- and 30- meter resolution used in this thesis were created by the USGS and are available at http://earthquake.usgs.gov/regional/states/california/northridge10m_DEMs.php. Google Earth, available at http://earth.google.com/, provides high resolution aerial coverage of the central Santa Monica Mountains.

A digital geographic information systems (GIS) database was built by compiling 10- and 30-meter DEMs, published digital geologic maps, earthquake projections plots, and culture (*e.g.,* roads and trails) of the Malibu Beach 7.5 minute quadrangle. All of the digital data were integrated into an ESRI *ArcGIS 9.0* mapping layer in order to prepare for seismo- and geomorphic lineament analysis within the study area.

The earthquake data used in this project were taken from an earthquake catalog compiled by Cronin (http://www3.baylor.edu/~Vince_Cronin/MalibuCurrentEQFile.xls; Cronin and Sverdrup, 1998). This catalog contains over 1000 earthquake events with reported epicenters along the Santa Monica Mountains and the northern Santa Monica Bay, including about 150 focal mechanism solutions to associate earthquake data with unmapped faults. Focal mechanism solutions were compiled from Buika and Teng (1979), Hardebeck (2005), Hauksson (1990, 2000, 2004), Hauksson and Saldivar (1986), Lee and others (1979), Stierman and Ellsworth (1976), and Webb and Kanamori (1985).

Geomorphic Lineament Analysis

In their study of lineaments in the Nanga Parbat-Haramosh Massif of the northwest Himalaya, Cronin and others (1993, p. 196) define a lineament as "a long (generally ≥ 5 km) colinear or slightly curving array of stream drainage segments or tonal boundaries within the Landsat mosaic that does not appear to be related to human construction or other [human] activities." It is convenient to define two categories of lineaments for studies in the Santa Monica Mountains, based on scale: *local lineaments* and *composite lineaments* (Cronin, 2004c). *Local lineaments* are between 0.5 and 2 kilometers in length, and *composite lineaments* are longer features that may extend 10 kilometers or more. In practice, local lineaments are identified first and are subsequently used to define composite lineaments. Criteria for identifying local lineaments include the following (Wesson and others, 1975; Cronin and others, 1993; McCalpin 1996; Burbank and Anderson, 2001; Keller and Pinter, 2002; list is from Cronin, 2004c, and isused with permission):

a. stream channels aligned across a drainage divide

b. lower-order (smaller) stream channels aligned across a higher-order stream channel

c. a long, straight segment of a stream channel

d. aligned straight segments of a stream channel

e. a lower-order stream channel whose trend is directed upstream relative to the higher-order stream it intersects, so that water flowing from the smaller stream into the larger stream has to change directions through an acute angle.

f. an abrupt change in gradient along a stream channel

(1) a stream channel that steps down in the direction of flow, evinced by rapids or a waterfall (*i.e.,* a knick point)

(2) a stream channel that steps up in the direction of flow, evinced by a pond

g. apparent lateral deflection of an incised stream channel or flood plain

h. abrupt changes in gradient along a ridge crest

(1) a ridge crest that steps down abruptly in the direction the ridge is decreasing in elevation

(2) a ridge crest that steps up in the direction the ridge is decreasing in elevation

(3) a saddle in the ridge crest

i. apparent lateral deflection of a ridge crest

j. abrupt changes in the gradient of a surface localized along a narrow linear step (*i.e.,* a fault scarp)

k. benches or faceted spurs at the base of ridges that are unrelated to coastal erosion.

l. a set of ridges in an *en echelon* array

m. a topographic basin along a linear trough (*i.e.,* a pull-apart basin or a sag pond)

n. a topographic hill along a linear trough (*i.e.,* a pop-up or a pressure ridge)

o. a ridge across the mouth of a stream drainage that is not a glacial moraine (*i.e.,* a shutter ridge)

In this thesis, a 10-meter resolution DEM of the study area was used to identify lineaments that may be associated with potential seismogenic structures (Cronin and others, 1993, 2003). The DEM of the Malibu Beach 7.5 minute quadrangle is added to an *ArcGIS* mapping layer for geomorphic lineament analysis. The primary advantages of using a DEM for geomorphic analysis, compared with an aerial photograph, are (1) a DEM contains only information about the shape of the ground surface, and (2) a DEM can be represented as a surface illumined from any direction or elevation. Aerial photographs contain distracting cultural and landscape artifacts (roads, buildings, vegetation) and have a fixed direction of solar illumination.

The DEM was illumined from an elevation of 45° and from a number of different directions, using *ArcGIS* version 9.0. The analysis of the entire Malibu Beach 7.5 minute quadrangle was conducted with illumination from due north (0°), 45°, 90°, 135°, 180°, 270°, and 315°. Each image was saved in JPEG format and imported to ACD Canvas, which is an application that can operate on raster and vector graphics.

For a given JPEG, all of the local lineaments are mapped within a one-by-one inch grid spacing. After all of the lineaments are mapped within this grid, the grid is moved by one-half of an inch. This process is repeated until the entire DEM is examined for local lineaments. During this process, no maps or other images are consulted. The process is then repeated, using the same steps. The resulting two maps of geomorphic lineaments are compared to each other to test the reproducibility of lineament

recognition. The lineaments are evaluated to make sure that they are not a geomorphic representation of a man-made structure (*e.g.,* roads and trails). The remaining lineaments are then compiled into a lineaments map. Composite lineaments are then identified using these maps of local lineaments (fig. 5). The map of composite lineaments is used to generate fault-location hypotheses and to guide field work.

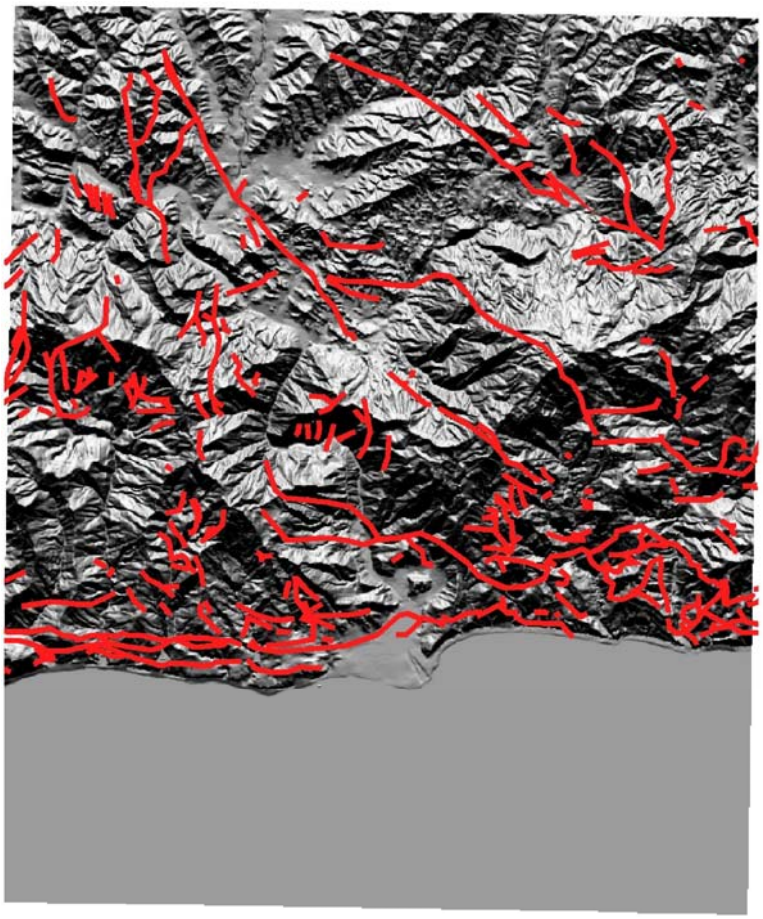

Figure 5. Previously mapped faults (red) within the Malibu Beach 7.5 minute quadrangle (Campbell and others, 1996).

Seismo-Lineament Analysis

This thesis applies a method developed by Cronin (2004b), which involves exploring the potential for seismogenic faults in the study area by using published

earthquake focal-mechanism solutions. Background information about focal mechanism solutions is provided in a web-accessible primer by Cronin (2004a). Focal mechanism solutions for ten earthquakes with reported locations near the Malibu Beach quadrangle were used in this study (fig. 6).

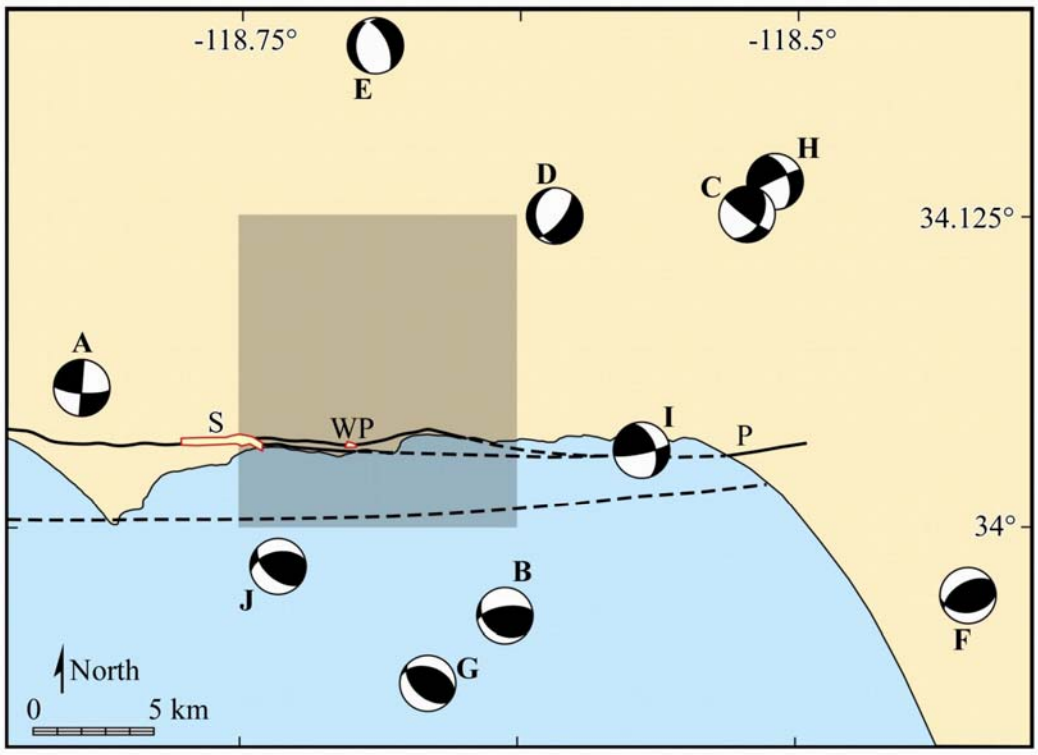

Figure 6. Focal mechanism solution diagrams for ten earthquakes reported near or within the Point Dume, Malibu Beach (gray), and Topanga 7.5 minute quadrangles. Focal mechanism solution data from Hardebeck (2003) and Hauksson (1990, 2004). Earthquake date and origin time is used as an identifier: yyyyMMddhhmm.
(A) Earthquake 20031031010718, reported magnitude 2.94, focal depth 11.18 km.
(B) 19940217161359, M 2.62, 13.82 km. (C) 20000316095007, M 1.93, 8.51 km.
(D) 19810812225800, M 2.7, 3.3 km. (E) 19941026041847, M 2.4, 4.66 km.
(F) 20000916132441, M 3.27, 11.09 km. (G) 19860520071140, M 2.79, 13.48 km.
(H) 20030328054413, M 2.91, 6.75 km. (I) 19831123120100, M 2.5, 8.1 km.
(J) 19930726212949, M 3.6, 15.04 km.

The focal-mechanism solution for each earthquake includes the orientation of two nodal planes oriented 90° from one another. One of the nodal planes is parallel to the

fault that generated the earthquake, while the other plane is the auxiliary plane along which there was no shear displacement during the earthquake. The focal-mechanism solution alone does not provide enough data to differentiate between the fault plane and the auxiliary plane, so additional geological data are required. The vector normal to one nodal plane coincides with the slip vector of the potential fault-plane solution represented by the other nodal plane, so each focal mechanism solution yields the orientation of two possible fault-plane solutions and their respective slip vectors (Cronin, 2004a).

Cronin's method projects one of the nodal planes from the earthquake focus toward the ground surface represented by the DEM, and defines the intersection of those two surfaces (fig. 7).

Figure 7. Focal-mechanism solution "beach ball" diagram for a magnitude 2.9 earthquake recorded on October 31, 2003 at a depth of 11.2 km (Hauksson, 2004). The red curves are the surface traces of the two nodal planes across the ground surface, represented by the DEM image. The focal-mechanism solution includes information about the orientation and slip direction associated with each nodal plane, one of which is inferred to coincide with the fault that produced the earthquake. From Gammill and others (2004).

For cases in which an estimate of the uncertainty in focal location is available, that uncertainty is used to define an envelope around the nodal plane, which intersects the DEM in a swath (fig. 8). The intersection of the nodal plane or its associated uncertainty region with the DEM is called a *seismo-lineament*. The underlying idea is that the most likely location of a seismogenic fault associated with that earthquake, if that fault is exposed at the ground surface, will be within the seismo-lineament defined by one of the two nodal planes. Geological field work is subsequently undertaken to explore for faults within each seismo-lineament that have an orientation and sense of slip that is similar to the corresponding nodal plane.

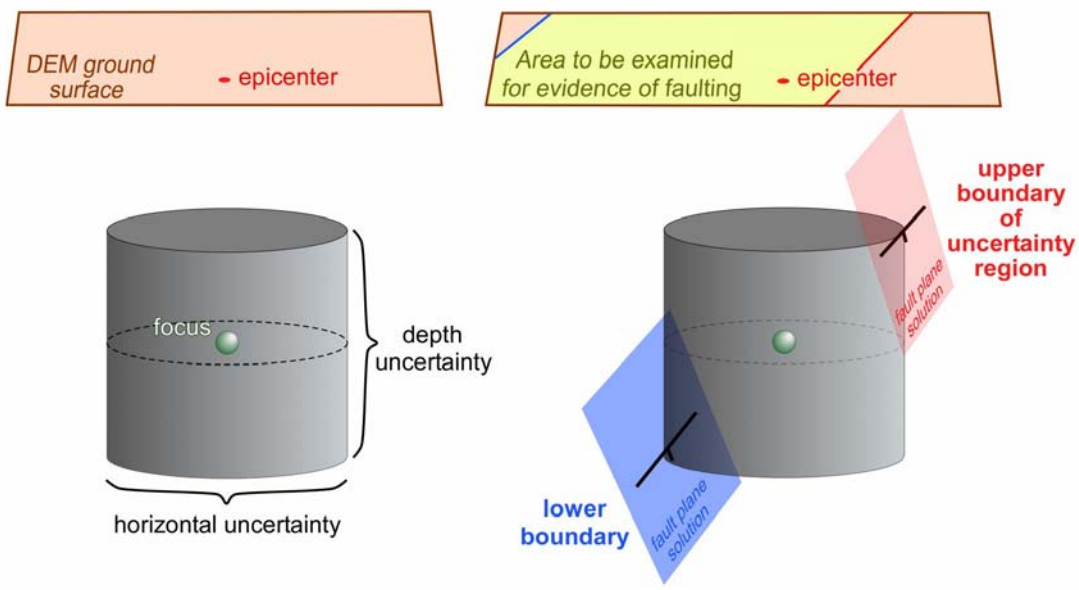

Figure 8. Three-dimensional representation of the seismo-lineament swath. The swath is defined by the projected fault plane solutions, which have both a vertical and horizontal uncertainty and are bounded by both the upper and lower boundary of the uncertainty region.

Cronin's seismo-lineament analysis method requires the following data input to a *Mathematica* notebook application: a DEM, typically at 30-meter resolution; the

latitude, longitude, and depth of the earthquake focus; the vertical and horizontal uncertainty in the focal location; the orientation of one of the two focal mechanism solution nodal planes; and the rake of the slip vector associated with the earthquake event (Cronin, 2004c). The *Mathematica* code projects the uncertainty region around the nodal plane up to the DEM surface to produce a map of the seismo-lineament swath.

The location of the earthquake focus is input as the latitude and longitude of the earthquake epicenter and the reported focal depth in kilometers. These data are converted to UTM coordinates $\{x_{\text{focus}}, y_{\text{focus}}, z_{\text{focus}}\}$ in meters, using the method described by Snyder (1982). The z_{focus} value is negative when the focus is below sea level (Cronin, 2004b). The rake of the slip vector is the angle between the slip vector and the reference strike of the fault. A negative rake indicates a normal (hanging-wall down) component of slip, and a positive rake indicates a reverse component of slip. The reference strike is 90° anticlockwise from the trend of the dip vector (Cronin, 2004a).

The remainder of this section is a description of how the *Mathematica* notebook application defines a seismo-lineament. The code is reproduced in Appendix A. This description is quoted *verbatim* from Cronin (2004c), and is reproduced here with permission.

"The first several records in the DEM contain header data that define the number of rows (*nrows*) and columns (*ncols*) in the matrix of elevation data, the UTM coordinates of the lower-left corner ($x_{\text{llcorner}}, y_{\text{llcorner}}$), the horizontal distance between adjacent elevation data (*cellsize*), and the value used to indicate "no data" within the matrix (Maune, 2001). The matrix of elevation data follows the header, with the horizontal coordinates of each elevation datum implied by its location within the matrix. The UTM

coordinates of the datum in row i and column j of the matrix (where $i = 1$ for the first row of elevation data) are

$$x \text{ coordinate} = x_{\text{llcorner}} + ((cellsize)\,(j - 1)) \tag{1a}$$

$$y \text{ coordinate} = y_{\text{llcorner}} + ((cellsize)\,(nrows - i)) \tag{1b}$$

and the z coordinate (*i.e.*, the elevation) is the value that occupies position $[i, j]$ of the matrix.

Data derived from the focal mechanism solution are used to define several vector quantities needed in the analysis. The unit vector along the fault dip (*dipVector*) is computed using the plunge and trend of the fault dip:

$$dipVector = \{\cos(\text{plunge})\sin(\text{trend}), \cos(\text{plunge})\cos(\text{trend}), -\sin(\text{plunge})\}. \tag{2}$$

The unit vector associated with the reference strike of the fault plane is

$$strikeVector = \{\sin(\text{trend} - 90°), \cos(\text{trend} - 90°), 0\}. \tag{3}$$

The unit vector normal to the fault plane (**N**) is defined by the vector cross product

$$\mathbf{N} = dipVector \times strikeVector. \tag{4}$$

The UTM coordinates associated with the DEM are transformed by rigid translation to a coordinate system whose origin is coincident with the earthquake focus. The transformed coordinates of the datum in row i and column j of the data matrix are

$$x_{(i,j)\text{trans}} = (\text{cellsize} * (j - 1)) + (x_{\text{llcorner}} - x_{\text{focus}}) \tag{5a}$$

$$y_{(i,j)\text{trans}} = (\text{cellsize} * (\text{nrows} - i)) + (y_{\text{llcorner}} - y_{\text{focus}}) \tag{5b}$$

$$z_{(i,j)\text{trans}} = \text{elevation}_{(i,j)} - z_{\text{focus}} \tag{5c}$$

where $\text{elevation}_{(i,j)}$ is the value in row i, column j of the original data matrix. The vector $\mathbf{L}_{i,j} = \{x_{(i,j)\text{trans}}, y_{(i,j)\text{trans}}, z_{(i,j)\text{trans}}\}$ is the location vector to the point at row i and column j of

the transformed data matrix, relative to a coordinate-system in which the origin is coincident with the earthquake focus.

The distance between the fault plane and the point on the DEM surface associated with location vector $\mathbf{L}_{i,j}$, in meter units, is the result of the vector dot product

$$d_{i,j} = \mathbf{N} \bullet \mathbf{L}_{i,j} \quad (6)$$

(fig. 9a). For a fault plane with a dip angle of δ passing through a focal point whose location is known plus-or-minus some vertical error (v_e in meters) and horizontal error (h_e in meters), the half-width of the uncertainty envelope (w_e) is given by

$$w_e = [v_e * \cos(\delta)] + [h_e * \sin(\delta)] \quad (7)$$

(fig. 9b). Any point on the DEM for which the distance to the reported fault plane is less than or equal to the half-width of the location uncertainty envelope is considered to lie within the seismo-lineament swath that will be the focus of field evaluation."

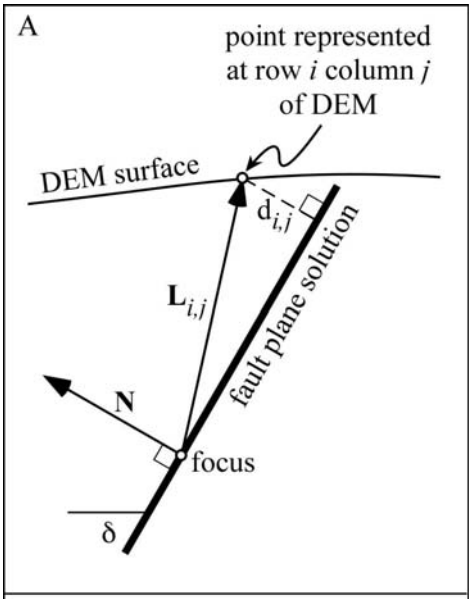

Figure 9. (A) Cross section of the vector and fault plane geometry used in Cronin's seismo-lineament method (Cronin, 2004). Angle δ represents the dip of the fault. Unit vector **N** is normal to the fault plane. Location vector $\mathbf{L}_{i,j}$ is directed toward a point on the DEM surface that is $d_{i,j}$ meters away from the fault plane.

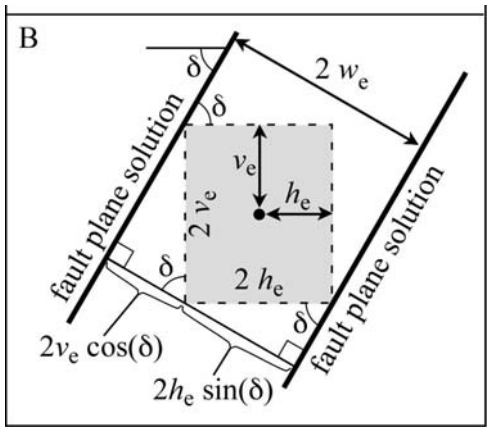

Figure 9. (B) Cross section showing the uncertainty region (gray box) around the earthquake focus (black dot) bracketed by parallel fault-plane solutions. Length v_e is the uncertainty in focal depth, h_e is the horizontal uncertainty in focal location, and w_e is the half-width of the uncertainty envelope between the fault planes. This figure is copyright (2006) by Cronin and used here with permission.

Geomorphic Lineament Analysis Along Seismo-Lineaments

The 10-meter resolution of DEMs of individual seismo-lineament swaths were illuminated from an elevation of 45°, and from various azimuth directions measured relative to the strike of the corresponding nodal plane: ±90°, ±60°, ±30°, and ±15°. Appendix B presents the sun angles used for each of the individual seismo-lineament swaths. Within each of the seismo-lineament swaths, geomorphic lineaments were preferentially identified with the same general orientation as the seismo-lineament. Figure 10 presents how a DEM looks when it is illuminated from different angles. In this figure four images of the DEMs of seismo-lineament swath 200310310718a are illumined at 45º elevation from different directions. Different illumination directions accentuate geomorphic features differently.

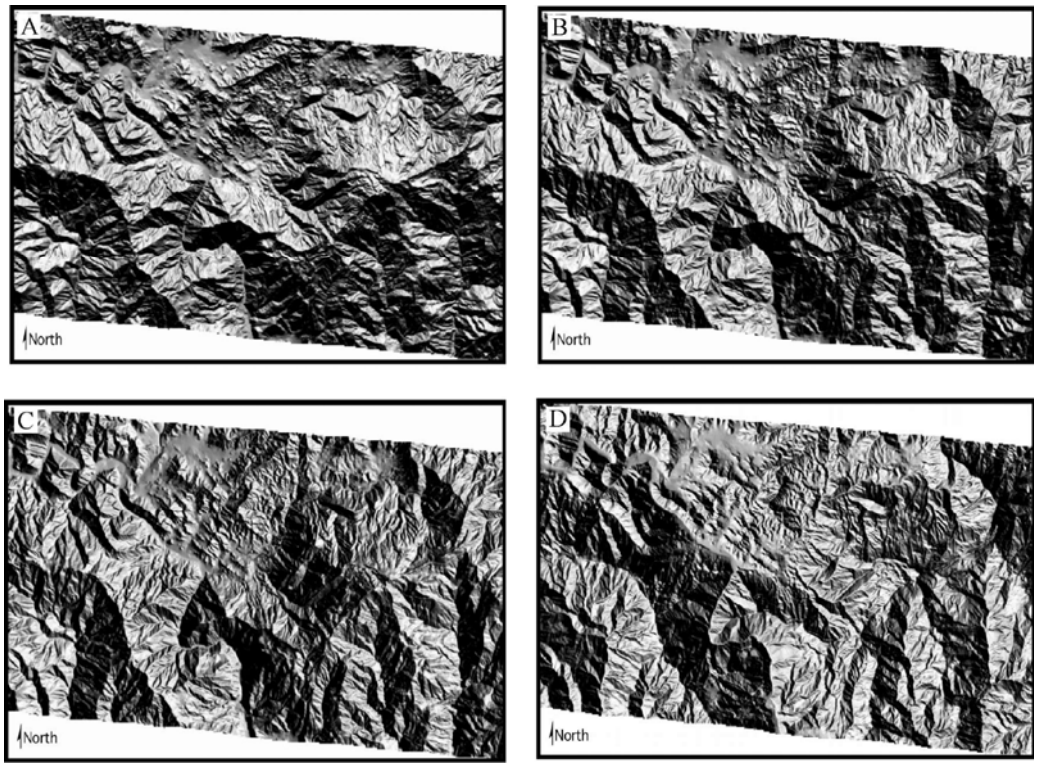

Figure 10. The images are illuminated from azimuths of (A) 15°, (B) 45°, (C) 75° and (D) 245°.

Field Work

Geomorphic lineament analysis generates hypotheses concerning the possible location of structures along the ground surface that have an influence on the morphology of that surface, and seismo-lineament analysis generates hypotheses about the possible location of the surface trace of seismogenic faults. Field work is used to evaluate these hypotheses in order to locate actual faults. Fault-location hypotheses are tested in the field by traveling to the location where a geomorphic or seismo-lineament crosses a road or trail and looking for physical evidence of a fault (Cronin, 2004c). At these locations the ground surface within a seismo-lineament swath was examined for evidence of faulting (*e.g.,* fig. 11).

Figure 11. Example of a fault identified in the field. The light-toned block on the left is displaced downward relative to the block on the right, along a fault surface that is nearly parallel to the outcrop face. The fault surface above the geologist has shear striations.

Active faults are marked by zones of brittle deformation at or near the ground surface, featuring zones of gouge, breccia, or cataclasite that are bounded by striated and polished surfaces on either side of the fault zone (fig. 12; Chester and others, 2004). A fractured damage zone often extends beyond the fault zone into the rock on either side. Offset geological objects (*e.g.*, clasts in a conglomerate, macrofossils) or surfaces (*e.g.*, beds, joints, igneous intrusions, older faults, the ground) may permit quantification of

offset along a fault. The location and orientation of faults identified in the field were compared with faults included in published geological maps to determine whether the faults identified in the field have previously been recognized.

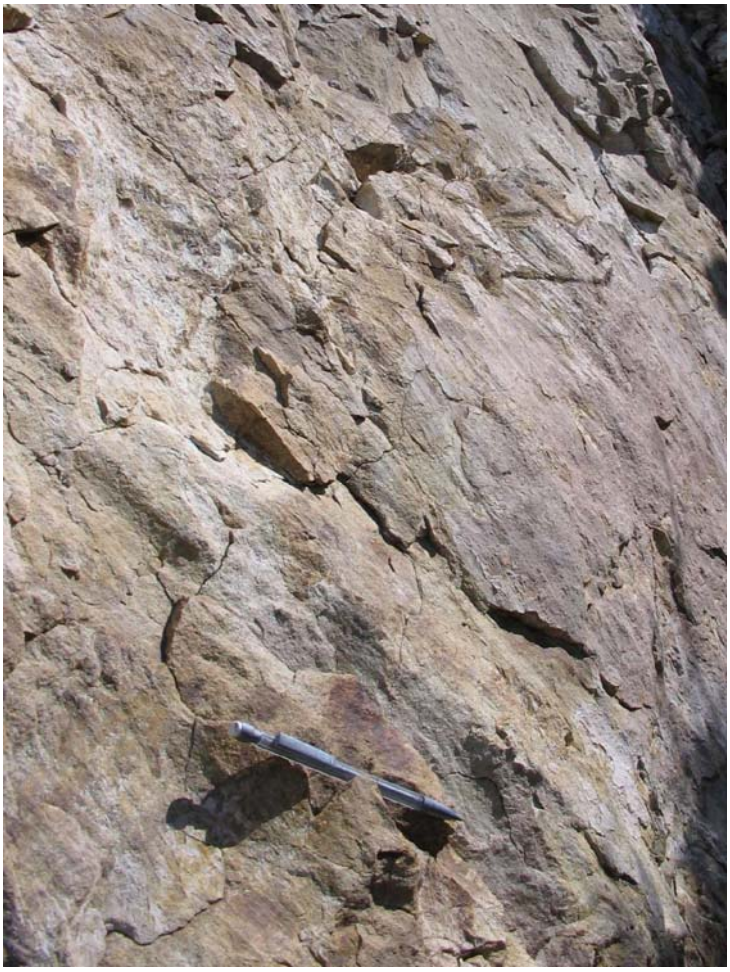

Figure 12. Typical example of an exposed fault surface, displaying the shear striations and grooves that indicate the general direction of most recent fault motion along this surface. Pencil is for scale.

Prior to conducting field work, a list of information to be obtained at every faulted outcrop/roadcut was compiled. The following data are collected when a fault is identified in the field:

a. GPS and topographic map location

b. type of outcrop exposure (*e.g.,* roadcut or natural outcrop)

c. physical description of the rock unit

d. photographs, complete with scale

e. basic fault description

f. record of the type of slip-sense indicator (*e.g.,* Reidel shear, slickenfiber, offset marker, or indeterminate)

g. oriented fault samples

h. fault-rock description and color

i. fault width measurement, with associated uncertainty

j. offset of fault, with associated uncertainty

k. damage zone description

l. description of rock on both sides of the fault (*e.g.,* structural condition, lithology, formation, and orientation)

m. observations regarding the geomorphic effect of the fault (*e.g.,* scarp or drainage localization), and

n. documentation of the involvement of a fault in a landslide event.

Approximately 7 to 12 measurements of the orientation of each fault surface were made with a Brunton compass. Typically, each measurement included the strike azimuth, dip angle, and the direction of dip of the surface. Fault surfaces were recognized from the presence of shear striations (slickenlines). In cases where there was a gouge zone of significant thickness, the orientation of the boundary surface between the gouge and the surrounding rock was measured. The orientation of more than 7 shear striations was also

collected, generally by measuring the rake of the striation relative to the reference strike of the striated surface.

Evidence was sought to indicate the direction of slip along the striation; however, interpretation of slip was commonly ambiguous in the absence of clear displaced markers on opposite sides of the fault. Oriented samples were collected along the fault for later microscopic analysis in hopes of finding microstructures that may indicate shear direction. If the hanging-wall slip direction cannot be determined directly, but can be inferred by context, then it was documented in the field notes. However, if the hanging-wall slip direction cannot be determined either through outcrop evidence or inferred from context, the shear striation was considered to be a line (not a vector).

Fisher Statistics

R.A. Fisher developed a method for describing the spatial statistics for a set of vectors that are expected to have a unimodal distribution, as is characteristic of paleomagnetic vectors (Fisher, 1953). Cronin (2007) adapted this method for use in defining the average orientation of geological surfaces, along with the associated statistical uncertainty. The fault-orientation data and the orientation of shear striae were analyzed using Fisher statistics. Surface orientations were represented as the trend and plunge of the corresponding dip vector. Uncertainties in these sets of vector data were computed to a 90% confidence interval, to make them comparable with the 90% confidence interval associated with some of the earthquake data used to define the seismo-lineaments. Appendices C and D present worked Fisher statistical examples with actual field data.

Criteria for Recognition of Seismogenic Faults

The seismo-lineament maps each define a swath within which the surface trace of a fault associated with that earthquake might be found. Field work was undertaken in these areas to look for faults, and to document the orientation of the sheared surfaces and slip directions for faults that were encountered. Average orientations of these faults and slip directions, and an assessment of the associated uncertainties, were obtained using Fisher statistics. Where the uncertainty region for the orientation of the observed fault overlaps with the orientation (or orientation uncertainty region) of the fault-plane solution that defines the seismo-lineament, the fault and the fault-plane solution are said to have a similar orientation. In the same way, the orientation of observed shear striae and the orientation of the appropriate slip vector from the focal-mechanism solution are compared. Stereonet plots were made for all fault mean orientations and rakes of both earthquakes and faults identified in the field, with the respective 90% confidence intervals.

The criteria for identifying a fault that is inferred to be seismogenic are as follows. (1) The surface trace of the fault must be located within the corresponding seismo-lineament. (2) The orientation of the fault must be similar to the orientation of the corresponding fault-plane solution. (3) The orientation of the shear striae on the fault must be similar to the orientation of the slip vector associated with the corresponding fault-plane solution.

CHAPTER FOUR

Results

Seismo-Lineament Analysis

Ten seismo-lineaments were evaluated in the Malibu Beach 7.5 minute quadrangle, corresponding to nodal planes from earthquakes 200310310718a, 20030328054413a, 19810812225800a, 2000316095007a, 20000916132441a, 198311231020100a, 19940217161359a, 19930726212949a, 19941026041847a, and 198605200740a. The earthquake labels incorporate the origin date/time of the earthquake (yyyyMMddhhmm) and an identifier for the nodal plane (a or b). All ten seismo-lineaments intersect the ground surface within the Malibu Beach 7.5 minute quadrangle. All ten seismo-lineaments are presented together in Figure 13.

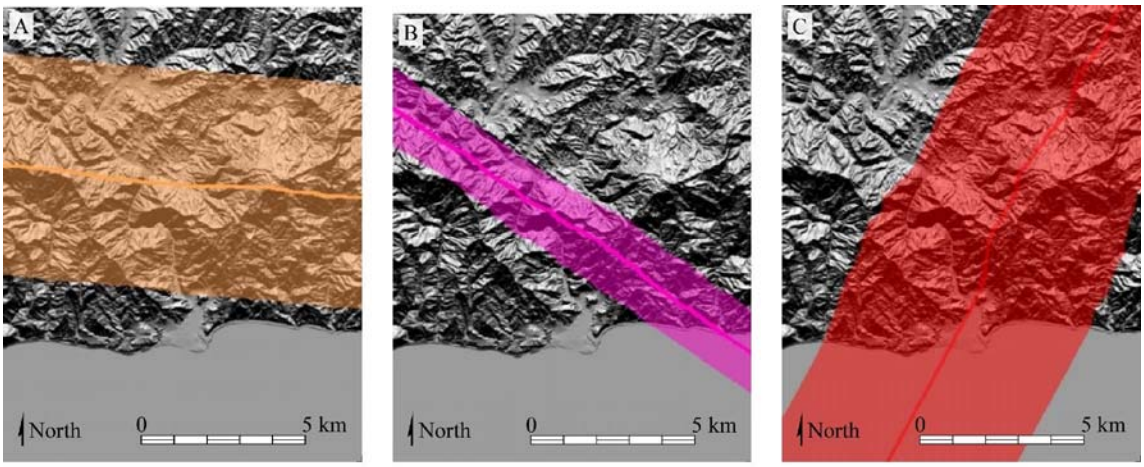

Figure 13. Colored bands indicate locations of seismo-lineaments investigated in this study, projected onto an image of the Malibu Beach 7.5 quadrangle DEM. This figure is continued onto the next page. Earthquake date and origin time is used as an identifier: yyyyMMddhhmm. (A) Seismo-lineament 20031031010718a. (B) 19940217161359a. (C) 20000316095007a.

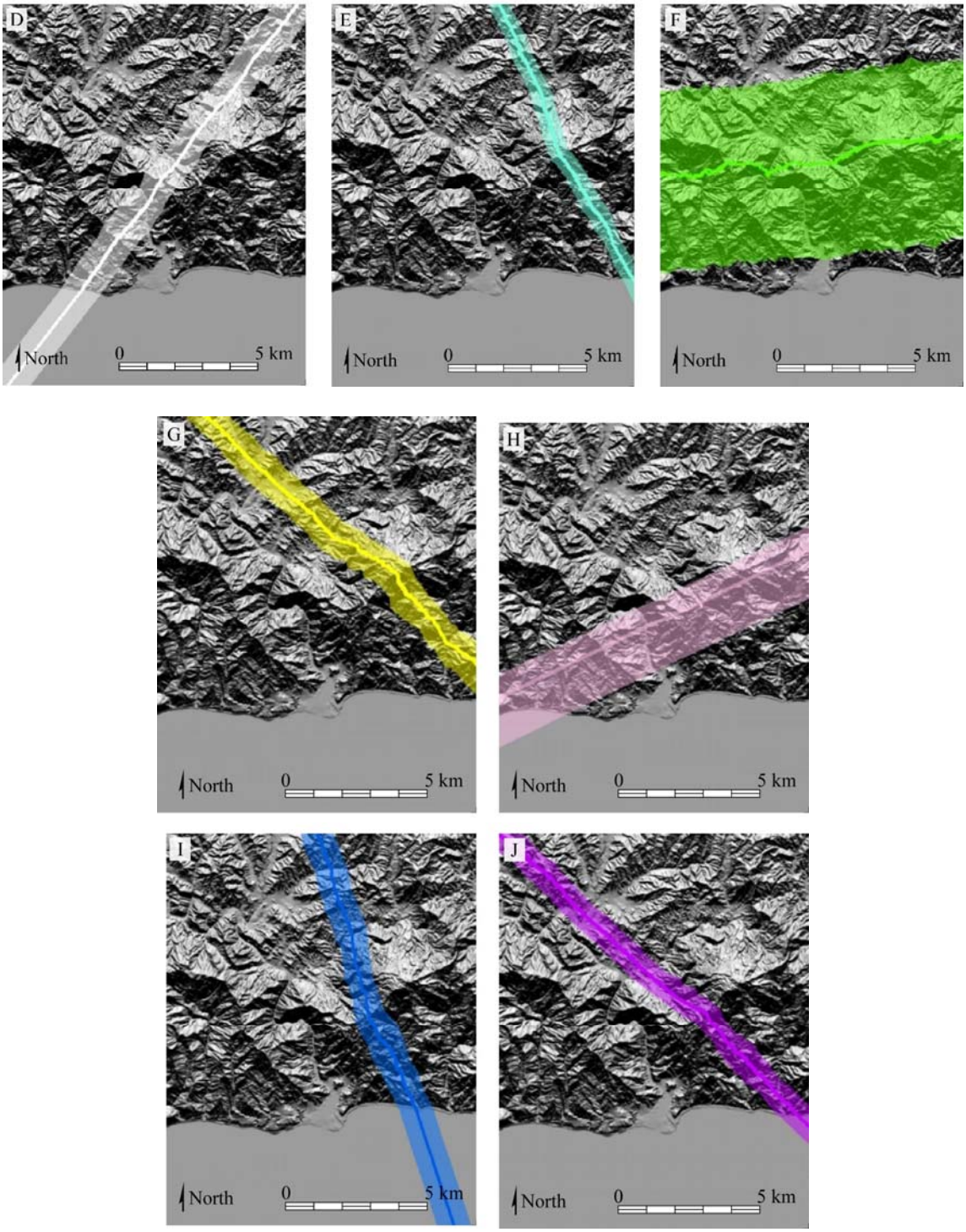

Figure 13, continued from previous page. (D) Seismo-lineament 19810812225800a. (E) 19941026041847a. (F) 20000916132441a. (G) 19860520071140a. (H) 20030328054413a. (I) 19831123120100a. (J) 19930726212949a.

The width of the seismo-lineament swath is a function of the dip of the nodal plane (the steeper the plane, the thinner the swath) and the reported 95% confidence interval for the earthquake location (the smaller the uncertainty region for the focus, the thinner the swath). Complete information for each focal mechanism solution is presented in Appendix E.

Geomorphic Lineament Analysis

Many geomorphic lineaments were recognized within the Malibu Beach 7.5 minute quadrangle (fig. 14). These figures show geomorphic lineaments with the same general orientation as the seismo-lineament swath.

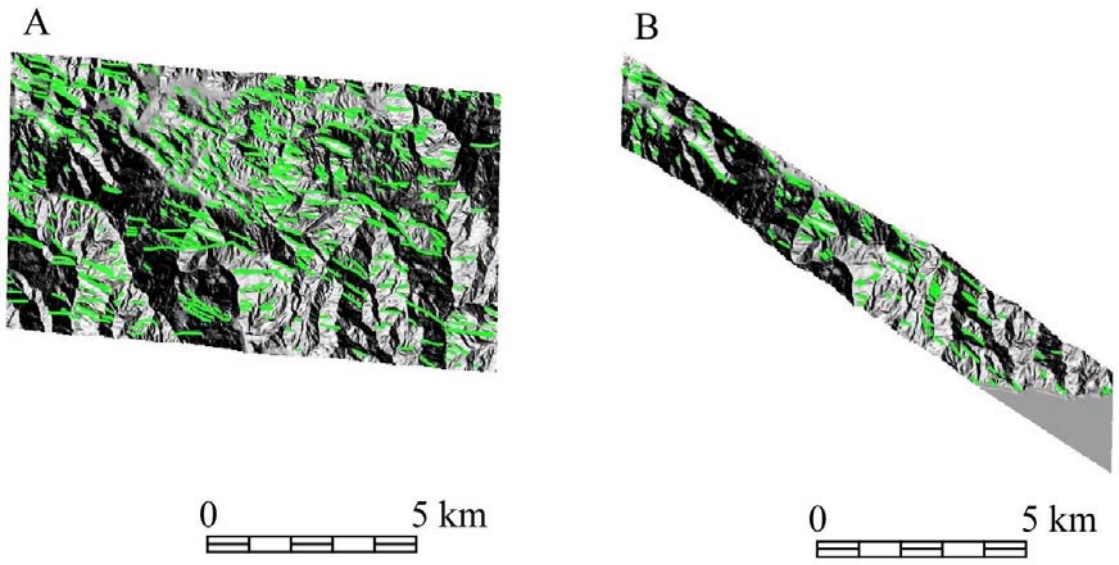

Figure 14. Geomorphic lineaments (green) traced onto DEM images of the ten seismo lineaments. Faults associated with each seismo-lineament would be expected to have approximately the same strike as the seismo-lineament. This figure is continued onto the next page. (A) Seismo-lineament 2003103101071a with DEM illumined from 245°, -30° to strike. (B) 19940217161359a illumined from 243°, 30° to strike.

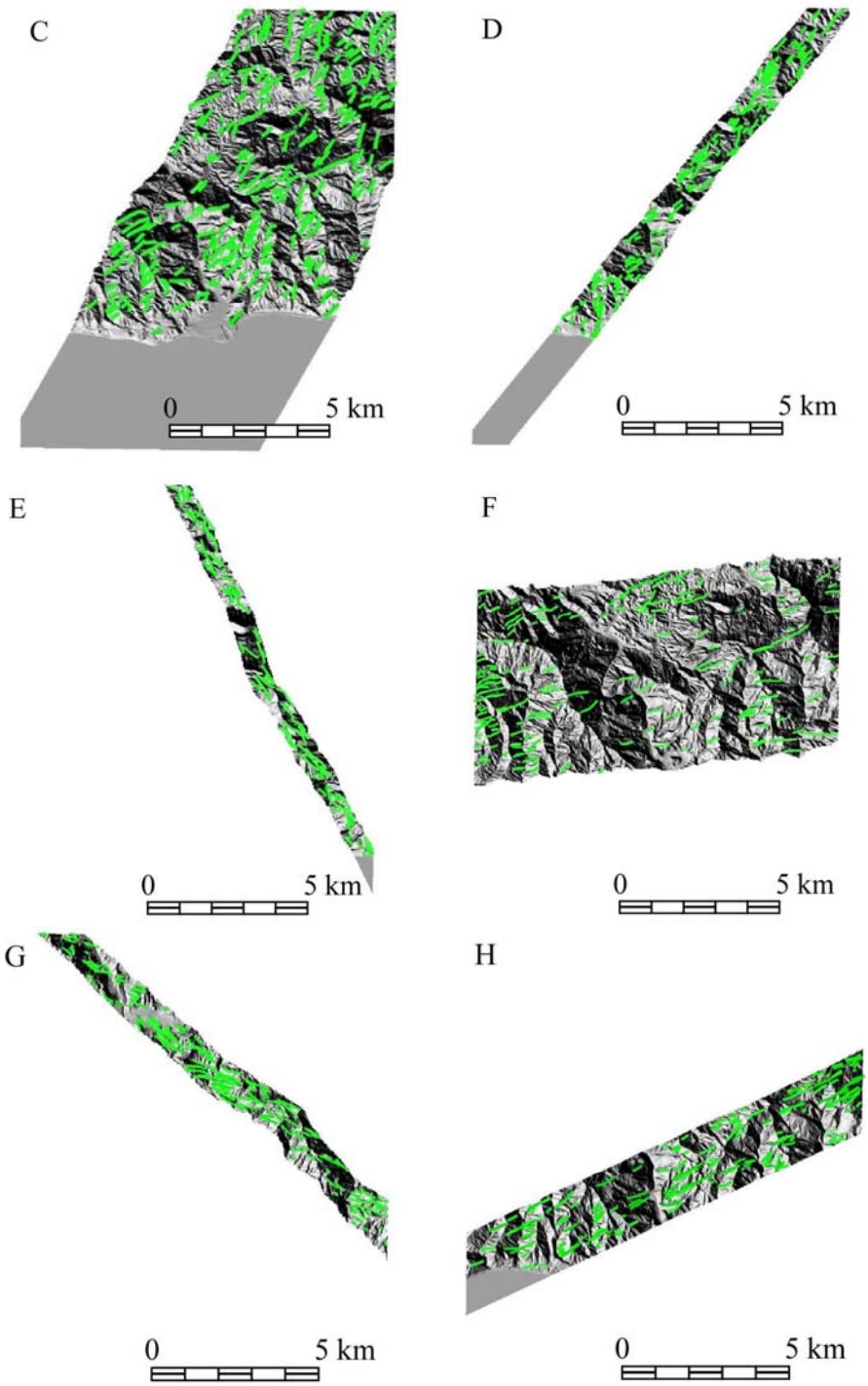

Figure 14, continued from previous page. This figure is continued onto the next page. (C) Seismo-lineament 20000316095007a illumined from 210°, 90° to strike. (D) 19810812225800a illumined from 219°, 90° to strike. (E) 19941026041847a illumined from 214°, 60° to strike. (F) 20000916132441a illumined from 235°, 60° to strike. (G) Seismo-lineament 19860520071140a with DEM illumined from 252°, -60° to strike. (H) 20030328054413a illumined from 245°, -90° to strike.

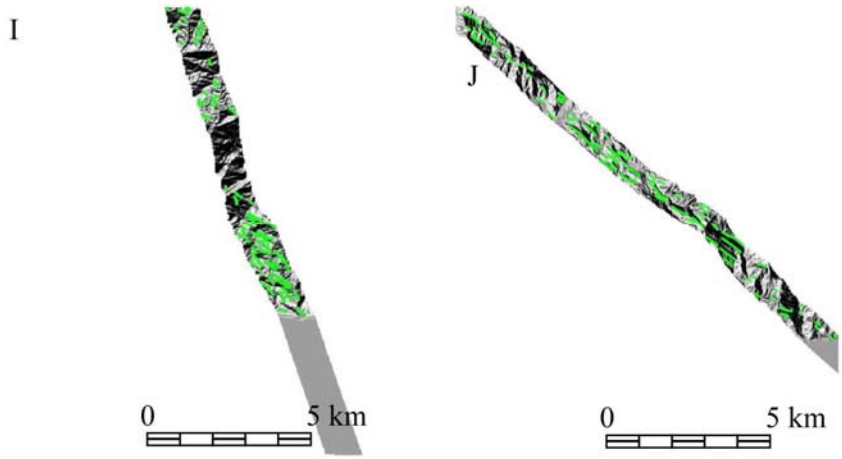

Figure 14, continued from previous page. (I) 19831123120100a illumined from 161°, 90° to strike. (J) 19930726212949a illumined from 251°, 30° to strike.

Some of these geomorphic lineament correlate with previously mapped faults or other lithologic boundaries, but many do not. There are a few outstanding trends on this composite lineament map, including geomorphic lineaments trending northwest-southeast, northeast-southwest, and east-west. The results of the geomorphic lineament analysis within each seismo-linearment swath are presented in Figure 15.

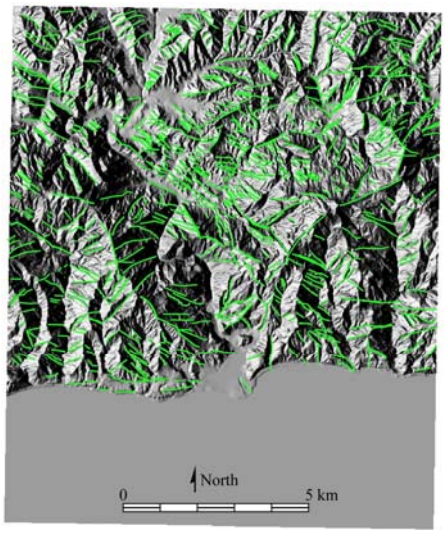

Figure 15. Geomorphic lineaments (green) mapped on an image of the DEM of the Malibu Beach 7.5 minute quadrangle, illumined from 270°.

Field Observations

The seismo-lineaments and the geomorphic lineaments within seismo-lineament swaths generated location hypotheses for possible seismogenic faults, which were evaluated during two field seasons in December, 2005, and May, 2006. Faults were identified within seismo-lineaments at 16 sites in the field (fig. 16). All of the faults were located on roadcut outcrops within the highland region of the Malibu Beach 7.5 minute quadrangle. Most had not been mapped previously.

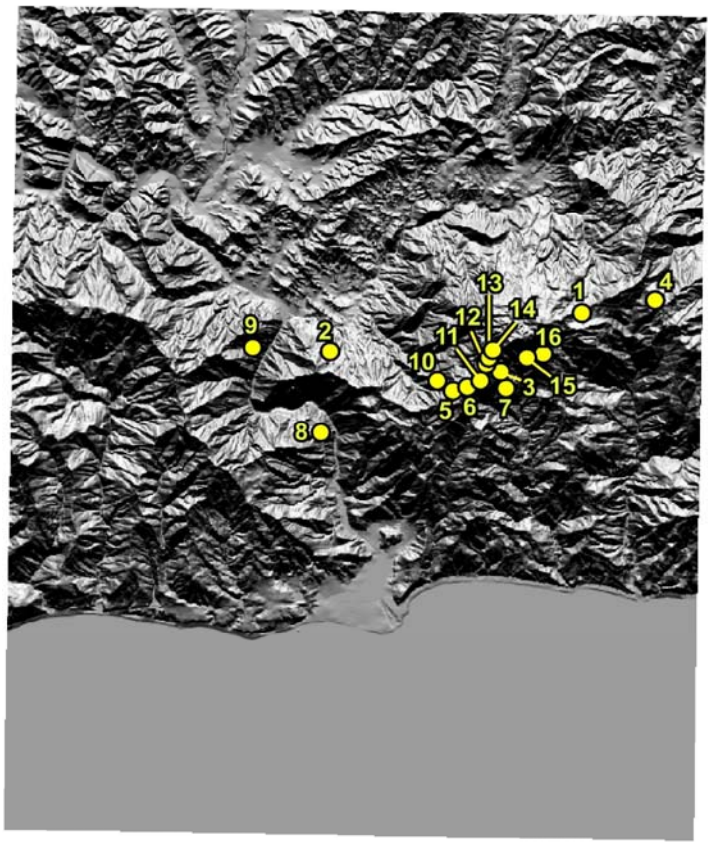

Figure 16. DEM of the Malibu Beach 7.5 minute quadrangle, showing the locations of sites where faults were located along seismo-lineaments.

All fault locations were recorded in the format of the topographic maps within the region: Universal Transverse Mercator (UTM) coordinates, zone 11, North America

datum of 1927 (NAD 27). None of the faults identified in the field appear to be involved in landsliding, and slip vectors were measured from shear striations on all faulted surfaces.

Site 1

Site 1 is located at UTM 11S 347997 E and 3772008 S with an uncertainty of 3 meters. The elevation is ~732 meters. The outcrop is located within the seismo-lineaments of the following earthquakes: 2003028054413a, 2000316095007a, and 20000916132441a. There are seven previously unmapped faults identified at this location.

Site 2

Site 2 is located at UTM 11S 344037 E and 3770978 N with an uncertainty of 8 meters. The elevation is ~282 meters. The outcrop is located within the seismo-lineaments of the following earthquakes: 20000916132441a, 19810812225800a, 2000316095007a, and 19940217161359a. There was no fault identified at this location, but a valley was observed that trends 170 degrees.

Site 3

Site 3 is located at UTM 11S 347534 E and 3770972 N with an uncertainty of 6 meters. The elevation is ~518 meters. The outcrop is located within the seismo-lineaments of the following earthquakes: 2003103010718a, 20030328054413a, 2000316095007a, 20000916132441a, 19941026041847a, and 198605200740a. Evidence of faulting was observed at three separate locations at the outcrop. This is a previously unmapped fault.

Site 4

Site 4 is located at UTM 11S 349286 E and 3772386 N with an uncertainty of 5 meters. The elevation is ~762 meters. The outcrop is located within the seismo-lineaments of the following earthquakes: 20030328054413a, 2000316095007a, 2003032805441a, 19941026041847a, and 198605200740a. This is a previously unmapped fault.

Site 5

Site 5 is located at UTM 11S 346580 E and 3770825 N with an uncertainty of 8 meters. The elevation was 640 meters. The outcrop is located within the seismo-lineaments of the following earthquakes: 20030328054413a, 2000316095007a, and 20000916132441a. This is a previously unmapped fault.

Site 6

Site 6 is located at UTM 11S 346742 E and 3770868 N with an uncertainty of 5 meters. The elevation is 640 meters. The outcrop is located within the seismo-lineaments of the following earthquakes: 20030328054413a, 2000316095007a, and 20000916132441a. This is a previously unmapped fault.

Site 7

Site 7 is associated with a shear zone that is ~50 meters wide. Even though there were several faults observed at this site, 11 previously unmapped faults were identified within this study (faults A, B, C, D, E, F, G, H, J, K, and L). The elevation of this site is 518 meters. The outcrop is located within the seismo-lineaments of the following

earthquakes: 20030328054413a, 2000316095007a, 20000916132441a, 19941026041847a, and 198605200740a.

All of the faults associated with site 7 cut Sespe Formation sandstone. Overall, the orientation of bedding was difficult to measure because the sandstone was heavily sheared.

Fault A is located at UTM 11S 347546 E and 3770746 N with an uncertainty of 4.26 meters (fig. 17).

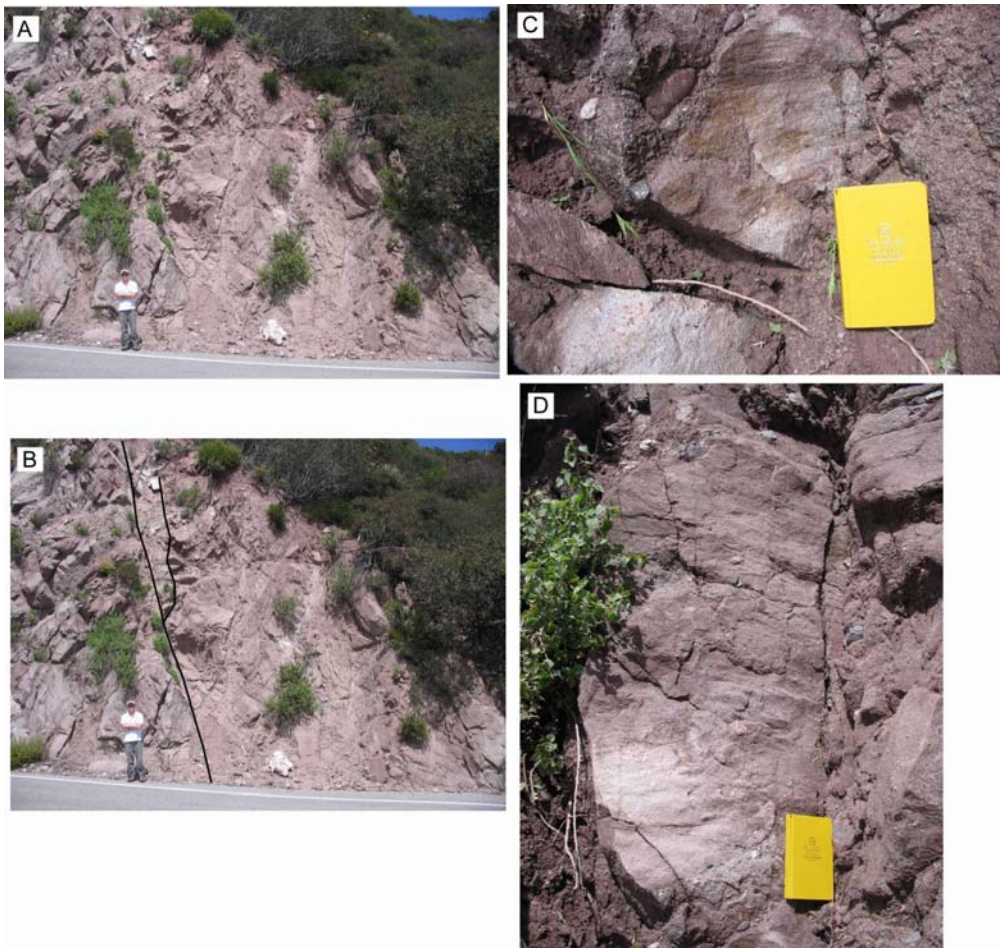

Figure 17. Fault 7A at site 7. (A) Uninterpreted field photograph of road cut. (B) Interpreted photograph, with fault zone outlined in black. (C) Shear striations on the fault surface. (D) Detail of the fault zone.

The lithology of both sides of Fault A is cohesive sandstone, which dips 32˚ to the northwest. The fault rock is composed of sheared purple sandstone, bounded by fairly regular surfaces. The average dip trend of the fault is 200˚; the average dip plunge is 74˚; with an associated 90% confidence interval of ±8˚. Polished surfaces containing shear striations were observed on the fault plane (fig. 17). The fault has a mean slip vector plunge of 24˚, a trend of 91˚, and an associated 90% confidence interval of ±9˚. There is an apparent offset of beds, but no offset of marker to measure.

Fault D is located at UTM 11S 347545 E and 3770744 N with an uncertainty of 7 meters (fig. 18).

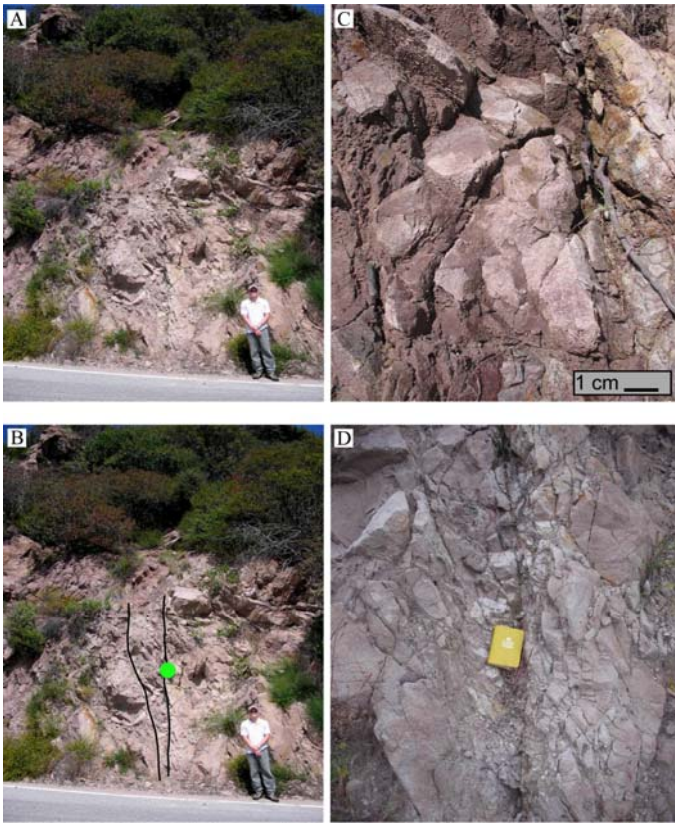

Figure 18. Fault 7D at site 7. (A) Uninterpreted field photograph of road cut. (B) Interpreted photograph with fault zone outlined in black and a green dot where shear striations were observed. (C) Shear striations on the fault surface. (D) Detail of fault the zone.

The lithology on both sides of Fault D is an indurated tan sandstone which dips 32° to the northwest. The fault rock is composed of brittle, fractured, and sheared zone of sandstone, bounded by fairly regular surfaces. The average dip trend of the fault is 224° (left side) and 248° (right side); and the average dip plunge is 61° (left side) and 64° (right side); with an associated 90% confidence interval of ±6° (left side) and 9° (right side). Polished surfaces containing shear striations were observed in the fault plane. The fault has a mean slip vector plunge of 19° (left side) and 22° (right side), a trend of 123° (left side) and 152° (right side), and an associated 90% confidence interval of ±9° (left side) and ±17° (right side). The width of the fault zone is 0.45 meters with an uncertainty of ±0.06 meters. There is apparent offset of beds, but no offset marker to measure at this fault.

Fault G is located at UTM 11S 347530 E and 3770836 N with an uncertainty of 14 meters (fig. 19). The lithology on both sides of the fault is cohesive sandstone which dips 32° to the northwest. The fault rock is composed of sheared gray sandstone, bounded by fairly regular surfaces. The fault rock truncates the surrounding sandstone beds. The average dip trend of the fault is 226° (left side) and 173° (right side); the average dip plunge is 47° (left side) and 67° (right side); with an associated 90% confidence interval of ±7° (left side) and ±11° (right side). Polished surfaces containing shear striations were observed in the fault plane. The fault has a mean slip vector plunge of 27° (left side) and 43° (right side), a trend of 109° (left side) and 64° (right side), and an associated 90% confidence interval of ±9° (left side) and ±22° (right side). The width of the fault is 1.61 meters with an uncertainty of 0.06 meters. There is apparent offset of beds, but no offset marker to measure at this fault.

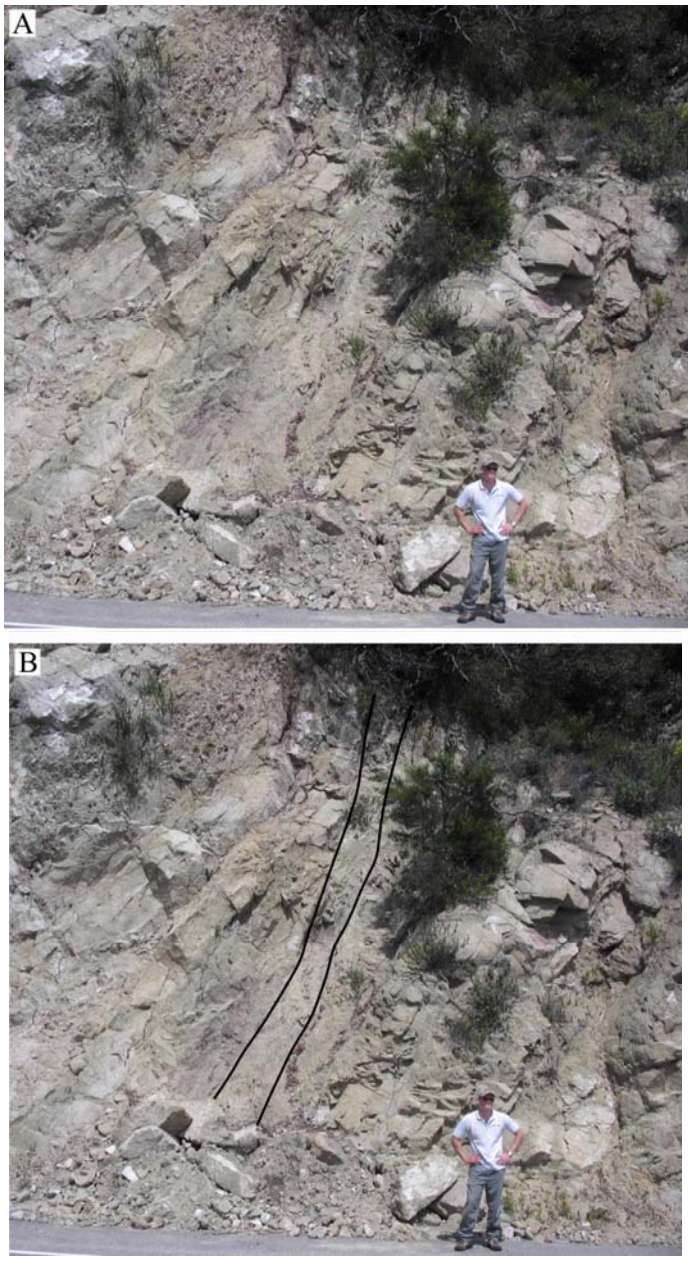

Figure 19. Fault 7G at site 7. (A) Uninterpreted field photograph of road cut. (B) Interpreted photograph, with fault zone outlined in black.

Fault H is located at UTM 11S 347517 E and 3770861 N with an uncertainty of 12.19 meters (fig. 20). The lithology on both sides of the fault is cohesive sandstone which dips 32° to the northwest. The fault rock is composed of sheared gray sandstone, bounded by fairly regular surfaces. The fault rock truncates the surrounding sandstone

beds. The average dip trend of the fault is 151°; the average dip plunge is 70°; with an associated 90% confidence interval of ±6°. Polished surfaces containing shear striations were observed in the fault plane (fig. 20). The fault has a mean slip vector plunge of 61°, a trend of 267°, and an associated 90% confidence interval of ±17°. The width of the fault is 1.37 meters with an uncertainty of 0.06 meters. There is apparent offset of beds, but no offset marker to measure at this fault.

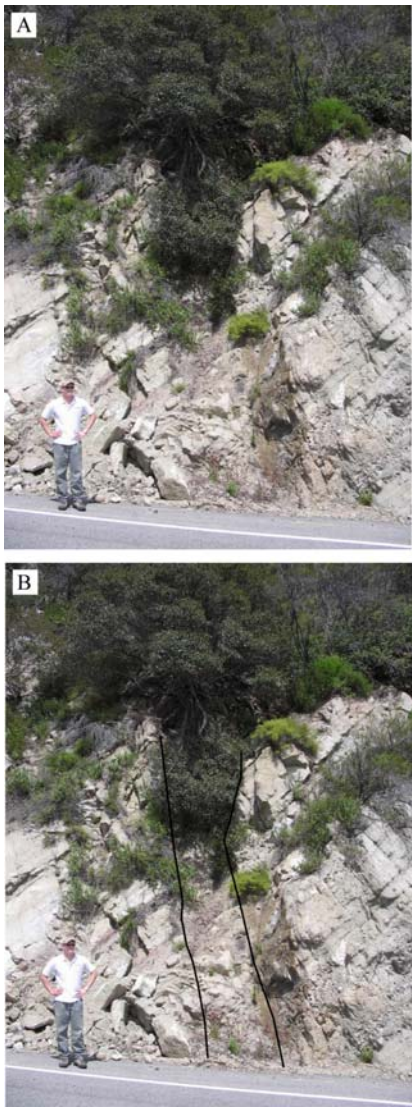

Figure 20. Fault 7H at site 7. (A) Uninterpreted field photograph of road cut. (B) Interpreted photograph, with fault zone outlined in black.

Fault J is located at UTM 11S 347513 E and 3770909 N with an uncertainty of 5.18 meters (fig. 21). The lithology on both sides of the fault is cohesive sandstone which dips 32˚ to the northwest. The fault rock is composed of sheared gray sandstone, bounded by fairly regular surfaces. The fault rock truncates the surrounding sandstone beds. The average dip trend of the fault is 206°; the average dip plunge is 52°; with an associated 90% confidence interval of ±2°. Polished surfaces containing shear striations were observed in the fault plane (fig. 21). The fault has a mean slip vector plunge of 39°, a trend of 77°, and an associated 90% confidence interval of ±5°. The width of the fault is 0.61 meters to 1.82 meters with an uncertainty of 0.06 meters. There is apparent offset of beds, but no offset marker to measure at this fault.

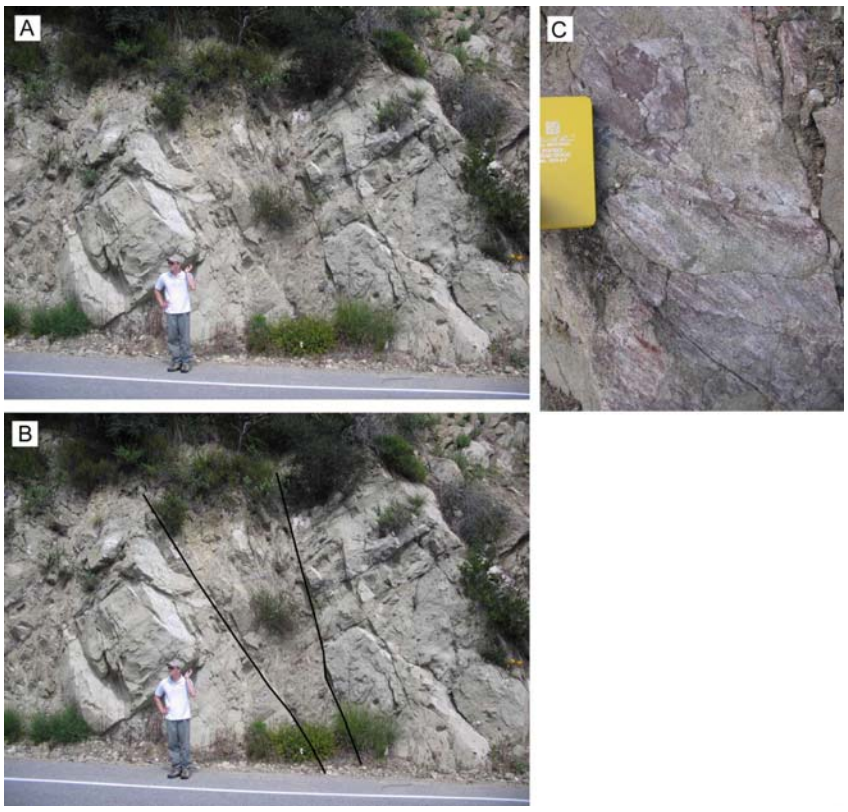

Figure 21. Fault 7J at site 7. (A) Uninterpreted field photograph of road cut. (B) Interpreted photograph, with fault zone outlined in black. (C) Shear striations on fault surface.

Fault K is located at UTM 11S 347511 E and 3770924 N with an uncertainty of 8 meters (fig. 22).

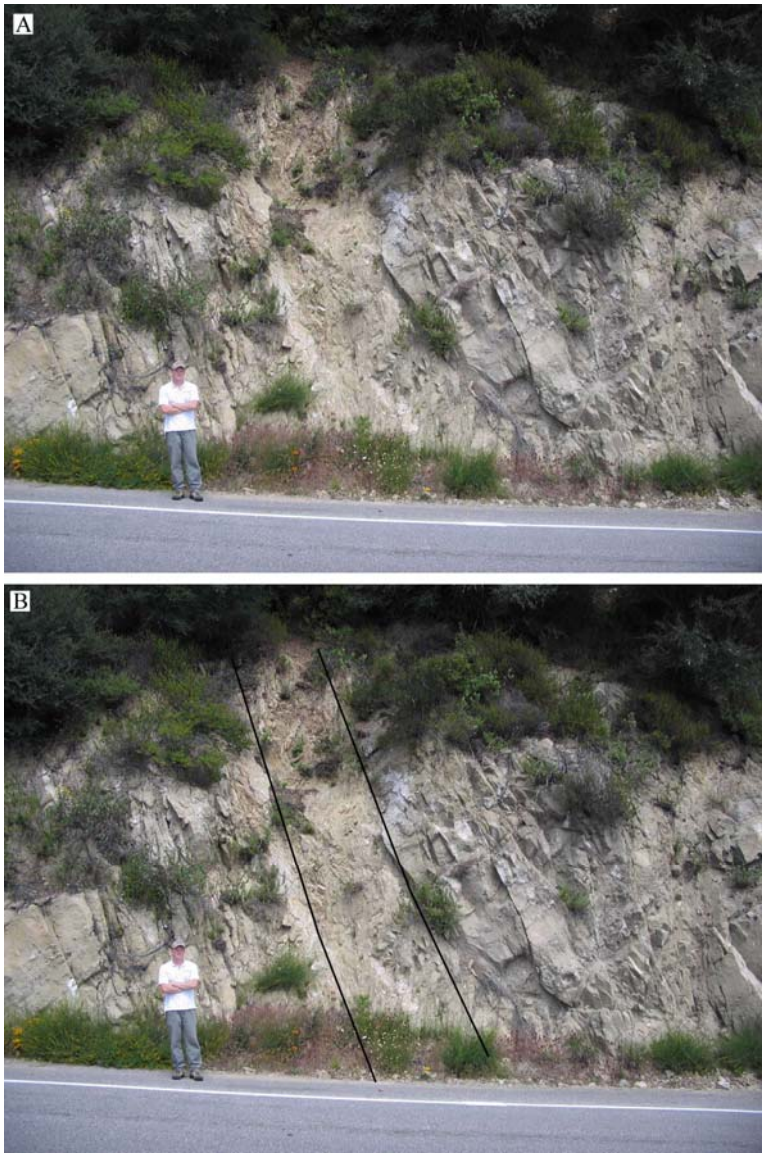

Figure 22. Fault 7K at site 7. (A) Uninterpreted field photograph of road cut. (B) Interpreted photograph, with fault zone outlined in black.

The lithology on either side of Fault K is cohesive gray sandstone which dips 32° to the northwest. The fault rock is non-cohesive fault gouge, bounded by fairly regular surfaces. The average dip trend of the fault is 214° (left side) and 219° (in the fault

zone); the average dip plunge is 61° (left side) and 50°. The gouge zone truncates the surrounding sandstone beds. Polished surfaces containing shear striations were observed in the fault plane (fig. 22). The fault has a mean slip-vector plunge of 26° degrees (left side) and 39° (in the plane of the fault), a trend of 109° (left side) and 87° (in the plane of the fault) degrees, and an associated 90% confidence interval of ±6° (left side) and 10° (in the plane of the fault). The width of the fault is 1.71 meters with an uncertainty of 0.06 meters. There is apparent offset of beds, but no offset marker to measure at this fault.

Site 8

Site 8 is located at UTM 11S 343728 E and 3769735 N with an uncertainty of 3 meters. The elevation is ~137 meters. The outcrop is located within the seismo-lineaments of the following earthquakes: 2003032805441, 20030328054413a, 19810812225800a, 2000316095007a, and 19940217161359a. This is a previously unmapped fault.

Site 9

Site 9 is located at UTM 11S 342860 E and 3771574 N with an uncertainty of 5 meters. The elevation is ~137 meters. There are two faults located at this site (fig. 23). Both outcrops are located within the seismo-lineaments of the following earthquakes: 2000316095007a, 20000916132441a, and 19940217161359a. The observed lithology on both sides of fault 2 is gray sandstone of the Topanga Canyon formation, which dips 56° to the northeast. The fault rock is composed of sheared gray sandstone. From south to north along the outcrop, there is massive sandstone that has shear striations in at least two

general directions, a faulted contact with horizontal shear striations in the fault plane (fig. 23), and near-vertical shale, pillow basalt, and massive sandstone is present at this outcrop. The average dip trend of the fault is 257° and the average dip plunge is 80°, with an associated confidence interval of ±1°. The fault has a mean slip vector plunge of 2°, an azimuth of 347°, and an associated 90% confidence interval of ±36°. Both faults are previously unmapped faults.

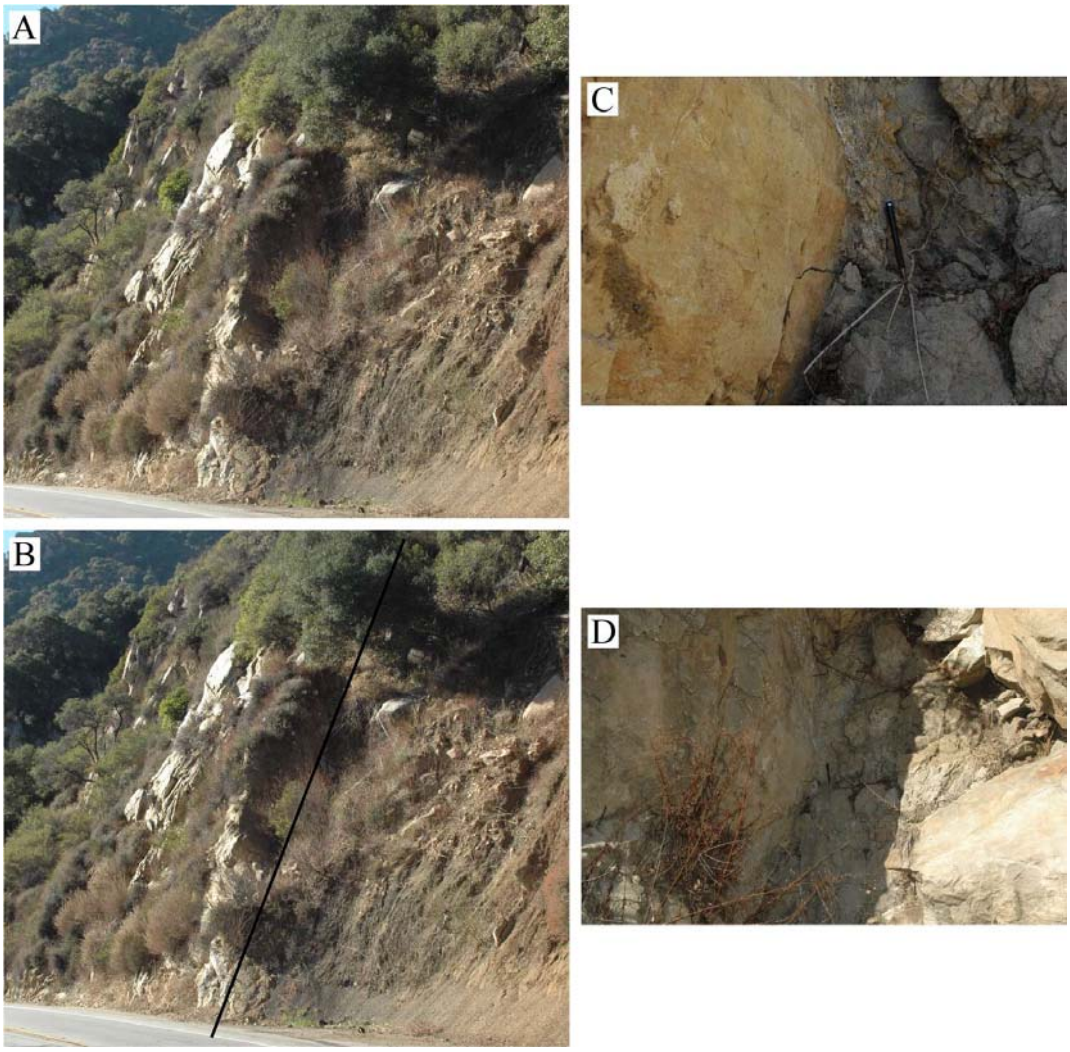

Figure 23. Fault 2 at site 9. (A) Uninterpreted field photograph of road cut. (B) Interpreted photograph, with fault zone outlined in black. (C) Shear striations on the fault surface, with pencil for scale. (D) Detail of the fault zone.

Site 10

Site 10 is located at UTM 11S 345648 E and 3770463 N with an uncertainty of 5 meters. The elevation is ~671 meters. The outcrop is located within the seismo-lineaments of the following earthquakes: 20030328054413a, 2000316095007a, 20000916132441a, 198311231020100a, and 19930726212949a. This is a previously unmapped fault.

Site 11

Site 11 is located at UTM 11S 346766 E and 3770933 N with an uncertainty of 5 meters. The elevation is ~640 meters. The outcrop is located within the seismo-lineaments of the following earthquakes: 20030328054413a, 20000916132441a, and 198605200740a. There are two faults observed located at this site. At fault 2 at site 11 (fig.24), the lithology on both sides surrounding the fault is grayish-red sandstone of the Piuma Formation, which dips 50° to the northwest. The fault rock is composed of sheared purple sandstone and mudstone in a zone that dips ~50° to the northwest. The average dip trend of the fault is 203° and the average dip plunge is 61°, with an associated 90% confidence interval of ±17°. Polished surfaces containing shear striations were observed in the fault plane. The fault has a mean slip vector plunge of 60°, a trend of 192°, and an associated 90% confidence interval of ±19°. The width of the fault is 1.06 meter with an uncertainty of 0.06 meter. The apparent offset of beds associated with the fault is 1.67 meter with an uncertainty of 0.06 meter. This is a previously unmapped fault.

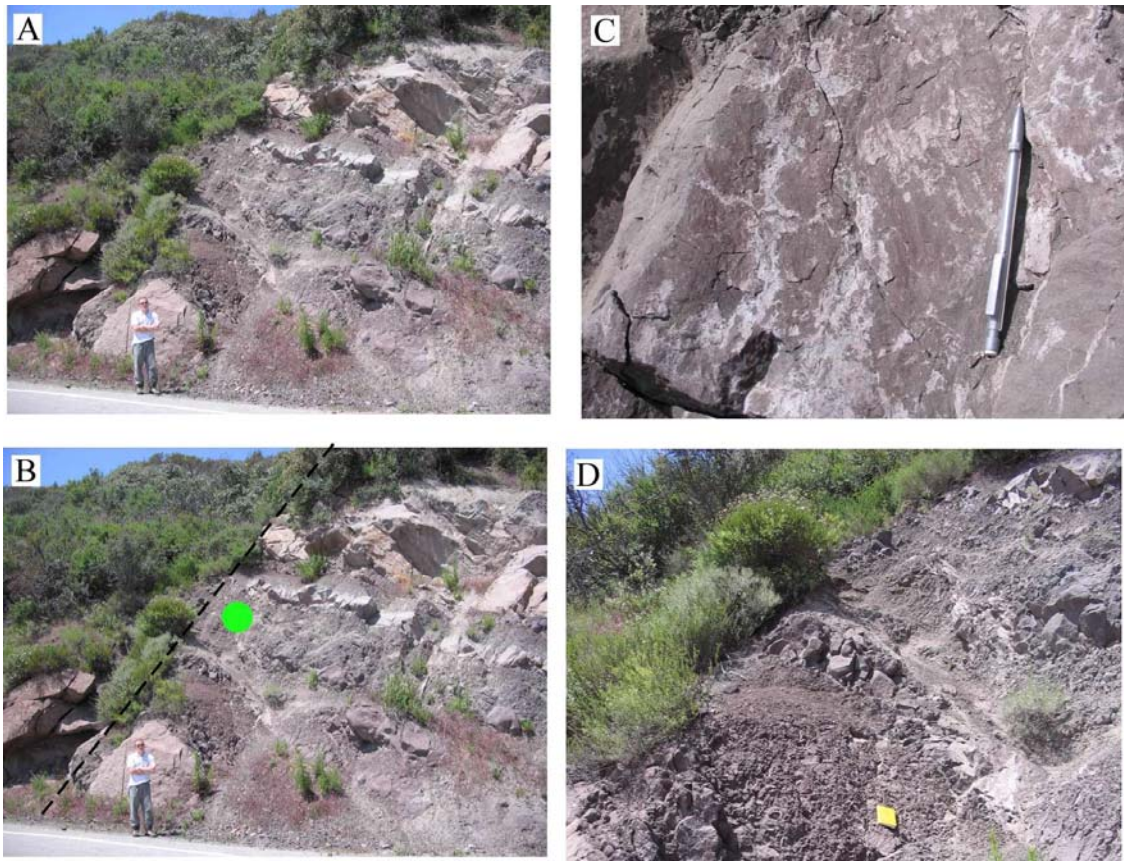

Figure 24. Fault 2 at site 11. (A) Uninterpreted field photograph of road cut. (B) Interpreted photograph, with fault zone outlined in black and the green dot shows the location where shear striations were observed. (C) Shear striations on the fault surface, with pencil for scale. (D) Detail of the fault zone.

Site 12

Site 12 is located at UTM 11S 346757 E and 3770957 N with an uncertainty of 2 meters. The elevation is ~640 meters. The outcrop is within the seismo-lineaments of the following earthquakes: 20030328054413a, 20000916132441a, and 198605200740a. This is a previously unmapped fault.

Site 13

Site 13 is located at UTM 11S 346757 E and 3770957 N with an uncertainty of 2 meters. The elevation is ~640 meters. The outcrop is within the seismo-lineaments of

the following earthquakes: 20030328054413a, 20000916132441a, and 198605200740a. This is a previously unmapped fault.

Site 14

Site 14 is located a few meters to the north of site 13, at UTM 11S 346757 E and 3770957 N with an uncertainty of 2 meters. The elevation is ~640 meters. The outcrop is within the seismo-lineaments of the following earthquakes: 20030328054413a, 20000916132441a, and 198605200740a. This is a previously unmapped fault.

Site 15

Site 15 is located at UTM 11S 347640 E and 3771496 N with an uncertainty of 4 meters. The elevation is ~625 meters. The outcrop is within the seismo-lineaments of the following earthquakes: 20030328054413a, 2000316095007a, 20000916132441a, 19941026041847a, and 198605200740a. This is a previously unmapped fault.

Site 16

Site 16 has UTM coordinates of 11S 347707 E and 3771501 N with an uncertainty of 8 meters. The elevation is ~625 meters. The outcrop is within the seismo-lineaments of the following earthquakes: 20030328054413a, 2000316095007a, 20000916132441a, 19941026041847a, and 198605200740a. There are two faults located at this location (figs. 25 and 26).

The lithology of the rocks on both sides of fault 1 at this site are tan igneous intrusive bodies, which are too small to be identified as their own unit (Yerkes and Campbell, 1980). The rocks at this site are intensely fractured. Overall, the orientation of bedding was difficult to measure because the sandstone was heavily sheared. Even so,

the sandstone beds generally dip ~30° to the northwest. Fault drag is present near the fault plane. The average dip trend of the fault is 216° and the average dip plunge is 70°, with an associated 90% confidence interval of ±8°. Polished surfaces containing shear striations were observed in the fault plane. The fault has a mean slip-vector plunge of 36°, an azimuth of 136°, and an associated 90% confidence interval of ±12°. This is a previously unmapped fault.

Figure 25. Fault 1 at site 16. (A) Uninterpreted field photograph of road cut. (B) Interpreted photograph, with fault zone outlined in black and a green dot where shear striations were observed. (C) Shear striations on the fault surface, with Brunton compass for scale.

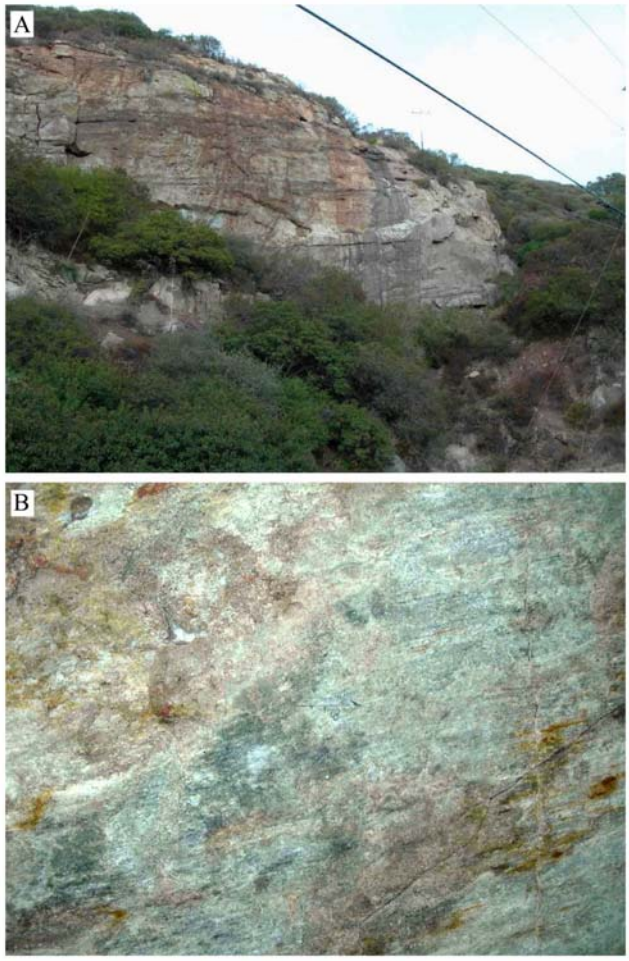

Figure 26. Fault 2 at site 16. (A) Uninterpreted field photograph of fault, which is along the prominent rock surface. (B) Shear striations on the fault surface.

Figure 26 presents the location of fault 2 at site 16. The outcrop in Figure 26 appears to be abruptly terminated to the east by a linear canyon. The lithology of the rock face is tan sandstone of the Sespe Formation. There are sheared surfaces in a number of different orientations at the east base of the outcrop. Faint horizontal striae were noted on a surface oriented 222 87, and striae raking roughly 90° on a surface oriented 175 68. Sheared surfaces were also observed on float rock below the face. The average dip trend of the fault is 23° and the average dip plunge is 88°, with an associated

90% confidence interval of ±41°. Polished surfaces containing shear striations were observed along the sandstone face. The fault has a mean slip-vector plunge of 39°, a trend of 293°, and an associated 90% confidence interval of ±6°. This is a previously unmapped fault.

After identifying several faults at sites 1 through 16, each fault was compared to the previously mapped faults within the Malibu Beach 7.5 minute quadrangle. Figure 27 presents all of the faults identified in the field (indicated by the yellow dots) and the previously mapped faults (indicated by the lines in red) within the study area. In general, the faults identified in the field do not correlate with the previously mapped faults and therefore they can be considered previously unmapped

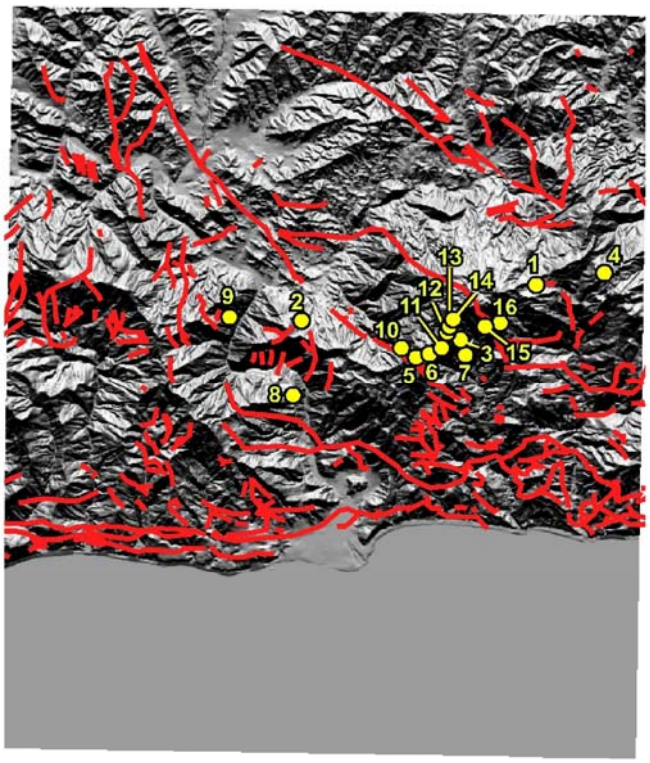

Figure 27. Image of DEM of the Malibu Beach 7.5 minute quadrangle, showing previously mapped faults in red and sites where faults were observed along seismo-lineaments as yellow dots.

CHAPTER FIVE

Discussion

Interpretation of Results

The purpose of this project was to identify seismogenic faults in the Malibu Beach 7.5 minute quadrangle. Current maps for the Santa Monica Mountains place all active faulting along a few left oblique structures along the coastline and just offshore. This study suggests that there is more structural activity occurring in the Santa Monica Mountains than current models allow, as the previously unmapped faults identified in the highland region do not correlate with the active Malibu Coast Fault Zone along the coast.

Cronin's (2004) seismo-lineament analysis method was successful in identifying several faults in the Malibu Beach 7.5 minute quadrangle, some of which had not been previously mapped. The possible relationship between each of these faults and the earthquake used to generate the corresponding seismo-lineament was evaluated based on the following criteria: (1) the surface trace of the fault must be located within the seismo-lineament swath; (2) the fault must have a similar orientation to the fault-plane solution associated with the seismo-lineament; and (3) the fault must have a slip vector with an orientation similar to the slip vector of the corresponding fault-plane solution. Some faults identified in the field correlated with seismo-lineaments, and some did not.

Seismo-Lineament 20030328054413a

Both fault H at site 11 and fault 2 at site 11 have orientations and slip characteristics similar to the fault-plane solution associated with seismo-lineament 20030328054413a (fig. 28).

Figure 28. Image of DEM along seismo-lineament 20030328054413a. The two dots indicate the locations of faults H site 7 (red) and fault 2 at site 11 (yellow).

Figures 29A and B present stereonet plots of the uncertainty regions around the fault planes and slip vectors associated with site 7 (fault H) and site 11 (fault 2). Figure 29A illustrates the overlap in the 90% confidence regions for the orientation of the fault-plane solution and the observed fault orientations, and figure 29B compares the

orientation of the slip vector computed from earthquake data and the orientations of shear striations on the fault surface.

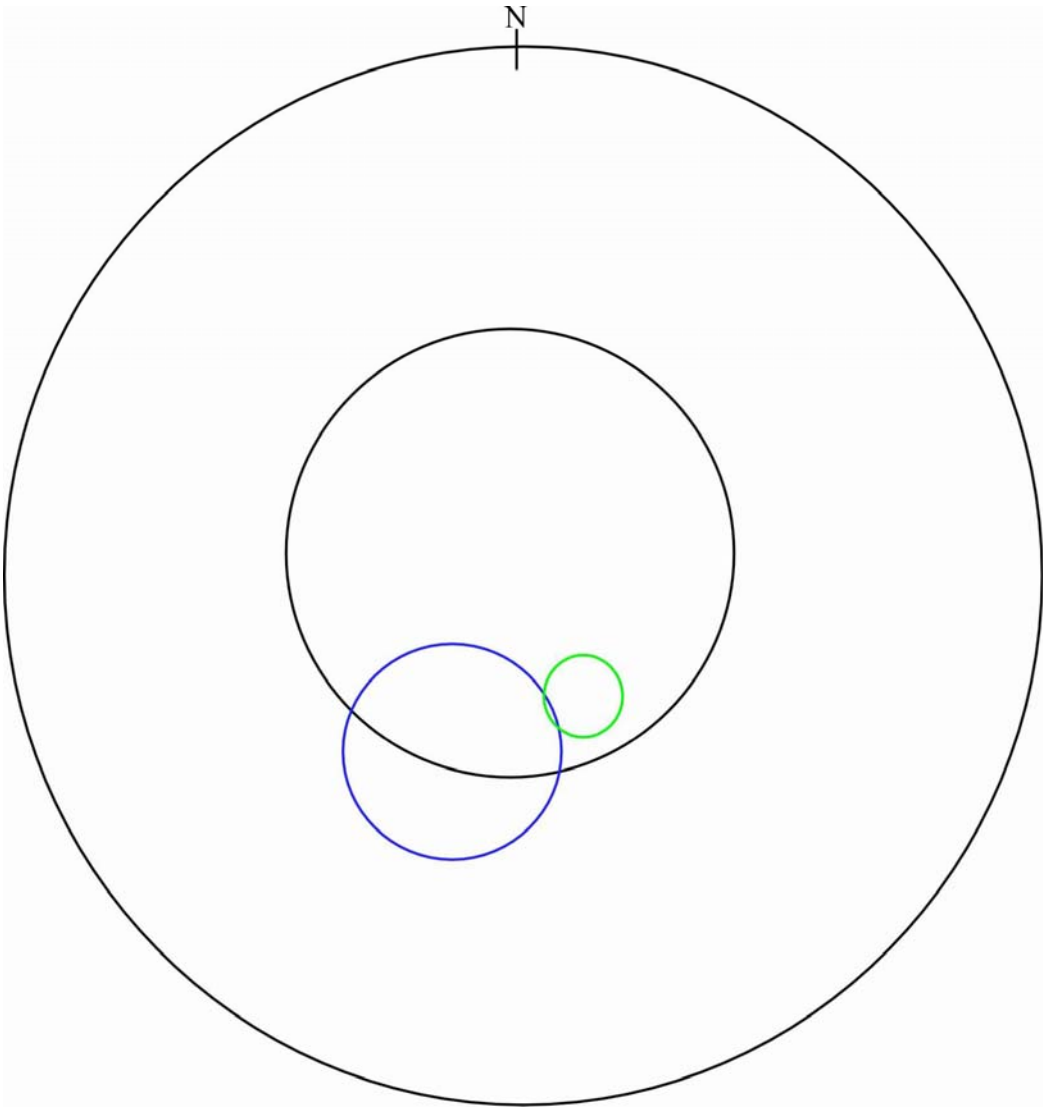

Figure 29A. Lambert equal-area lower hemisphere projection of the relationship between focal mechanism solution 20030328054413a and faults H at site 7, and fault 2 at site 11. The focal mechanism solution has a reported dip-vector plunge of 85° trending 335°, with a reported 90% confidence interval of 35° (black small circle), and a hanging-wall slip vector that rakes -40° with a reported 90% confidence interval of 25°. The other small circles represent the 90% confidence interval associated with the orientations of fault 2 at site 11 (blue), and fault H at site 7 (green).

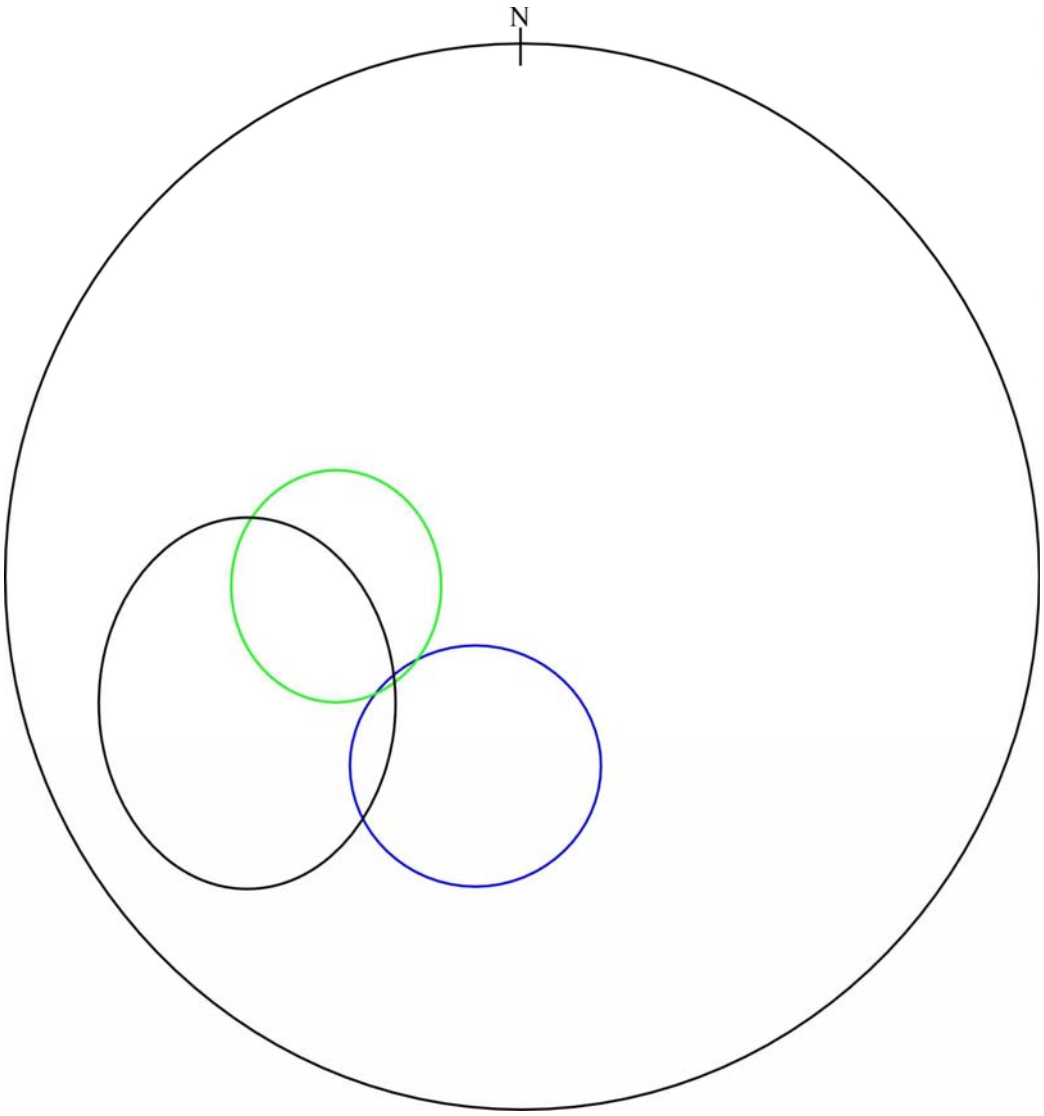

Figure 29B. Lambert equal-area lower hemisphere projection of the relationship between focal mechanism solution 20030328054413a and faults H at site 7, and fault 2 at site 11. The focal mechanism solution has a reported dip-vector plunge of 85° trending 335°, with a reported 90% confidence interval of 35°, and a hanging-wall slip vector that rakes -40° with a reported 90% confidence interval of 25° (black small circle). The other small circles represent the 90% confidence interval associated with the slip vectors on fault 2 at site 11 (blue), and on fault H at site 7 (green).

These faults are all located within the seismo-lineament swath (fig. 28). Therefore, these faults can be tentatively considered seismogenic and probably coincident with the fault that generated earthquake 20030228054413a.

Within seismo-lineament swath 20030328054413a, two faults were found to have the same orientations and slip characteristics as the corresponding fault-plane solution. It is possible that there may not be just one faulted surface, but several parallel seismogenic strands associated with this earthquake event. The three faults located at sites 11 and 12 (on the west side of the road) are also an example of parallel faults with the same general orientation (fig. 30).

Figure 30. Interpreted photographs of the three faults at sites 11 and 12.

There are several geomorphic lineaments within seismo-lineament 20030328054413a, including several strong northeast-to-southwest trending geomorphic lineaments (fig. 28). Northeast and southwest trends exist within the seismo-lineament swath on the geologic map by Yerkes and Campbell (1980).

Seismo-Lineament 20000916132441a

Faults A, D, G, J, and K at site 7 all have orientations and slip characteristics similar to the fault-plane solution associated with seismo-lineament 20000916132441a (fig. 31).

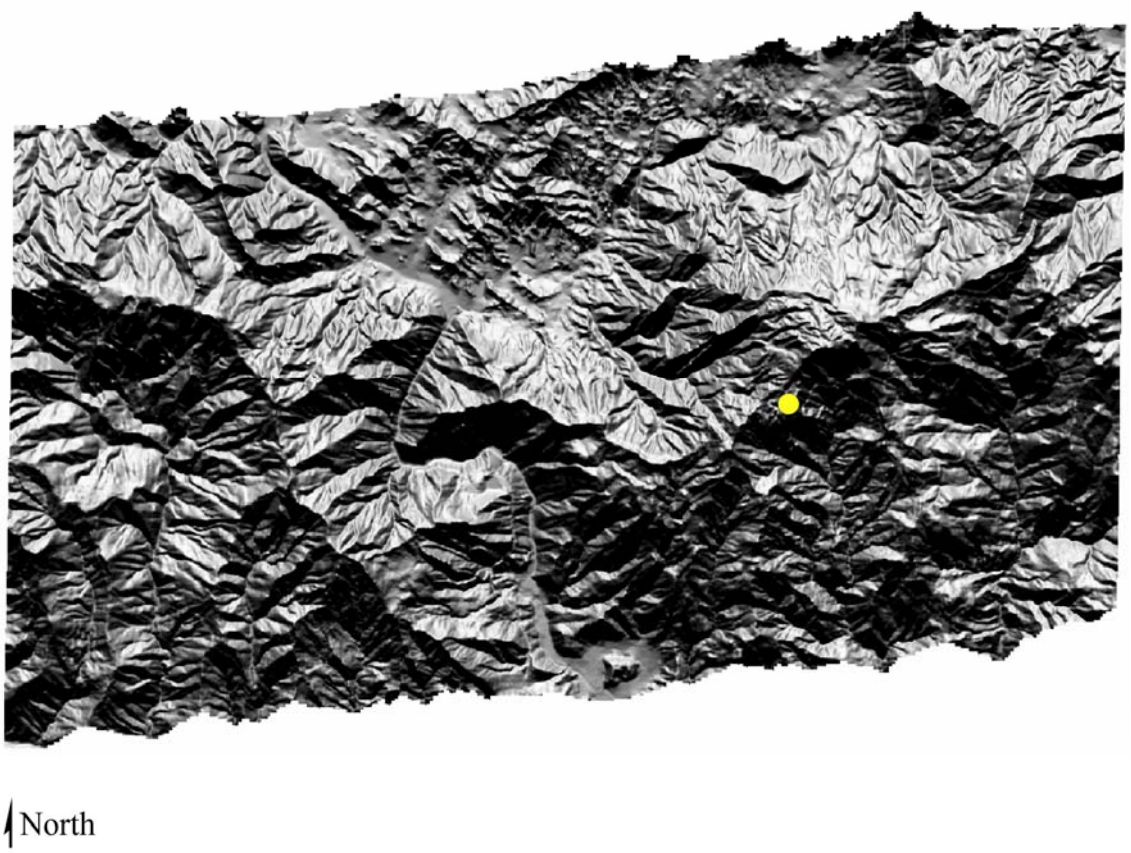

Figure 31. Image of DEM along seismo-lineament 20000916132441a. The yellow dot indicates the locations of faults A, D, G, J, and K at site 7.

Figures 32A and B present stereonet plots of the uncertainty regions around the fault planes and slip vectors associated with site 7 (fault A, D, G, J, and K). Figure 32A illustrates the overlap in the 90% confidence regions for the orientation of the fault-plane solution and the observed fault orientations, and figure 32B compares the orientation of the slip vector computed from earthquake data and the orientations of shear striations on the fault surface.

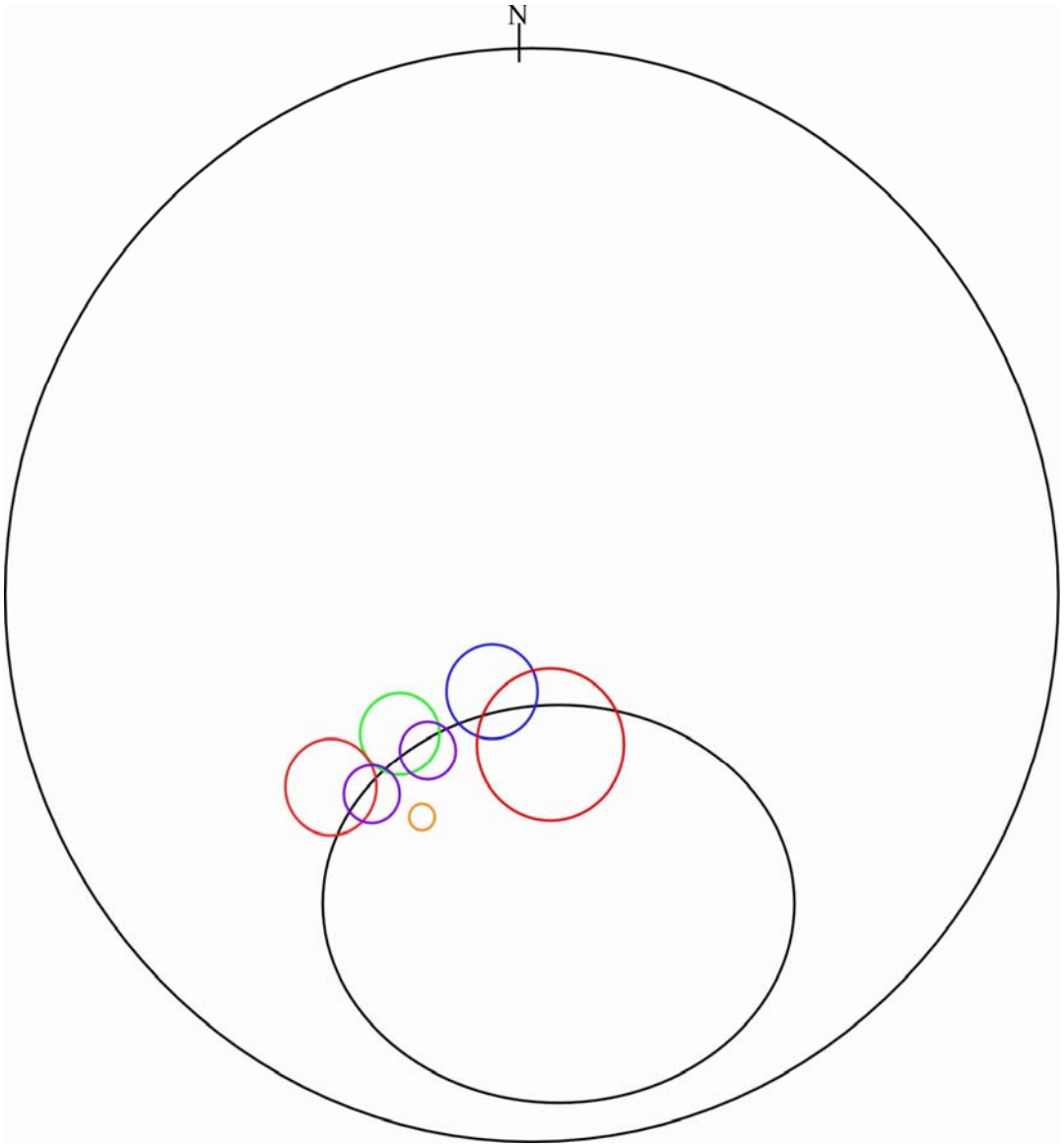

Figure 32A. Lambert equal-area lower hemisphere projection of the relationship between focal mechanism solution 20000916132441a and faults A, D, G, J, and K at site 7. The focal mechanism solution has a reported dip-vector plunge of 40° trending 175°, with a 90% confidence interval of 33° (black small circle), and a reported rake of 110° with a 90% confidence interval of 50°. The other small circles represent the 90% confidence interval associated with the orientations of fault A at site 7 (blue), fault D at site 7 (green), fault G at site 7 (red), fault J at site 7 (orange), and fault K at site 7 (purple).

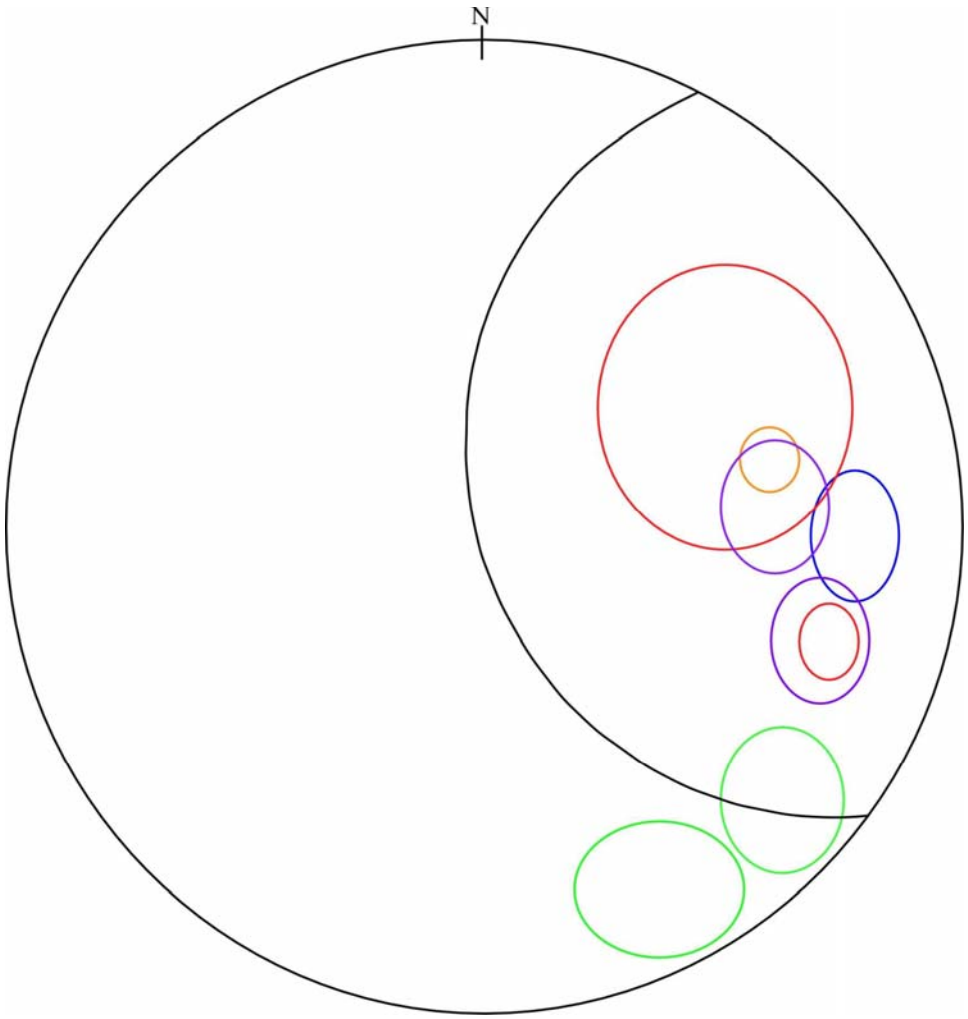

Figure 32B. Lambert equal-area lower hemisphere projection of the relationship between focal mechanism solution 20000916132441a and faults A, D, G, J, and K at site 7. The focal mechanism solution has a reported dip-vector plunge of 40° trending 175°, with a 90% confidence interval of 33°, and a reported rake of 110° with a 90% confidence interval of 50° (black small circle). The small circles represent the 90% confidence interval associated with the slip vectors on fault A at site 7 (blue), fault D at site 7 (green), fault G at site 7 (red), fault J at site 7 (orange), and fault K at site 7 (purple).

These faults are all located within the seismo-lineament swath (fig. 31). Therefore, these faults can be tentatively considered seismogenic and probably coincident with the fault that generated earthquake 20000916132441a.

Within seismo-lineament swath 20000916132441a, five faults were found to have the same orientations and slip characteristics as the corresponding fault-plane solution. It

is also possible at this location that there may not be just one faulted surface, but several parallel seismogenic strands associated with this earthquake event. There are several geomorphic lineaments within seismo-lineament 20000916132441a, including several strong northeast-to-southwest trending geomorphic lineaments (fig. 31). Northeast and southwest trends exist within the seismo-lineament swath on the geologic map by Yerkes and Campbell (1980).

Seismo-Lineament 200310310718a

Bayliss (2006) located three faulted outcrops with similar orientation and slip characteristics to one of the fault-plane solutions associated with earthquake 200310310718, which occurred on October 31, 2003, and had a magnitude of 2.94. These faults provide evidence of a left-lateral strike-slip motion in the middle of the Santa Monica Mountains (fig. 33).

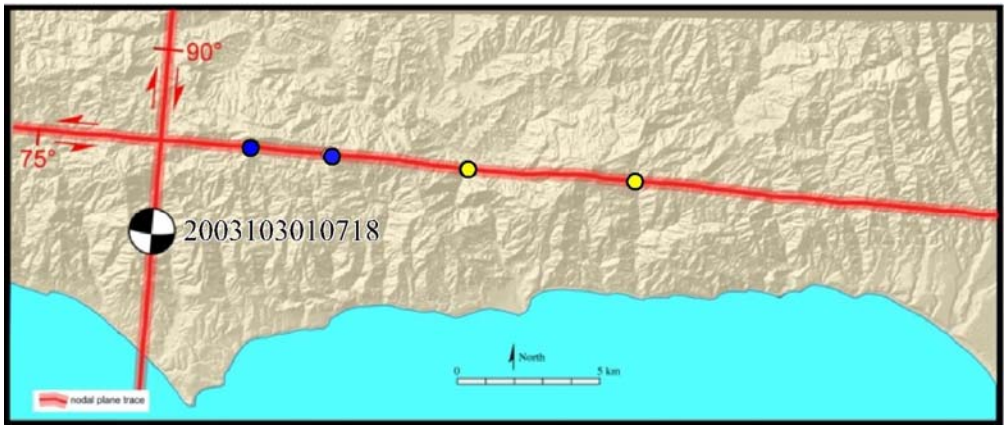

Figure 33. The focal mechanism solution (represented by the beach ball diagram) includes two fault plane solutions (red lines), which both have an orientation (indicated in degrees) and a sense of slip (red arrows). Seismo-lineament 200310310718a trends east-west. Along this east-west trending nodal plane trace, Bayliss (2006) located two faulted outcrops (blue dots) and this study has identified two faulted outcrops (yellow dots) with the right orientation and shear striations to indicate a left-lateral strike-slip motion feature through the middle of the Santa Monica Mountains.

This is interesting because this strike slip zone is not located along the coastal strip where current models place all active faulting in the Santa Monica Mountains (*e.g.*, Treiman, 1994).

The faults identified at site 16 (fault 1 and 2) are located within one of the seismo-lineament swaths associated with earthquake 200310310718a (fig. 34). The faults also have an orientation and slip characteristics that are similar to the fault-plane solution associated with seismo-lineament 200310310718a.

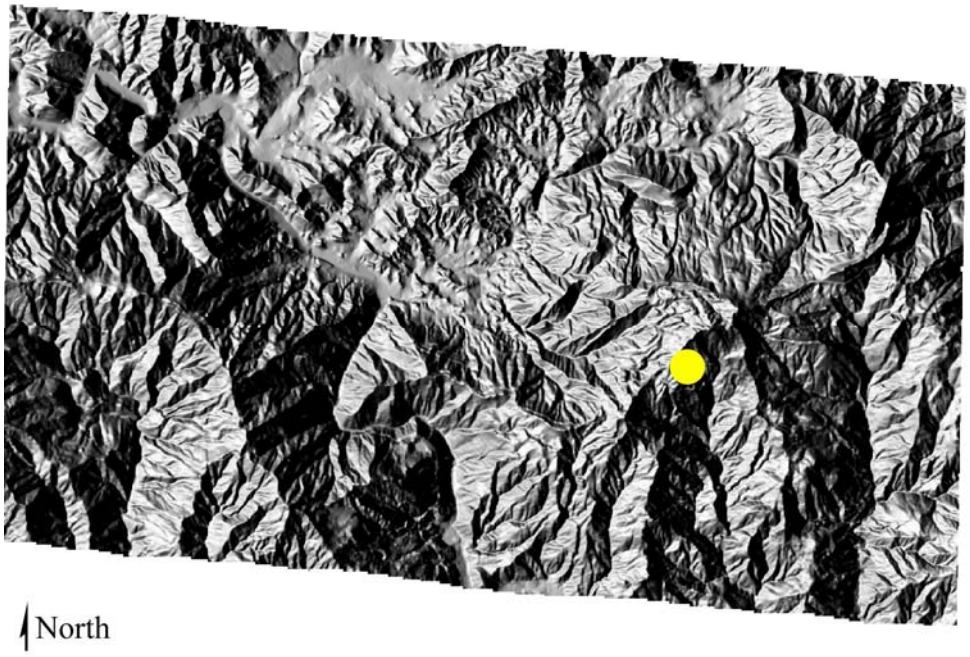

Figure 34. Image of DEM along seismo-lineament 2003103010718a. The yellow dot indicates the location of site 16.

Figures 35A and B present stereonet plots of poles to points for all orientations and slip vectors at site 16 and fault 2 at site 9. This fault can be tentatively considered seismogenic and probably coincident with the fault that generated earthquake 200310310718a.

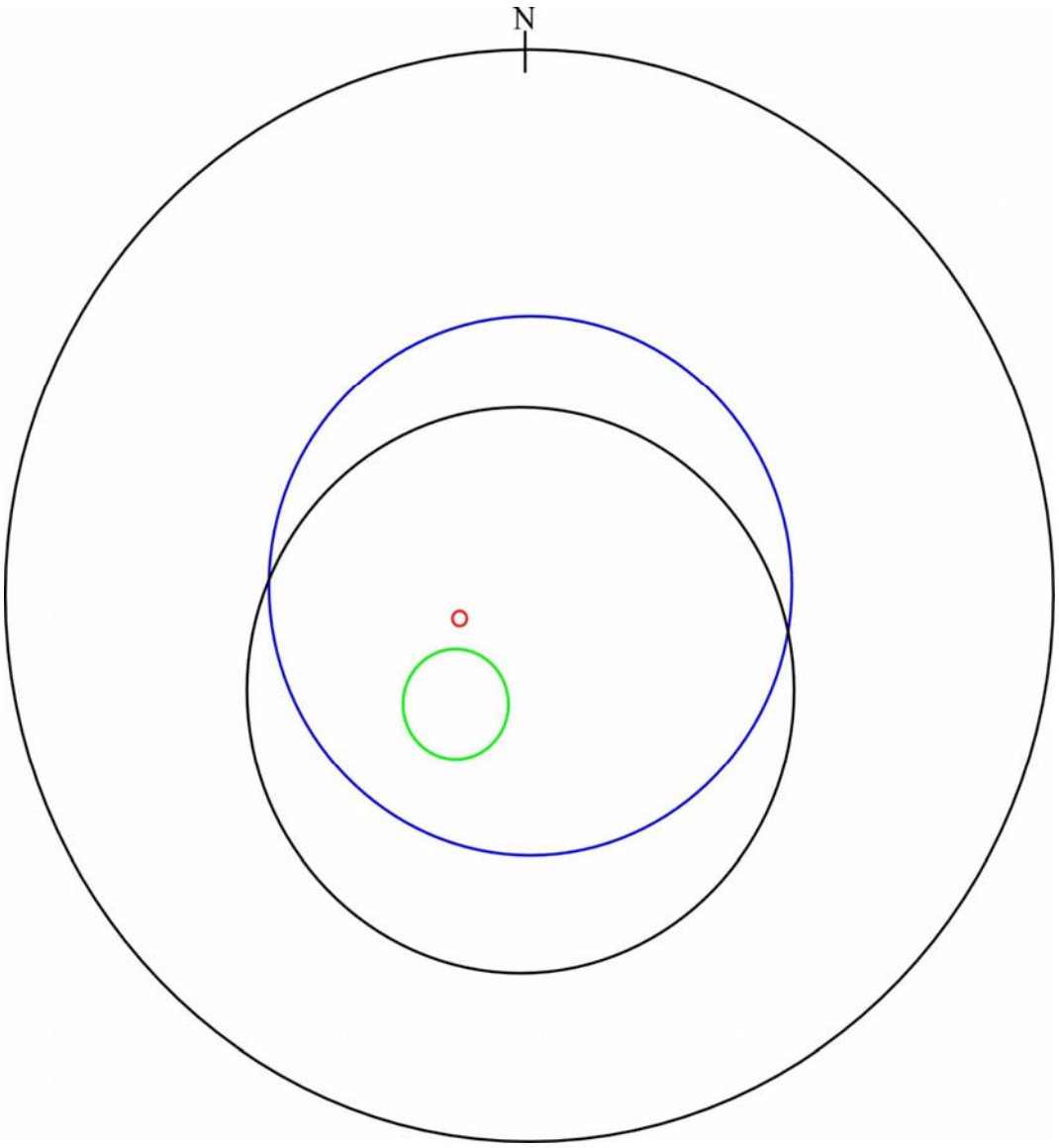

Figure 35A. Lambert equal-area lower hemisphere projection of the relationship between focal mechanism solution 2003103010718a and fault 2 at site 9, fault 1 at site 16, and fault 2 at site 16. The focal mechanism solution has a reported dip-vector plunge of 75° trending 185°, with a 90% confidence interval of 43° (black small circle), and a reported rake of 0° with a 90% confidence interval of 50°. The small circles represent the 90% confidence interval associated with the orientations of fault 1 at site 16 (blue), fault 2 at site 16 (green), and fault 2 at site 9 (red).

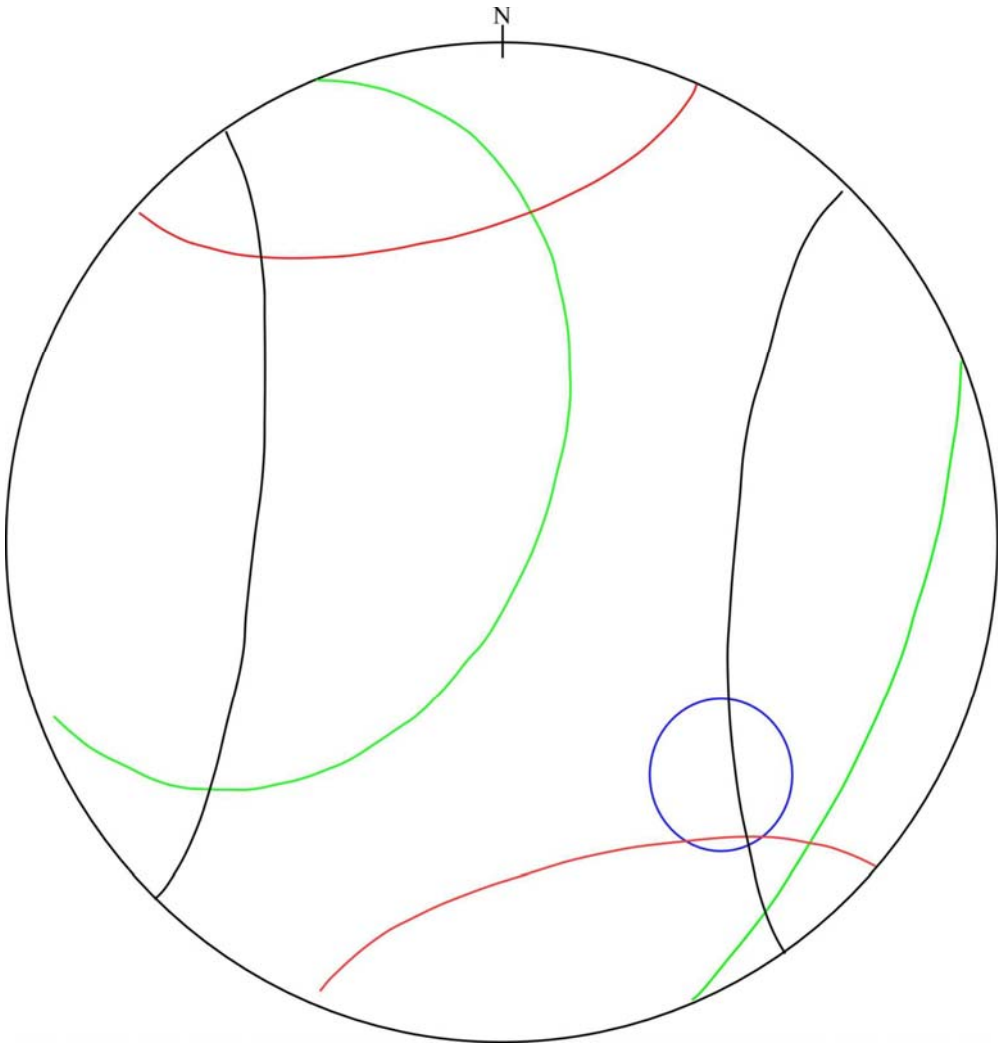

Figure 35B. Lambert equal-area lower hemisphere projection of the relationship between focal mechanism solution 2003103010718a and fault 2 at site 9, fault 1 at site 16, and fault 2 at site 16. The focal mechanism solution has a reported dip-vector plunge of 75° trending 185°, with a 90% confidence interval of 43°, and a reported rake of 0° with a 90% confidence interval of 50° (black small circle). The small circles represent the 90% confidence interval associated with the slip vectors on fault 1 at site 16 (blue), fault 2 at site 16 (green), and fault 2 at site 9 (red).

Given that Bayliss (2006) found evidence of faulting consistent with earthquake 200310310718a and both faults at site 16 possesses the same orientations and slip characteristics as this particular earthquake event (fig, 33), I infer that the fault at site 16

is part of a left-lateral strike-slip fault zone through the middle of the Santa Monica Mountains.

There are several geomorphic lineaments within seismo-lineament 200310310718a, including several strong northwest to southeast trending features. These may be related to lithologic controls. Northwest and southeast trends exist within the seismo-lineament swath on the geologic map by Yerkes and Campbell (1980).

In addition to site 16 and the two sites identified by Bayliss (2006), seismo-lineament 200310310718a passes directly through the location of fault 2 at site 9, as does an east-west geomorphic lineament. This fault is considered to be seismogenic according to our criteria. It is a high-angle fault with roughly horizontal shear striations, so it is a strike-slip fault. Most of the faulting at site 9 is in the shale, with some shear evident in the sandstone. It is possible that the shale at this location may be accommodating most of the strike-slip movement through cataclastic flow at this location.

The results of this study indicate that there are several previously unmapped seismogenic faults in the Santa Monica Mountains, illustrating the need for new models for active deformation in the western Transverse Ranges. Evidence for a left lateral strike-slip system located in the center of the Santa Monica Mountains (fig. 36) and dip-slip faults along the coastline suggest a structural style similar to that of the Santa Cruz Island fault zone.

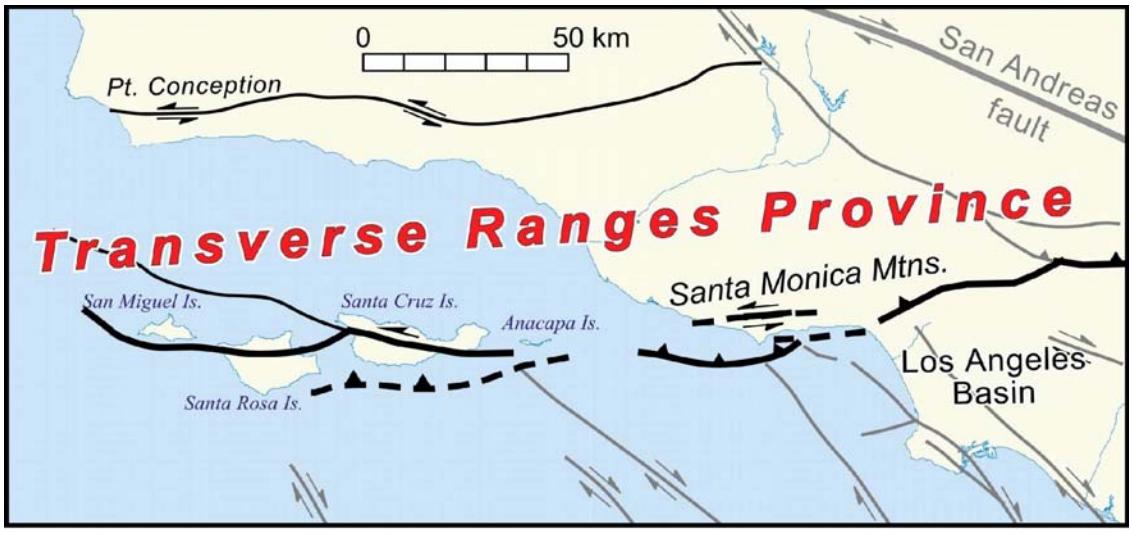

Figure 36. Relationship of the left-lateral strike-slip fault in the central Santa Monica Mountains to important faults around the western Transverse Ranges Province.

Pinter and others (1998) suggested that the Malibu Coast fault zone extends offshore toward the Santa Cruz Island fault zone. It is possible that this model presented by Legg and others (2004) is appropriate for the Santa Monica Mountains as well as the Santa Cruz Island fault zone (fig. 37).

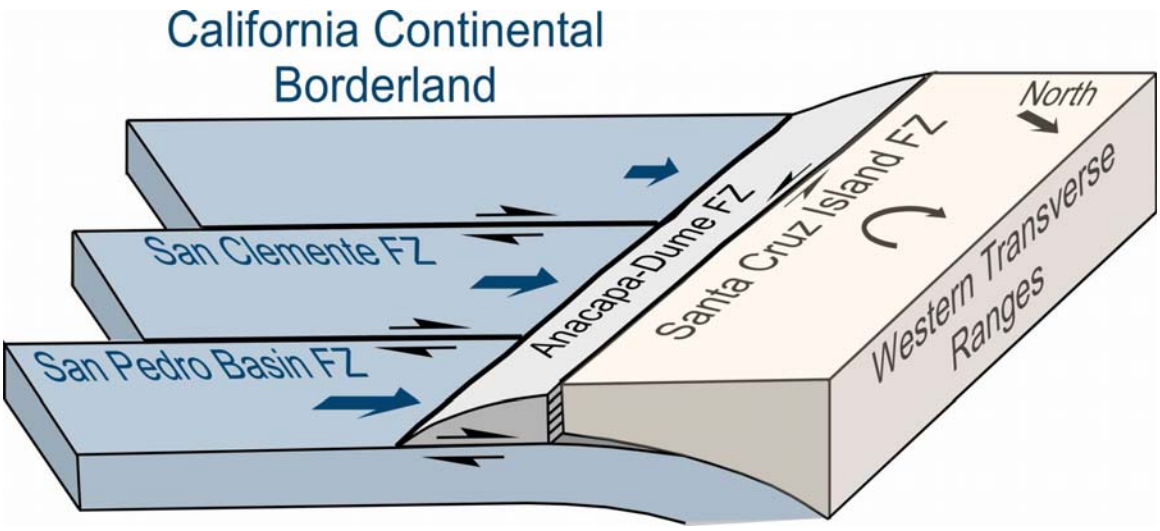

Figure 37. Kinematic model of strain partitioning along faults in the Channel Islands area, southern California, after Legg and others (2004).

In Legg's 2004 model, strain is partitioned between thrusting under the highland region and the strike slip fault with left lateral sense of slip. Strain partitioning provides the possibility for an array of faults in the Santa Monica Mountains that are mechanically optimized so the overall system does the least amount of work.

It is the combination of these interpretations that suggests the need for different ideas about active deformation in the western Transverse Ranges. The successful identification of Holocene-age faulting in the Santa Monica Mountains will have significant consequences for seismic risk analysis throughout the greater Los Angeles area.

Future Investigations

The faults recognized in the field that did not correlate with any of the earthquakes used in this study can be explained in several ways. They may correlate with seismo-lineaments from other historic earthquakes that were not evaluated in this study. They may correlate with Holocene earthquakes that predate accurate instrumental seismology, or for which no focal mechanism solution has yet been computed. Or they may now be "fossil" faults that are no longer seismogenic.

Future investigation will serve to expand upon the results presented in this study by applying the same set of analysis techniques in the Topanga 7.5 minute quadrangle and offshore. Also, since only the "a" planes to the focal mechanism solutions were investigated in this research project, it would be advantageous to field check the "b" planes in order to investigate the possibility of more seismogenic features in the study area. The "b" planes were not investigated because they projected out of the study area.

Aerial analysis with Landsat and SPOT satellite images, as well as several generations of geo-references aerial photos (orthoquadrangles) would also yield useful information in the search for potential seismogenic structures in the study area.

The results of this study indicate that there are probably seismogenic faults along seismo-lineaments 20030328054413a and 200310310718a. Additional field work is necessary within these seismo-lineament swaths to map the surface trace of these faults between the outcrops and roadcuts where they have been observed to date. This process may lead to the recognition of places along the fault trace where Holocene material may have accumulated, suggesting the possibility of a trench study. Trench studies are necessary to legally establish whether the faults are active, by the standards established by the State of California (Hart and Bryant, 1999). These types of discoveries could lead to geohazard mitigation efforts and more stringent zoning and building codes within the Santa Monica Mountains. Special attention should be paid to faults that cut pre-Holocene rock, like the faults identified in this study.

CHAPTER SIX

Conclusions

The integration of geomorphology and earthquake data yields useful information for the identification of previously unmapped seismogenic faults within the Malibu Beach 7.5 minute quadrangle. Several previously unmapped faults were successfully identified in the Malibu Beach 7.5 minute quadrangle using a combination of Cronin's (2004) geomorphic lineament and seismo-lineament analysis methods. Field work verified the existence of several previously unmapped faults along some seismo-lineaments. Some faults are approximately coplanar with earthquake fault-plane solutions, and are tentatively considered seismogenic.

The results of this study indicate that not all active faulting can be attributed to the Malibu Coast fault. There are more seismogenic faults than current, standard models allow in the Santa Monica Mountains. Focal mechanism solutions and field observations suggest that strain is partitioned between several seismogenic faults which may be working together to accommodate strain for the entire Santa Monica Mountain region. The methodology employed in this research is likely to be applicable to tectonically active areas around the world.

APPENDICES

APPENDIX A

The *Mathematica* Notebook Application, which Defines a Seismo-Lineament

Projecting a fault plane from a focal mechanism solution onto a digital elevation model surface

Written and revised by Vince Cronin for a research project of Vince Cronin, Brian Bayliss, Lauren Seidman, Mark Millard, Bruce Byars, and Lisa Zygo

Begun August 5, 2004; Revised September 6, 2006

Introduction

The purpose of this notebook is to describe how to define the intersection of a DEM surface and a plane of given orientation that passes through a particular point located below the DEM surface. The application of this is in estimating the surface trace of a fault plane defined by an earthquake focal mechanism solution. It is hoped that this technique, in conjunction with structural terrain analysis and field mapping, will assist in the identification of the surface traces of seismogenic faults.

Each fault surface is initially represented by an upward-directed unit vector that is normal to the fault plane and whose origin is at the earthquake focus. Each location vector to a point on the DEM surface grid is evaluated to determine whether it is within a user-defined region around 90° from the vector normal to the fault. If so, that grid location is identified as being along the surface trace of the fault plane, or within the uncertainty region around the fault plane. The result of evaluating every point on the DEM surface grid in this manner is a subset of points that collectively define the surface trace of the fault plane and the associated uncertainty region across the DEM surface.

The output from this application is a set of 3 files, whose names are defined by the user.

- One file is an encapsulated PostScript file (.eps) that contains the graphic showing the DEM shaded by elevation, the topographic contours at ~500 ft increments, curves marking the boundaries of the uncertainty region, and a curve showing the trace of the fault-plane solution intersection with the topography.
- Another file is a data file (.dat) with the same dimensions as the input DEM .dat file, but whose values are either the null value (-9999) or, for points located along the trace of the fault-plane solution intersection with the topography, some other value (typically "1" or the DEM-derived elevation at that node point).
- The other file is a data file (.dat) with the same dimensions as the input DEM .dat file, but whose values are either the null value (-9999) or, for points located along the boundaries of the uncertainty region, some other value (typically "1" or the DEM-derived elevation at that node point).

Explanation of changes to this code that are necessary to evaluate another fault plane solution

The list of changes noted below was created assuming that this code is going to be used to evaluate the DAT file "xport2" that is a digital elevation model (DEM) of part of the Malibu coastline in California. Malibu is in UTM Zone 11, whose central meridian is longitude -117 degrees. If those assumptions are not true, additional items will have to be adjusted.
(1) In the "Description of input data" section, the user must supply values for the following variables: focalLat, focalLong, reportedFocalDepthKm, faultDipTrend, faultDipPlunge, reportedVertError, horizError.
(2) In the "Import the DEM data from a DAT file" subsection of the "Digital elevation model (DEM)" section, the user may need to modify the path information so this notebook can find the input DEM/DAT file.
(3) In the "Export data and image files" section at the end of this code, the user must supply different names for the output files to avoid over-writing the results of previous runs.

Description of input data

■ Data source for focal mechanism solution used in this run

Egil Hauksson, http://www.data.scec.org/ftp/catalogs/hauksson/Socal_focal

■ From focal mechanism solution

Epicenter location: latitude (focalLat) and longitude (focalLong) in decimal degrees.

```
focalLat = 34.056;
```

```
focalLong = -118.821;
```

Focal depth (focalDepthKm) in kilometers

```
reportedFocalDepthKm = 11.8;
```

The central meridian of UTM Zone 11 is longitude -117°.

```
zoneMeridian = -117;
```

Trend (faultDipTrend) and plunge (faultDipPlunge) of dip vector of the fault plane, in decimal degrees

```
faultDipTrend = 185;
```

```
faultDipPlunge = 75;
```

Reported vertical (reportedVertError) and horizontal (horizError) uncertainties in the location of the earthquake focus, in kilometers.

```
reportedVertError = 28.1;

horizError = 0.2;
```

Some user-defined functions

```
makeVector[plunge_, trend_] := {Cos[plunge Degree] Sin[trend Degree],
   Cos[plunge Degree] Cos[trend Degree], -Sin[plunge Degree]};

vectorNorm[x_] := √x.x ;

unitVector[x_] :=
  {x[[1]] / vectorNorm[x], x[[2]] / vectorNorm[x], x[[3]] / vectorNorm[x]};

vectorAngle[a_, b_] := ArcCos[a.b / (vectorNorm[a] vectorNorm[b])];
```

The lat/long to UTM conversion is after Snyder, 1982.

```
convertToUTM[inLat_, inLong_, centMerid_] :=
  Module[{c1, c2, c3, c4, c5, v1, v2, v3, v4, v5, v6, utmX, utmY}, c1 = 6378206.4;
   c2 = 0.00676866; c3 = 0; c4 = centMerid; c5 = 0.9996; v1 = c2 / (1 - c2);
   v2 = c1 / Sqrt[1 - (c2 * (Sin[inLat Degree]^2))]; v3 = Tan[inLat Degree]^2;
   v4 = v1 * (Cos[inLat Degree]^2); v5 = (Cos[inLat Degree]) * ((inLong - c4) (π / 180));
   v6 = (111132.0894 * inLat) - (16216.94 * Sin[2 * (inLat Degree)]) +
     (17.21 * Sin[4 * (inLat Degree)]) - (0.02 * Sin[6 * (inLat Degree)]);
   utmX = (c5 * v2 * (v5 + (((1 - v3 + v4) * v5^3) / 6) +
          ((5 - (18 * v3) + (v3^2) + (72 * v4) - (58 * v1)) * v5^5) / 120)) + 500000;
   utmY = c5 * (v6 - 0 + (v2 * Tan[inLat Degree] * ((v5^2 / 2) +
            (((5 - v3 + (9 * v4) + (4 * (v4^2))) * v5^4) / 24) + (((61 - (58 * v3) +
                 (v3^2) + (600 * v4) - (330 * v1)) * v5^6) / 720)))); {utmX, utmY}];
```

The following module differentiates between points that are within "width" meters from the fault plane and those that are further away. Given unit vector N that is normal to the fault plane that passes through the origin of the coordinate system, the distance from an arbitrary point (whose position vector is P) to that plane is given by |N·P|.

```
pointEvaluator[xCoord_, yCoord_, zCoord_, width_, fltUNrml_, nulData_] :=
  Module[{locVect, distToFlt, result}, locVect = {xCoord, yCoord, zCoord};
   distToFlt = If[(zCoord < (-1000)), width, Abs[Dot[fltUNrml, locVect]]];
   result = If[(distToFlt ≤ width), zCoord, nulData]; result];
```

Defining the vertical extent of the uncertainty region around the earthquake focus

Defining the vertical extent of the uncertainty region around the earthquake focus is not always a simple matter of modifying the reported focal depth by the reported vertical error above and below the focus. In some cases, the combination of focal depth and stated vertical error yields locations that are above ground level, or below the reasonably expected depth of an earthquake focus in the area. The deepest reported earthquake in the west or central Santa Monica Mountains was a M2.9 event on February 1, 1994, located at longitude -119.17 and latitude 34.15, with a focal depth of 23 km (NEIC). The shallowest reported focal depths are less than 1 km. The highest elevation in the Santa Monica Mountains is Castro Peak, at 2,824 feet (861 meters).
The variable "upperBound" marks either the upper boundary of the crustal seismogenic zone (set at sea level) or the upper part of the uncertainty region for the earthquake focus, whichever is deeper.

```
upperBound = If[(reportedFocalDepthKm - reportedVertError) < 0,
   0., (reportedFocalDepthKm - reportedVertError)];
```

The variable "lowerBound" marks either the lower boundary of the crustal seismogenic zone (set at 23 km for the Malibu study) or the lower part of the uncertainty region for the earthquake focus,whichever is shallower.

```
lowerBound = If[(reportedFocalDepthKm + reportedVertError) > 23,
   23., (reportedFocalDepthKm + reportedVertError)];
```

The variable "meanFocalDepthKm" is the depth half way between the upper bound and the lower bound.

```
meanFocalDepthKm = upperBound + ((lowerBound - upperBound) / 2);
```

In situations where the reported error bars cause us to consider the possibility of an earthquake focus that is in the atmosphere or below the regional norm for the base of the seismogenic zone, we use a "pseudofocus" located between the upper and lower boundaries of the seismogenic zone for the purpose of mapping the uncertainty swath across the DEM.

```
focalDepthKm = If[meanFocalDepthKm ≠ reportedFocalDepthKm,
   meanFocalDepthKm, reportedFocalDepthKm];
```

The "vertError" is half the vertical uncertainty in focus location, expressed in meters. In situations where a "pseudofocus" is used, the vertical error will differ from the reported vertical error, allowing us to map a more reasonable uncertainty swath across the DEM.

```
vertError = If[focalDepthKm ≠ reportedFocalDepthKm,
   (meanFocalDepthKm * 1000), (reportedVertError * 1000)];
```

Find the unit vector normal to the fault surface at the earthquake focus

Convert the fault dip vector from trend and plunge to a unit location vector (dipUnitVector)

```
faultDipUnitVector = unitVector[makeVector[faultDipPlunge, faultDipTrend]];
```

Find the dip azimuth vector (dipAzimuthVector)

```
dipAzimuthVector = {Sin[faultDipTrend Degree], Cos[faultDipTrend Degree], 0};
```

Find the strike vector (strikeVector) defined using the right-hand rule

```
faultStrikeTrend = faultDipTrend - 90;

strikeVector = {Sin[faultStrikeTrend Degree], Cos[faultStrikeTrend Degree], 0};
```

Find the unit vector that is normal to the fault plane and is directed upwards (faultUnitNormal)

```
faultUnitNormal = unitVector[faultDipUnitVector × strikeVector];
```

Digital elevation model (DEM)

The digital elevation model is presented as a set of z data in meters, with x and y coordinates explicit from the position of the z datum in the data file. The data file is derived from the U.S. Geological Survey's DEM data for the Pt. Dume, Malibu Beach and Topanga 7.5 minute quadrangles (30 m resolution).
The DEM was acquired from _____

■ Import the DEM data from a DAT file

It is assumed that the DEM data is in a file called "xport.2" that is on the desktop,
with the path "C:\\Documents and Settings\\Vince_Cronin\\Desktop\\LaurenSeidmanCode\\xport2.dat"
This information should be adjusted as appropriate when this code is used by other people on other machines.

```
mydata = Import["C:\\Documents and Settings
     \\Vince_Cronin\\Desktop\\LaurenSeidmanCode\\xport2.dat"];
```

■ Read and interpret the DEM header information

Read the header information.

```
headerData = Table[mydata[[i, j]], {i, 6}, {j, 2}];
```

"ncols" is the number of columns; label in position [[1,1]] and value in [[1,2]]

```
ncols = headerData[[1, 2]];
```

"nrows" is the number of rows; label in position [[2,1]] and value in [[2,2]]

```
nrows = headerData[[2, 2]];
```

"xllcorner" is the UTM zone 11 "x" coordinate, in meters, of the lower left corner of the DEM; label in position [[3,1]] and value in [[3,2]].

```
xllcorner = headerData[[3, 2]];
```

"yllcorner" is the UTM zone 11 "y" coordinate, in meters, of the lower left corner of the DEM; label in position [[4,1]] and value in [[4,2]]

```
yllcorner = headerData[[4, 2]];
```

"gridSpacing" a.k.a. "cellsize" is the distance between grid nodes in the DEM file, in meters; label in position [[5,1]] and value in [[5,2]]

Note that the code below uses the variable name "gridSpacing" rather than "cellsize."

```
gridSpacing = headerData[[5, 2]];
```

"nodata_value" is the value used in the data file to indicate that there is no data in a specific location in the data file; label in position [[6,1]] and value in [[6,2]]

```
nodataValue = headerData[[6, 2]];
```

The seventh row of the data set is the first data row.

The true UTM coordinates of the datum in position [[i,j]] of the data set (from row 7 to the end) are as follows:

x coordinate = xllcorner + (cellsize * (j - 1)) y coordinate = yllcorner + (cellsize * (nrows - i))

z coordinate = the datum in position [[i,j]]

Convert the input coordinates of the earthquake focus to the same coordinate system as the DEM data

```
utmCoordinates = convertToUTM[focalLat, focalLong, zoneMeridian];
```

The "focus" is the (x, y, z) coordinates in meters of the "pseudofocus" located at a depth half way between the upper and lower boundaries of the vertical uncertainty region, in a coordinate system in which the origin is the lower-left (southwest) corner of the DEM at sea level.

```
focus = {(utmCoordinates[[1]] - xllcorner),
   (utmCoordinates[[2]] - yllcorner), (focalDepthKm * (-1000))};
```

The "reptFocus" is the (x, y, z) coordinates in meters of the reported earthquake focus, in a coordinate system in which the origin is the lower-left (southwest) corner of the DEM at sea level.

```
reptFocus = {(utmCoordinates[[1]] - xllcorner),
   (utmCoordinates[[2]] - yllcorner), (reportedFocalDepthKm * (-1000))};
```

Define the threshold for resolving whether a point in the DEM is within the fault swath

The "zoneHalfWidth" is twice the distance between the parallel planes that bound the uncertainty region for this fault-plane solution. The units are meters.

```
zoneHalfWidth = (vertError * Cos[faultDipPlungeDegree]) +
    (horizError * 1000 * Sin[faultDipPlungeDegree]);
```

The "innerZone" is the minimal width of the surface trace of the fault-plane solution, needed to define the trace given the input grid spacing. The units are meters.

```
innerZone = ((0.6 * gridSpacing) * Sin[faultDipPlungeDegree]);
```

■ Determine which points on the DEM lie along the modeled fault-plane trace, ± the width of the "innerZone," and map their boundary with points that do not lie along the fault-plane trace

The UTM coordinates of each point from the DEM are transformed to a coordinate system whose origin is at the earthquake focus
(focus = {(utmCoordinates[[1]]-xllcorner),(utmCoordinates[[2]]- yllcorner),(focalDepthKm*(-1000))}).

x coordinate=(gridSpacing*(j-1))-focus[[1]] y coordinate=(gridSpacing*(nrows-i))-focus[[2]]
z coordinate=(the datum in position [[i,j]])-focus[[3]]

```
inFaultTrace = Table[pointEvaluator[((gridSpacing * (j - 1)) - reptFocus[[1]]),
    ((gridSpacing * (nrows - i)) - reptFocus[[2]]),
    (mydata[[i + 6, j]] - reptFocus[[3]]), innerZone,
    faultUnitNormal, nodataValue], {i, nrows}, {j, ncols}];

elev1 = Table[inFaultTrace[[i, j]], {i, nrows, 1, -1}, {j, ncols}];

traceImageFile1 = ListContourPlot[elev1,
  ContourShading → False, AspectRatio → Automatic, Contours → {0}]
```

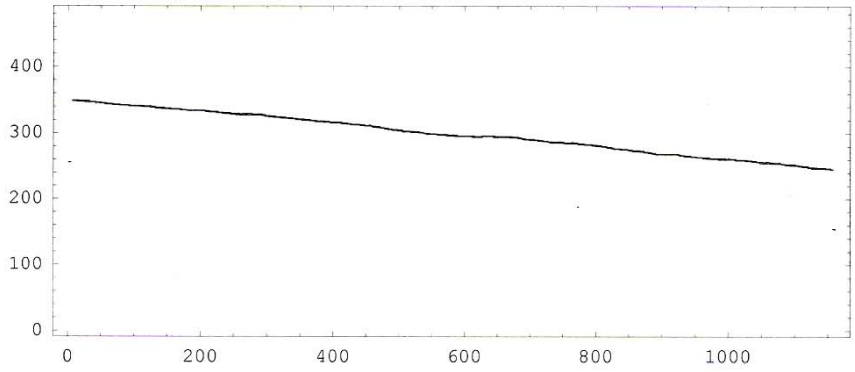


```
- ContourGraphics -
```

■ Determine which points on the DEM lie within the uncertainty swath for the fault location, ± the width of the "zoneHalfWidth," and map their boundary with the points that lie outside the swath

```
uncertSwath = Table[pointEvaluator[((gridSpacing * (j - 1)) - focus[[1]]),
    ((gridSpacing * (nrows - i)) - focus[[2]]), (mydata[[i + 6, j]] - focus[[3]]),
    zoneHalfWidth, faultUnitNormal, nodataValue], {i, nrows}, {j, ncols}];
```

```
elev2 = Table[uncertSwath[[i, j]], {i, nrows, 1, -1}, {j, ncols}];

traceImageFile2 = ListContourPlot[elev2,
  ContourShading → False, AspectRatio → Automatic, Contours → {0}]
```

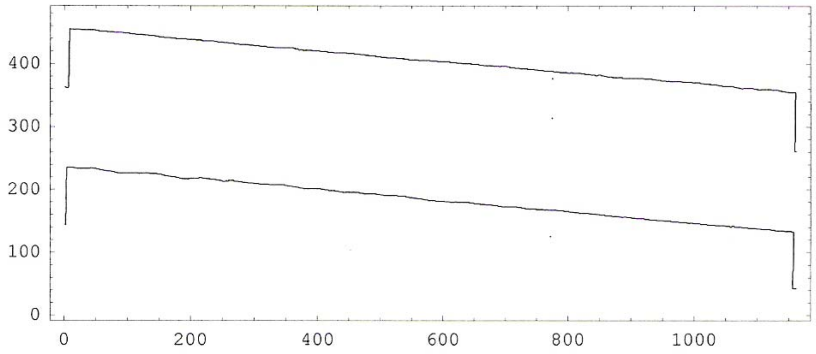


```
- ContourGraphics -
```

- **Combine the fault-trace map with the fault-swath map into a single graphic**

```
traceImageFile = Show[%, traceImageFile1];
```

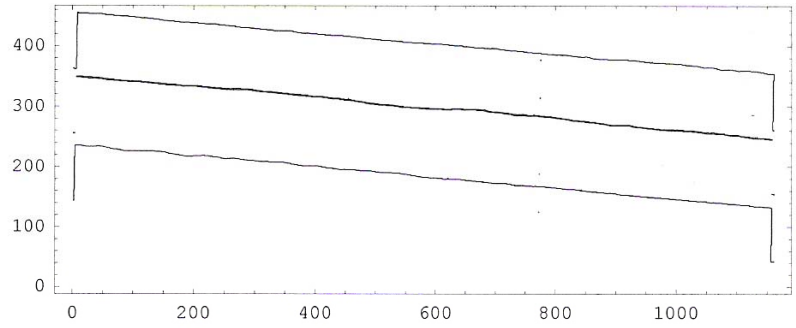

- **Plot a topographic contour map of the DEM, at a contour interval of 500 feet (152.4 meters)**

```
demImageFile = Table[mydata[[i + 6, j]] - focus[[3]], {i, nrows}, {j, ncols}];

aratio = nrows / ncols;
minval = 0;
maxval = Max[demImageFile];
relief = (maxval - minval);

elev3 = Table[demImageFile[[i, j]] + focus[[3]], {i, nrows, 1, -1}, {j, ncols}];
```

```
topoMap = ListContourPlot[elev3, ContourShading → False, Frame → False,
    AspectRatio → aratio, Contours → Table[c, {c, -152.3, 1000, 152.4}]];
```

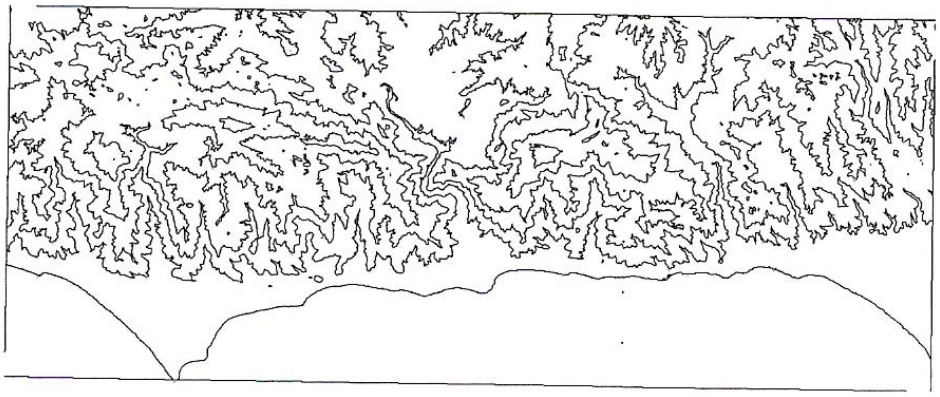

```
ListDensityPlot[elev3, AspectRatio → aratio, Frame → False,
  Mesh → False, ColorFunction → Function[z, GrayLevel[(0.3 + 0.7 z)]]];
```

```
shadedTopoMap = Show[%, topoMap];
```

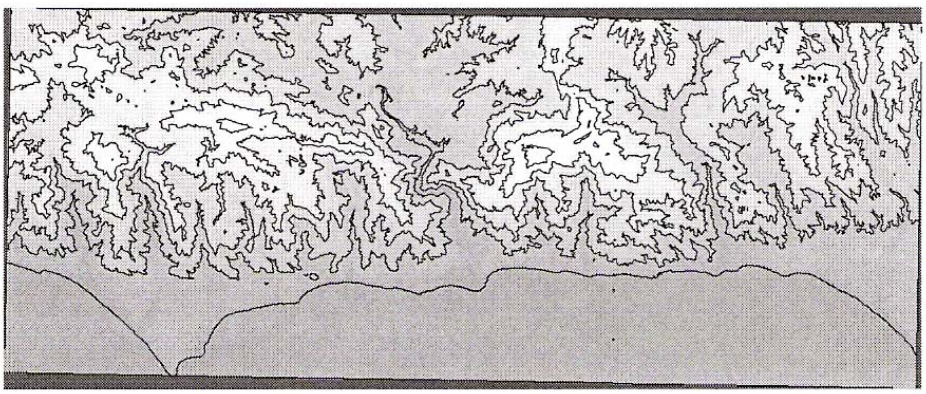

```
finalImage = Show[shadedTopoMap, traceImageFile]
```

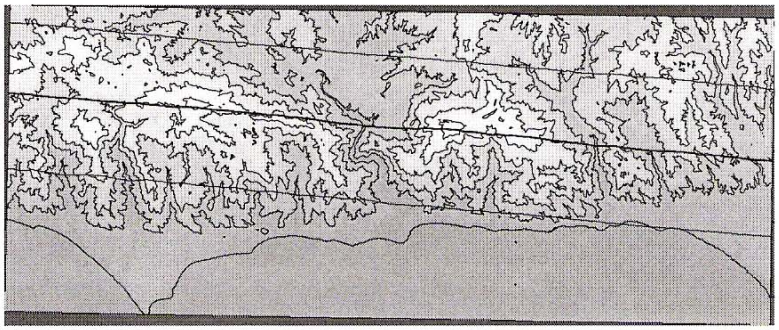

```
- Graphics -
```

■ Add the original header data to the output files

```
mergedData = Join[headerData, inFaultTrace];

mergedSwathData = Join[headerData, uncertSwath];
```

■ Export data and image files

The file created in the next line is a data file (.dat) with the same dimensions as the input DEM .dat file, but whose values are either the null value (-9999) or, for points located along the trace of the fault-plane solution intersection with the topography, some other value (typically "1" or the DEM-derived elevation at that node point).

```
Export["C:\\Documents and Settings\\Vince_Cronin\\
    Desktop\\LaurenSeidmanCode\\seisLinA1039a.dat", mergedData];
```

The file created in the next line is a data file (.dat) with the same dimensions as the input DEM .dat file, but whose values are either the null value (-9999) or, for points located along the boundaries of the uncertainty region, some other value (typically "1" or the DEM-derived elevation at that node point).

```
Export["C:\\Documents and Settings\\Vince_Cronin\\Desktop
    \\LaurenSeidmanCode\\seisLinB1039a.dat", mergedSwathData];
```

The file created in the next line is an encapsulated PostScript file (.eps) that contains the graphic showing the DEM shaded by elevation, the topographic contours at ~500 ft increments, curves marking the boundaries of the uncertainty region, and a curve showing the trace of the fault-plane solution intersection with the topography.

```
Export["C:\\Documents and Settings\\Vince_Cronin\\Desktop\\
    LaurenSeidmanCode\\EQ1039aseisLinMap.eps", finalImage, "EPS"];

ClearAll[mergedData, mergedSwathData, traceImageFile,
  traceImageFile1, traceImageFile2, finalImage, shadedTopoMap,
  mydata, inFaultTrace, uncertSwath, elev1, elev2, elev3];
```

■ **How long did this program take to run, in minutes?**

```
minutesForProcessing = (AbsoluteTime[] - startTime) / 60
```

```
22.739123253
```

References

Colley, S.J., 2002, Vector calculus [2nd edition]: Upper Saddle River, New Jersey, Prentice-Hall, 558 p., (pp. 43-50), ISBN 0-13-041531-6.

Cronin, V.S., and Sverdrup, K.A., 1998, Preliminary assessment of the seismicity of the Malibu Coast Fault Zone, southern California, and related issues of philosophy and practice, *in* Welby, C.W., and Gowan, M.E. [editors], A Paradox of Power--Voices of Warning and Reason in the Geosciences: Geological Society of America, Reviews in Engineering Geology, p. 123-155.

Cronin, V.S., Byars, B.W., and Gammill, T., 2003, Developing techniques for regional structural interpretation using GIS and DEM-based terrain analysis: Geological Society of America, Abstracts with Programs, v. 34, no. 7, p. 261. http://gsa.confex.com/gsa/2003AM/finalprogram/abstract_61851.htm

Davis, H.F., and Snider, A.D., 1987, Introduction to vector analysis [5th edition]: Boston, Allyn and Bacon, 365 p. (pp. 34-37), ISBN 0-205-10263-8.

Gammill, T., Cronin, V.S., and Byars, B.W., 2004, Combining earthquake focal data and digital map analysis in reconnaissance for active faults, central Santa Monica Mountains and northern Santa Monica Bay, California: Geological Society of America, Abstracts with Programs,v. 36, no. 5, http://gsa.confex.com/gsa/2004-AM/finalprogram/abstract_80352.htm

Haneberg, W.C., 2004, Computational geosciences with *Mathematica*: Berlin, Springer-Verlag, 381 p., CD, ISBN 3-540-40245-4.

Snyder, J.P., 1982, Map projections used by the U.S. Geological Survey: U.S. Geological Survey Bulletin 1532, pp. 63-69 and 233-235.

APPENDIX B

Sun Angles of Individual Seismo-Lineament Swaths

Table B. 1 Direction of Illumination in Degrees to Strike

Earthquake	Strike	plus 90	plus 30	plus 15	plus 60	minus 15	minus 30	minus 60	minus 90	0 degrees	composite image sun angle
2003103010718a	185	275	305	290	335	260	245	215	95	0	245
20030328054413a	335	45	75	60	105	30	15	345	245	0	245
19941026041847a	64	154	184	169	214	139	124	94	334	0	214
198605200740a	222	312	342	327	12	297	282	252	132	0	252
2000316095007a	120	210	150	135	180	105	90	60	30	0	210
19930726212949a	221	311	251	236	281	206	191	161	131	0	251
19940217161359a	213	303	243	228	273	198	183	153	123	0	243
198311231020100a	71	161	101	86	131	56	45	11	341	0	161
20000916132441a	175	265	205	190	235	160	145	115	85	0	235
19810812225800a	129	219	159	144	189	114	99	69	39	0	219

APPENDIX C

Worked Fisher Statistical Example with Actual Field Data

Fisher Statistics- Fault 2 at site 11

Vince Cronin, 26 Sept 2003 Revised 03/05/2006

User-Supplied Input Values

Number of measurements (N)	8	minimum = 3, maximum = 12
Instrument (compass) error	1.0	usually between 0.5° and 2°
Probability	0.10	0.05 for 95% CI

	Dip Azimuth/Trend (degrees)	Dip Angle/Plunge (degrees)	
First measurement	33	48	required
Second measurement	192	53	required
Third measurement	207	59	required
Fourth measurement if any	210	60	
Fifth measurement if any	220	45	
Sixth measurement if any	211	49	
Seventh measurement if any	190	46	
Eighth measurement if any	201	58	
Ninth measurement if any			
Tenth measurement if any			
Eleventh measurement if any			
Twelfth measurement if any			

	Output Values	code
Average dip azimuth/trend	0	=B75
95%CI uncertainty in strike/dip azimuth	0	=IF(((90-B29)>B28),B85,"indeterminate")
Mean dip angle/plunge	0	=D75
Radius of 95% CI uncertainty cone	0	=B83*(180/PI())
Estimate of k (class I if k≥10)	0	=B78

APPENDIX D

Computing the Trend and Plunge of a Lineation Given its Rake on a Specified Plane; Worked Example with Actual Field Data

Fault 2 at site 11

INPUT Azimuth of strike from which the rake was measured	OUTPUT Other strike azimuth	INPUT Right-hand rule reference-strike azimuth*	INPUT Dip angle	INPUT Reported rake (negative values for down-directed rakes)	OUTPUT Rake relative to reference strike (negative values for down-directed rakes)	OUTPUT Dip azimuth/ trend	OUTPUT Horizontal angle between strike and trend of lineation (b)	OUTPUT Plunge of lineation	OUTPUT Trend/azimuth of lineation
input value	=IF(A7>180,A7-180, A7+180)	input value; must equal value in either column A or B	input value	input value	=IF((A7<>C7),(-1*(180-ABS(E7))),E7)	=IF(C7>270, C7-270,C7+90)	=ABS(ATAN((SIN(F7*(PI()/180))*COS(D7*(PI()/180)))/COS(F7*(PI()/180)))*(180/PI()))	=ATAN(TAN(D7*(PI()/180))*SIN(H7*(PI()/180)))*(180/PI())	=IF((ABS(F7)>90),IF(((C7-180)-H7)<0),(360+((C7-180)-H7)),((C7-180)-H7)),IF(((C7+H7)>360),((C7+H7)-360),(C7+H7)))
303	123	303	48	-74	-74	33	67	46	10
102	282	102	53	-79	-79	192	72	52	174
117	297	117	59	-80	-80	207	71	58	188
120	300	120	60	-71	-71	210	55	55	175
130	310	130	45	-75	-75	220	69	43	199
121	301	121	49	-81	-81	211	76	48	197
100	280	100	46	-80	-80	190	76	45	176
111	291	111	58	-110	-110	201	56	53	235
0	180	0	0	0	0	90	0	0	0
0	180	0	0	0	0	90	0	0	0
0	180	0	0	0	0	90	0	0	0
0	180	0	0	0	0	90	0	0	0
0	180	0	0	0	0	90	0	0	0

APPENDIX E

Table E. 1. Complete Focal Mechanism Solution Information

Year	Month	Day	Hour	Minute	Second	ID	Latitude	Longitude	Depth (m)	Horizontal error (km)	Vertical error (km)	Magnitude	Strike	Dip-vector trend	Dip-vector plunge	Rake
1993	7	26	21	29	49.19	19930726212949a	33.9842	-118.733	15.04	0.2	0.3	3.6	131	221	55	125
1994	2	17	16	13	58.93	19940217161359a	33.9655	-118.631	13.82	0.6	0.8	2.62	123	213	65	110
1994	10	26	4	18	46.7	19941026041847a	34.1933	-118.689	4.66	0.2	0.2	2.4	334	64	59	-106
2000	3	16	9	50	6.7	20000316095007a	34.1262	-118.523	8.51	0.2	3.3	1.93	30	120	45	170
2003	10	31	1	7	18.31	20031031010718a	34.0562	-118.821	11.18	0.2	28.1	2.94	95	185	75	0
1986	5	20	7	11	39.91	19860520071140a	33.9382	-118.666	13.48	0.2	0.4	2.79	132	222	60	106
2000	9	16	13	24	41.17	20000916132441a	33.9725	-118.422	11.09	0.1	2.5	3.27	85	175	40	110
2003	3	28	5	44	12.91	20030328054413a	34.1388	-118.51	6.75	0.1	18.1	2.91	245	335	85	-40
1981	8	12	22	58		19810812225800a	34.126	-118.608	3.3	0.3	0.7	2.7	39	129	67	-69
1983	11	23	12	1		19831123120100a	34.031	-118.569	8.1	0.3	0.3	2.5	341	71	50	167

REFERENCES

Bayliss, B., and Cronin, V. S., 2005, Test of a method for recognizing previously unmapped seismogenic faults: Geological Society of America, Abstracts with Programs, v. 37, no. 7, p. 559. http://gsa.confex.com/gsa/2005AM/final program/abstract_94440.htm

Bayliss, B., 2006, Test of a method for recognizing previously unmapped seismogenic faults: Baylor University.

Biddle, K. T., [editor], 1991, Active margin basins: American Association of Petroleum Geologists, Memoir 52, p. 35-134.

Bird, P., and Rosenstock, R. W., 1984, Kinematics of present crust and mantle flow in southern California: Geological Society of America Bulletin, v. 95, p. 946-957.

Blake, G. H., 1991, Review of Neogene biostratigraphy and stratigraphy of the Los Angeles Basin and implications for basin evolution, *in* Biddle, K.T., [editor], Active margin basins: American Association of Petroleum Geologists, Memoir 52, p. 135-184.

Bohannon, R. G., and Parsons, T., 1995, Tectonic implications of post-50 Ma Pacific and North American relative plate motions: GSA Bulletin, v.107, p. 937-959.

Buika, J. A., and Teng, T. L., 1979, A seismicity study for portions of the Los Angeles basin, Santa Monica basin, and Santa Monica mountains, California: University of Southern California, Geophysical Laboratory, Technical Report 79-9, 191 p.

Burbank, D. W., and Anderson, R. S., 2001, Tectonic geomorphology: Oxford, Blackwell Science, 274 p.

Campbell, R. H., Blackerby, B. A., Yerkes, R. F., Schoellhamer, J. E., Birkeland, P. W., and Wentworth, C. M., 1996, Geologic map of the Point Dume quadrangle, Los Angeles County, California: U.S. Geological Survey Geologic Quadrangle Map GQ-4747. http://ngmdb.usgs.gov/ImageLibrary/ILview_xsl.html?sid=q24_61691_us_c.sid

Campbell, R. H., and Yerkes, R. F., 1976, Cenozoic evolution of the Los Angeles basin area—relation to plate tectonic, in Howell, D. ZG., *ed*., Aspects of the geologic history of the California continental borderland: American Association of Petroleum Geologists, Pacific Section, Miscellaneous Publication 24, p. 541-558.

Chester, F. M., Chester, J. S., Kirschner, D. L., Schulz, S. E., and Evans, J. P., 2004, Structure of large-displacement, strike-slip fault zones in the brittle continental crust, *in* Karner, G.D., Taylor, B., Driscoll, N.W., and Kohlstedt, D.L., [editors], Rheology and deformation of the lithosphere at continental margins: New York, Columbia University Press, p. 223-260.

Colburn, I. P., 1973, Stratigraphic relations of the southern California Cretaceous strata, *in* Colburn, I. P., and Fritsche, A. E., eds., Cretaceous stratigraphy of the Santa Monica Mountains and Simi Hills: Society of Economic Paleontologists and Mineralologists, Pacific Section, Fall Field Trip Guide book, p. 45-73.

Cronin, V. S., 2004a, A draft primer on focal mechanism solutions for geologists: On the Cutting Edge Workshop on Teaching Structural Geology in the 21st Century, Science Education Resource Center, Carleton College, 14 p.,http://serc.carleton.edu /files/NAGTWorkshops/structure04/Focal_mechanism_primer.pdf

——— 2004b, Projecting a fault plane from a focal mechanism solution onto a digital elevation model surface: unpublished *Mathematica* notebook.

——— 2004c, Seismo-lineament analysis method: draft manuscript.

——— 2007, Finding the mean and 95% confidence interval of a set of strike-and-dip or lineation data: Environmental and Engineering Geoscience*, in press*.

Cronin, V. S., and Sverdrup, K. A., 1998, Preliminary assessment of the seismicity of the Malibu Coast Fault Zone, southern California, and related issues of philosophy and practice, *in* Welby, C. W., and Gowan, M. E. [editors], A paradox of power--Voices of warning and reason in the geosciences: Geological Society of America, Reviews in Engineering Geology, p. 123-155.

Cronin, V. S., Byars, B. W., and Gammill, T., 2003, Developing techniques for regional structural interpretation using GIS and DEM-based terrain analysis: Geological Society of America, Abstracts with Programs, v. 34, no. 7, p. 261.

Cronin, V. S., Schurter, G. J., and Sverdrup, K. A., 1993, Preliminary Landsat lineament analysis of the northern Nanga Parbat-Haramosh Massif, northwest Himalaya, *in* Treloar, P. J., and Searle, M. P., [editors], Himalayan tectonics: Geological Society (London), Special Publication, No. 74, p. 193-206.

Crouch, J. K., and Suppe, J., 1993, Late Cenozoic tectonic evolution of the Los Angeles basin and inner California borderland: A model for core complex-like crustal extension: Geological Society of America Bulletin, v.105, p., 1415-1434.

Davis, T. L., Namson, J. S., and Yerkes, R. F., 1989, A cross section of the Los Angeles area: seismically active fold and thrust belt, the 1987 Whittier Narrows earthquake, and earthquake hazard: Journal of Geophysical Research, v. 94, p. 9644–9664.

Dibblee, T. W., Jr., 1993, Geologic map of the Malibu Beach Quadrangle, Los Angeles County, California: Dibblee Geologic Foundation Map DF-47, scale 1:24,000.

Dibblee, T. W., Jr., and Ehrenspeck, H. E., 1993, Geologic map of the Point Dume Quadrangle, Los Angeles County, California: Dibblee Geological Foundation Map DF-48, scale 1:24,000.

Dolan, J. F., Sieh , K., Rockwell, T. K., Yeats, R.S., Shaw, J., Suppe, J., Huftile, G., and Gath, E., 1995, Prospects for larger or more frequent earthquakes in greater metropolitan Los Angeles, California: Science, v. 267, p. 199–205.

Dolan, J. F., Sieh, K., and Rockwell, T. K., 2000, Late Quaternary activity and seismic potential of the Santa Monica fault system, Los Angeles, California: Geological Society of America Bulletin, v.112, p.1559–1581

Drumm, P. L., 1992, Holocene displacement of the central splay of the Malibu Coast fault zone, Latigo Canyon, Malibu, *in* Pipkin. B.W., and Proctor, R.J., [editors], Engineering geology practice in southern California: Belmont, California, Star Publishing Company, Association of Engineering Geologists, Southern California Section, Special Publication No. 4, 247-254.

Fisher, R. A., 1953, Dispersion on a sphere: Proceedings of the Royal Society, London, v. A17, pp. 295-305.

Fisher, M. A., Langenheim, V. E., Sorlien, C. C., Dartnell, P., Sliter, R. W., Cochrane, G.R., and Wong F.L, 2005, Recent deformation along the offshore Malibu Coast, Dume, and related faults west of Point Dume, southern California: Bulletin of the Seismological Society of America, v. 95, no. 6, p. 2486–2500

Fuis, G. S., and 14 others, 2003, Fault systems of the 1971 San Fernando and 1994 Northridge earthquakes, southern California - relocated aftershocks and seismic images from LARSE II: Geology, v. 31, no. 2, p.171-174.

Gammill, T., Cronin, V. S., and Byars, B. W., 2004, Combining earthquake focal data and digital map analysis in reconnaissance for active faults, central Santa Monica Mountains and northern Santa Monica Bay, California: Geological Society of America, Abstracts with Programs, v. 36, no. 5, p. 298.

Haneberg, W. C., 2004, Computational geosciences with *Mathematica*: Berlin, Springer-Verlag, 381 p., CD.

Hart, E. W., and Bryant, W. A., 1999, Fault-rupture hazard zones in California: Special Publication 42, California Department of Conservation Division of Mines and Geology, ftp://ftp.consrv.ca.gov/pub/dmg/pubs/sp/Sp42.pdf

Haugerud, R. A., Harding, D. J., Johnson, S. Y., Harless, J. L., Weaver, C. S., and Sherrod, B. L., 2003, High-resolution LIDAR topography of the Puget lowland, Washington – a bonanza for Earth science: GSA Today, v. 13, no. 6, p. 4-10, ftp://rock.geosociety.org/pubs/GSAToday/gt0306.pdf

Hardebeck, J. L., 2005, SCEDC web dataset: Southern California Earthquake Data Center, http://www.data.scec.org/research/socal_focal_JLH.html.

Hauksson, E., 1987, Seismotectonics of the Newport-Inglewood fault zone in the Los Angeles Basin, southern California: Bulletin of the Seismological Society of America, v. 77, p. 539–561.

——— 1990, Earthquakes, faulting, and stress in the Los Angeles Basin: Journal of Geophysical Research, v. 95, p. 15,365-15,394.

——— 2000, Crustal structure and seismicity distribution adjacent to the Pacific and North America plate boundary in southern California: Journal of Geophysical Research, v. 105, p. 13,875-13,903.

——— 2004, 3-D earthquake focal mechanisms: Southern California Earthquake Data Center, http://www.data.scec.org/research/socal_focal.html

Hauksson, E., and Saldivar, G. V., 1986, The 1930 Santa Monica and the 1979 Malibu, California, earthquakes: Bulletin of the Seismological Society of America, v. 76, p. 1542-1559.

Hauksson, E., and Saldivar, G. V., 1989, Seismicity and active compressional tectonics in Santa Monica Bay, southern California: Journal of Geophysical Research, v. 94, no. B7, p.9591-9606.

Hobbs, W. H., 1904, Lineaments of the Atlantic border region: Geological Society of America Bulletin, v. 15, p. 483-506.

Hoots, H. W., 1931, Geology of the eastern part of the Santa Monica Mountains, Los Angeles County, California: U.S. Geological Survey, Professional Paper 165-C, p. 83-134, map scale 1:24,000.

Hornafius, J. S., Luyendyk, B. P., Terres, R. R., and Kamerling, M. J., 1986, Timing and extent of Neogene tectonic rotation in the western Transverse Ranges, California: Geological Society of America Bulletin, v. 97, p. 1476-1487

Jackson, J., and Molnar, P., 1990, Active faulting and block rotations in the western Transverse Ranges, California: Journal of Geophysical Research, v.95, p. 22,073-22,087.

Kamerling, M. J., and Luyendyk, B. P., 1979, A model for Neogene tectonics of the inner southern California borderland constrained by paleomagnetic data: Geological Society of America, Abstracts with Programs, v. 11, no. 7, p. 453.

——— 1985, Paleomagnetism and Neogene tectonics of the northern Channel Islands, California: Journal of Geophysical Research, v. 90, p. 12485–12,502.

Keller, E. A., and Pinter, N., 2002, Active tectonics -- earthquakes, uplift and landscape [second edition]: Upper Saddle River, New Jersey, Prentice Hall, 362 p.

Lamar, D. L., 1961, Structural evolution of the northern margin of the Los Angeles Basin: Los Angeles, California, University of California at Los Angeles, 106 p.

Lajoie, K. R., Kern, J. P., Wehmiller, J. F., Kennedy, G. L., Mathieson, S. A., Sarna-Wojcicki, A. M., Yerkes, R. F., and McCrory, P. F., 1979, Quaternary marine shorelines and crustal deformation, San Diego to Santa Barbara, California, *in* Abbott, P.L., [editor], Geological excursions in the southern California area: Department of Geological Sciences, San Diego State University, for Geological Society of America Annual Meeting, Nov. 1979, p. 3-15.

Larson, K. M., 1993, Application of the global positioning system to crustal deformation measurements 3, Results from the southern California borderlands: Journal of Geophysical Research, v. 98, p. 21713–21726.

Lee, W. H. K., Yerkes, R. F., and Simirenko, M., 1979, Recent earthquake activity and focal mechanisms in the western Transverse Ranges, California: U.S. Geological Survey Circular 799-A, 26 p.

Legg, M. R., Kamerling, M. J., and Francis, R. D., 2004, Termination of strike-slip faults at convergence zones within continental transform boundaries -- examples from the California Continental Borderland, *in* Grocott, J., McCaffrey, K.J.W., Taylor, G., and Tikoff, B., [editors], Vertical coupling and decoupling in the lithosphere: Geological Society, London, Special Publication 227, p. 65-82.

Leighton and Associates, Inc., 1989, Report of investigation, Rancho Malibu Mesa project, Pacific Coast Highway at Malibu Canyon Road, Malibu, California: unpublished consultant's report, August 4, 1989, Job No. 3831025-04.

Leith, C. K., 1923, Structural Geology: New York, Henry Holt and Company.

Link, M. H., Squires, R. L., and Colburn, I. P., 1984, Slope and deep-sea fan facies and paleogeography of Upper Cretaceous Chatsworth Formation, Simi Hills, California: American Association of Petroleum Geologists Bulletin, v. 68, p. 850-873.

Leighton and Associates, Inc., 1989, Geotechnical Investigation and Grading Plan review, Lower Loop Road, Newport Coast, County of Orange

Lobeck, A.K., 1939, Geomorphology – an introduction to the study of landscapes: New York, McGraw-Hill Book Company, 731 p.

Luyendyk, B. P., 1991, A model for Neogene crustal rotations, transtension and transpression in California: Geological Society of America Bulletin, v.103, p. 1528-1536.

Luyendyk, B. P., Kamerling, M. J, and Terres, R. R., Hornafius, S. J., 1985, Simple shear of southern California during Neogene time suggested by paleomagnetic declinations: Journal of Geophysical Research, v. 90, p. 12454-12466.

Maune, D. F., 2001, Digital elevation model technologies and applications: The DEM user's manual: Bethesda, Maryland, American Society for Photogrammetry and Remote Sensing, 539 p.

McCalpin, J. P., [editor], 1996, Paleoseismology: San Diego, Academic Press, 588 p.

McGill, J. T., 1982, Preliminary geologic map of the Pacific Palisades area, city of Los Angeles, California: Technical Report 82-194.

Miller, V. C., 1961, Photogeology: New York, McGraw-Hill Book Company, 248 p.

Molnar, P., and Gibson, J. M., 1994, Very long baseline interferometry and active rotations of crustal blocks in the western Transverse Ranges, California: Geological Society of America Bulletin, v. 106, p. 594–606

Nicholson, C., Sorlien, C. C., Atwater, T., Crowell, J. C., and Luyendyk, B. P., 1994, Microplate capture, rotation of the western Transverse Ranges, and initiation of the San Andreas transform as a low-angle fault system: Geology, v. 22, p.491–495.

Pinter, N., Lueddecke, S. B., Keller, E. A., and Simmons, K. R., 1998, Late Quaternary slip on the Santa Cruz Island fault, California: Geological Society of America Bulletin, v. 110, no. 6, p. 711–722.

Ray, R. G., 1960, Aerial photographs in geologic interpretation and mapping: U.S. Geological Survey, Professional Paper 373, p. 230.

Reid, H. F., 1910, The Mechanism of the earthquake, *in* The California Earthquake of April 18, 1906, Report of the State Earthquake Investigation Commission: Washington D.C., Carnegie Institution, v. 2, p. 1-192.

Sage, O. G., Jr. 1973, Paleocene geography of the Los Angeles region, *in* Kovach, R. L., and Nur, A., eds., Proceedings, Conference on tectonic problems of the San Andreas fault system: Palo Alto, California, Stanford University Publications, Geological Sciences, v. XIII, p. 348-357.

Scholz, C. H., 2000, Evidence for a strong San Andreas fault: Geology, February 2000; v. 28; no. 2; p. 163-166.

Seeber, L., and Sorlien, C. C., 2000, Listric thrusts in the western Transverse Ranges, California: Geological Society of America Bulletin, v. 112, no. 7, p. 1067–1079.

Snyder, J. P., 1982, Map projections used by the U.S. Geological Survey: U.S. Geological Survey, Bulletin 1532, 313 p.

Sorlien, Christopher, Broderick, Kris, Kamerling, Marc, Fisher, M. A., Normark, W.R., Sliter, Ray, and Seeber, Leonardo, Oblique contraction beneath Santa Monica Bay, California [abs.]: Pacific Section American Association of Petroleum Geologists and Western Region Society of Petroleum Engineers 2003 Combined Meeting, Long Beach, CA, May 21-23, 2003.

Stierman, D. J., and Ellsworth, W. L., 1976, Aftershocks of the February 21, 1973, Point Mugu, California, earthquake: Bulletin of the Seismological Society of America, v. 66, p. 1931-1952.

Tsutsumi**,** H., Yeats, R. S., and Huftile, G. J., 2001, Late Cenozoic tectonics of the northern Los Angeles fault system, California: Geological Society of America Bulletin, v. 113, no. 4, p. 454–468.

Treiman, J. A., 1994, Malibu Coast fault, Los Angeles County, California: California Department of Conservation, Division of Mines and Geology, unpublished Fault Evaluation Report FER-229, October 3, 1994, 42 p.

——— [compiler], 2000, Fault number 99, Malibu Coast fault, *in* Quaternary fault and fold database of the United States, ver 1.0: U.S. Geological Survey Open-File Report 03-417.

U.S. Geological Survey, 1995, Malibu Beach, California 7.5 Minute Quadrangle: U.S. Geological Survey 7.5 Minute Series, 1 sheet, scale 1:24,000.

Webb, T. H., and Kanamori, H., 1985, Earthquake focal mechanisms in the eastern Transverse Ranges and San Emigdio Mountains, southern California and evidence for a regional decollement: Bulletin of the Seismological Society of America, v. 75, p. 737-757.

Wesnousky, S. G., 1986, Earthquakes, Quaternary faults, and seismic hazard in California: Journal of Geophysical Research, v. 91, p. 12587–12631.

Wesson, R. L., Helley, E. J., Lajoie, K. R., and Wentworth, C. M., 1975, Faults and future earthquakes, *in* Borcherdt, R.D., [editor], Studies for seismic zonation of the San Francisco Bay region: U.S. Geological Survey, Professional Paper 941-A, p. 5-30.

Worchester, P. G., 1948, A textbook of geomorphology: Toronto, D. Van Nostrand Company, 584 p.

Wright, T. L., 1991, Structural geology and tectonic evolution of the Los Angeles Basin, California, *in* Biddle, K.T., [editor], Active margin basins: American Association of Petroleum Geologists Memoir 52, p. 35-134.

Yeats, R. S., 1968, Rifting and rafting in the southern California borderland, *in* Dickinson, W. R., and Grantz, A., eds., Proceedings, Conference on tectonic problems of the San Andreas fault system: Palo Alto, California, Sanford University Publications, Geological Sciences, v. XI, p. 207-322.

Yeats, R. S., 1981, Quaternary flake tectonics of the California Transverse ranges: Geology, v. 9, no. 1, p. 16-20.

Yeats, R. S., Clark, M. N., Keller, E. A., and Rockwell, T. K., 1981, Active fault hazard in southern California: Ground rupture versus seismic shaking: Geologic Society of America Bulletin, Part 1, v. 92, p. 189-196.

Yerkes, R. F., and Campbell, R. H., 1980, Geologic map of east-central Santa Monica Mountains, Los Angeles County, California: U.S. Geological Survey, Map I-1146, scale 1:24,000.

Yerkes, R. F., Campbell, R. H., Blackberby, B. A., Wentworth, C. M., Birleland, P. W., and Schoellhamer, J. E., 1971, Preliminary geologic map of the Malibu Beach Quadrangle, Los Angeles County, California: U.S. geological Survey Open-File Map, scale 1:12,000.

Yerkes, R. F., and Lee, W. H. K., 1987, Late Quaternary deformation in the western Transverse Ranges, *in* Morton, D. M., and Yerkes, R. F. eds., Recent reverse faulting in the Transverse Ranges, California: U.S. Geological Survey Professional Paper 1339, p. 71-82.

Yerkes, R. F., and Wentworth, C. M., 1965, Structure, Quaternary history, and general geology of the Corral Canyon area, Los Angeles County, California: U.S. Geological Survey, Open-File Report 864, 214 p.

Yunger, A., 1976, Tectonics of the southern California borderland, *in* Howell, D. G., ed. Aspects of the geologic history of southern California continental borderland: American Association of Petroleum Geologists, Pacific Section, Miscellaneous Publication 24, p. 486-498.

Ziony, J. K., and Yerkes, R. F., 1985, Evaluating earthquake and surface faulting potential, *in* Ziony. J. I., [editor], Evaluating earthquake hazards in the Los Angeles region—An Earth-science perspective: U.S. Geological Survey, Professional Paper 1360, p. 43-91.